USING TRANSVERSE OPTICAL PATTERNS FOR ULTRA-LOW-LIGHT ALL-OPTICAL SWITCHING

by

Andrew M. C. Dawes

Department of Physics
Duke University

Date: _____

Approved:

_____
Dr. Daniel J. Gauthier, Chair

_____
Dr. John Thomas

_____
Dr. Harold Baranger

_____
Dr. Josh Socolar

_____
Dr. Henry Everitt

Dissertation submitted in partial fulfillment of the
requirements for the degree of Doctor of Philosophy
in the Department of Physics
in the Graduate School of
Duke University

2008

ABSTRACT

USING TRANSVERSE OPTICAL PATTERNS FOR ULTRA-LOW-LIGHT ALL-OPTICAL SWITCHING

by

Andrew M. C. Dawes

Department of Physics
Duke University

Date: _____

Approved:

_____
Dr. Daniel J. Gauthier, Chair

_____
Dr. John Thomas

_____
Dr. Harold Baranger

_____
Dr. Josh Socolar

_____
Dr. Henry Everitt

An abstract of a dissertation submitted in partial fulfillment of the
requirements for the degree of Doctor of Philosophy
in the Department of Physics
in the Graduate School of
Duke University

2008

Abstract

All-optical devices allow improvements in the speed of optical communication and computation systems by avoiding the conversion between the optical and electronic domains. The focus of this thesis is the experimental investigation of a new type of all-optical switch that is based on the control of optical patterns formed by nonlinear interactions between light and matter.

The all-optical switch consists of a pair of light beams that counterpropagate through warm rubidium vapor. These beams induce a nonlinear optical instability that gives rise to mirrorless parametric self-oscillation and generates light in the state of polarization that is orthogonal to that of the pump beams. In the far-field, the generated light forms patterns consisting of two or more spots. To characterize this instability, I observe experimentally the amount of generated power and the properties of the generated patterns as a function of pump beam intensity, frequency, and size. Near an atomic resonance, the instability has a very low threshold: with less than 1 mW of total pump power, >3 μW of power is generated.

To apply this system to all-optical switching, I observe that the orientation of the generated patterns can be controlled by introducing a symmetry-breaking perturbation to the system. A perturbation in the form of a weak switch beam injected into the nonlinear medium is suitable for controlling the orientation of the generated patterns. The device operates as a switch where each state of the pattern orientation corresponds to a state of the switch, and spatial filtering of the generated pattern defines the output ports of the device. Measurements of the switch response show that it can be actuated by as few as 600 $\pm$40 photons. For a switch beam with 1/e field radius $w_0 = 185 \pm 5\,\mu$m, 600 $\pm$40 photons correspond to an energy density of $5.4 \pm 0.7 \times 10^{-4}$ photons/$\lambda^2/(2\pi)$ which is comparable to the best reported results from

all-optical switches. The approach to all-optical switching I report here operates at very low light levels and exhibits cascadability and transistor-like response. Furthermore, the sensitivity is comparable to switches using cold-atom electromagnetically-induced transparency or cavity quantum-electrodynamics techniques, but is achieved with a simpler system, requiring only one optical frequency and occurring in warm atomic vapor.

I develop a numerical model for the switch that exhibits patterns that rotate in the presence of a weak applied optical field. Results from this model, and from my experiment, show that the switch response time increases as the input power decreases. I propose that this increase is due to critical slowing down. Mapping the pattern orientation to a simple one-dimensional system shows that critical slowing down may account for the observed increase in response time at low input power. The ultimate performance of the device is likely limited by critical slowing down and I conclude that the minimum number of photons capable of actuating the switch is between 400 and 600 photons.

My approach to all-optical switching is simple, extremely sensitive and exhibits many of the properties necessary for use as an optical logic element. Additionally, this work has implications for a wide range of pattern forming systems, both in the field of optics and beyond, that may be applicable as novel devices for sensitive measurement and detection.

Contents

List of Tables

List of Figures

Acknowledgements

There are countless other people who have contributed, in one way or another, to the work I present in this dissertation. To list them all would be impossible, but I will attempt to convey my gratitude towards everyone who has had a lasting or pivotal influence on me or my work as a scientist.

My graduate career at Duke began when I first met my advisor, Dr. Daniel Gauthier in Rochester New York at the 8th Conference on Coherence and Quantum Optics. As a senior undergraduate, I was in search of the next step in my career, and his enthusiasm for science and commitment to his students was immediately obvious during our conversations at the conference. I have never seen him run out of ideas for what to try next in the lab, and his ability to maintain a seemingly endless list of interesting projects is impressive and inspiring. I wish him and his group the best of luck for their future projects and hope to have an opportunity to collaborate in the future.

I owe thanks to two agencies for providing financial support for the projects I have worked on at Duke. The Army Research Office provided support through grant W911NF-05-1-0228, and the Darpa Defense Sciences Office provided support through the Slow Light project Contract PO 412785-G-2.

Dr. Alex Gaeta was generous in answering questions as I began working on numerical simulations of my nonlinear optical system. He helped me begin this daunting task by providing me with a Fortran implementation of the one-dimensional split-step beam propagation method. This saved me from spending a significant amount of time writing and debugging code had I started from scratch.

I have been fortunate to share my time in graduate school with many people who have become good friends of mine. In the early years, I spent a fair bit of time with the other west-coast crew: Bason Clancy, Carolyn Berger, and Dean Hidas. Members of the

upper-class who contributed to my enjoyment of graduate school include Brian Bunton, John Wambaugh, Joe Kinast, and Brad Marts. Ann Pitruzello, although technically a BME student, should be mentioned in this list as well. She and John have helped maintain a weekly tradition of cheap food and good beer, two key ingredients for surviving graduate school.

The other members of my research group have provided both excellent advice and useful mentoring opportunities. Michael Stenner was busy writing his thesis when I arrived in the group, but was still willing to help me find my way around and answer my numerous questions. Joel Greenberg had a smokey start in the lab but has since proven himself and will be a successful member of the group. I owe Kristine Callan thanks both for helping me find a job and for several hours of pro bono babysitting for Carter. I wish her luck as she begins her new career, she will continue to be a great physics teacher.

My parents are responsible for all of the right decisions I made for the first half of my life. I'll take full credit for the wrong ones, and hope that I have recovered from them gracefully. At first, I may have tried not to follow in my Mother's footsteps as a science teacher, but clearly there is a certain amount of destiny encoded in my genes, and I am happy to have found teaching among my many scientific passions. My Father has always been willing to let me try something myself, and for this I am forever grateful. A phrase I have never heard from him is "don't do that, you might break it." Whatever *it* was, he would rather see me discover how to make it work than be short on confidence or doubt my own ability to tinker.

Both of my Grandfathers have also inspired me at various points in my life. One, a successful immunologist, helped set the foundation for my career in science by obliging my perennial request to spend an entire day at the Omniplex science museum whenever I would visit Oklahoma City. The other, a one-time engineer who could never be

accurately described by a single career or interest, was a perpetual hobbyist and expert tinkerer. He was known for sending his helpers, myself included, to the hardware store with a list of parts that no one else in the world had ever heard of. One way or another, though, we were able to succeed at implementing his designs.

More than anyone I have mentioned, I owe my survival and sanity to my pulchritudinous wife Leslie and her love and devotion. She has always been able to keep my head above water with a subtle balance of supportive gestures and profound insight. Being able to share the good times with her has made them even better, and weathering the bad times together makes them seem short and surmountable. Our son Carter has been a wonderful addition to the family and he helps keep everything in perspective. I enjoyed discovering his artwork on the back sides of my early thesis drafts, and I hope everyone else find this document as entertaining as he did during its preparation.

Chapter 1

Introduction

1.1 Spontaneous Pattern Formation

The spontaneous emergence of regular structure from natural processes has been observed throughout history. Found in nearly every field of science, and even in social and personal interactions, patterns are one of the most recognizable signatures of a nonlinear dynamical system. The study of such systems, and other large classes of phenomena, including chaos and solitons, is the primary goal of the active branch of physics known as *dynamics*. The mathematical tools developed in the field of dynamics have been used successfully to describe a wide range of pattern forming systems in biology, chemistry, computer science, and sociology [1–3].

The spontaneous formation of patterns takes place through a variety of mechanisms, each of which has the generic feature of competition between driving forces and dissipation in the system. In Rayleigh-Bénard convection, a canonical example of pattern formation, patterns are formed in a sheet of fluid contained between two horizontal plates where the driving force is a temperature difference between the top plate and the bottom plate. This driving force overcomes dissipation due to thermal conduction and viscosity, leading to the formation of convection patterns within the fluid.

Another simple example from nonlinear optics is the competition between nonlinearity and dispersion in soliton pulse propagation. In a nonlinear optical medium, pulses with a certain shape experience a nonlinearity that exactly balances the effects

of dispersion, thereby allowing the pulses to propagate without changing shape. In Chapter 3, I describe in greater detail an example of a pattern-forming system in nonlinear optics.

The quantitative description of pattern formation requires a study of the system dynamics and their stability relative to perturbations. In the general approach, a system is described by a set of differential equations that specify the trajectory of the system's state vector through phase space. Linear stability is determined by applying infinitesimal perturbations to the steady-state solutions of this equation set, and determining if such perturbations grow or shrink as the state of the system evolves. For spatially extended systems, the same concepts apply, although it is often the stability of the Fourier modes of the system that is of interest. Hence, if infinitesimal perturbations applied to a specific mode grow as the system evolves, that mode can give rise to an instability. Instabilities such as this are responsible for pattern formation in systems with two or more dimensions.

The term *pattern selection* refers to the tendency of the system to exhibit patterns with a certain symmetry or orientation. Understanding the pattern selection process is of fundamental importance to understanding the patterns observed in the system because many patterns are allowable solutions to the dynamics equations of the system, yet only a subset of the allowed patterns are typically exhibited. Patterns are selected both by constraints on the system and by the dynamics of the system. The optical patterns that are the subject of this thesis exhibit pattern selection by both mechanisms, although primarily via the system dynamics, in particular through external forcing [1].

Given a specific system, and thus specific allowable solutions (*i.e.*, allowed patterns), control of the patterns is limited to choosing from among these solutions. Hence, it is through controlling pattern selection that one can control the pattern generated by a system. Attempting to control the spontaneous patterns formed by

nonlinear processes is not an intrinsically new idea. In fact, attempts to control many aspects of nature are simply attempts to control the patterns that arise from nature's fundamental processes. Weather, ocean currents, tides, and wind are all patterns. There are, however, new applications for controllable pattern-formation, and one such application, controlling the flow of optical information, is the focus of this thesis.

Scientists are generally interested in controlling the flow of information. An early example of this is the diode vacuum tube, where electrons drift from a hot filament (cathode) to a charged plate (anode) allowing current to flow through the device in only one direction. More advanced vacuum tubes use similar principles to amplify electronic signals and perform other information-control functions. Advances in solid state physics led to the development of semiconductor materials and the transistor. Considered one the greatest inventions of the 20th century, the transistor has been responsible for the miniaturization of electronics enabling an enormous range of information-handling devices from cellular telephones to supercomputers. The development of the internet (world-wide-web) was enabled by personal computers and fueled by scientists need for shared information in the high-energy physics community.

To support the growing technological demands of the information age, the field of optics has developed a wide range of devices for generating, transmitting, detecting, and processing optical signals. All-optical devices are capable of operating at much higher bandwidths than electronic devices and more importantly, they are capable of much higher information density. In order to store or process information, an electronic device must displace electrons and separate them with a potential barrier. This process requires power that must ultimately be dissipated as heat. Thermal dissipation places limits on the density and speed of electronic devices; these limits have already been reached by leading-edge technology [4]. The development of all-optical devices that are capable of operating with low input power is thus an important step towards

improving information technology.

My contribution to this field is to investigate the control of patterns formed in a nonlinear optical system, and the application of such control to the problem of ultra-low-light-level all-optical switching. Nonlinear optical patterns have been observed for nearly 50 years since the invention of the laser and the birth of the field of nonlinear optics [5]. By combining ideas of pattern formation from the nonlinear dynamics community, with nonlinear optics, I have developed a device that demonstrates all-optical switching at ultra-low-light levels.

Prior to this work, many attempts to improve the sensitivity of all-optical switches were based on two assumptions. The first is that all-optical switching cannot be achieved with an input energy density of less than one photon per atomic cross section [6]. The second is that, in order to observe all-optical switching, the nonlinear phase shift induced by the input beam must be of the order of π radians [7, 8]. After discussing some instructive examples that serve to introduce and define these concepts, I will describe an all-optical switch that overcomes both of these limitations by exploiting the inherent sensitivity of nonlinear instabilities and the associated pattern-forming processes.

1.2 Overview of this Thesis

This thesis describes my investigation of controlling optical patterns generated by nonlinear interactions between laser light and warm rubidium vapor. Controlling these patterns leads to a new type of all-optical switch that can be actuated by less than 600 photons. The sensitivity, measured in units of photons per $\lambda^2/(2\pi)$, is comparable to the best results from devices based on electromagnetically-induced transparency (EIT). In addition to having high sensitivity, the switch is the first ultra-low-light level

device to exhibit transistor-like response. Additionally, the switch output beams are stronger than the input beams, thus making the switch cascadable; one device can be used to drive another, a feature that is required of all practical logic elements. This thesis presents an all-optical switch that meets the requirements for use as an all-optical logic element that operates at ultra-low-light levels. Additionally, I describe the various modifications that have been made to the experimental setup during the course of my research, and the improvements these modifications led to.

Chapter 2 presents two simple all-optical switches that illustrate the fundamental concepts behind all-optical switching. Chapter 3 describes theoretically the origin of pattern formation in nonlinear optical systems with counterpropagating beams. Chapter 4 describes my experimental observations of pattern formation in rubidium vapor. I also describe specific aspects of the experimental system that are necessary to generate patterns that are well suited to sensitive all-optical switching. These include beam alignment, vapor cell design, and shielding from external magnetic fields. In Chapter 5, I present a device that operates as an all-optical switch by controlling the orientation of transverse patterns. Results are presented, and discussed in the context of prior work on all-optical switching. Chapter 6 presents a numerical model for the switch system, and results from this model. With this model, I obtain qualitatively similar results in comparison to the experiment with regards to the time response of the switch and the input power level. Chapter 7 presents a simple 1D model, based on arguments of symmetry-breaking, that exhibits critical slowing down which can explain the increase in response time for low switch-beam powers. Finally, in Chapter 8, I summarize my main results and describe possible future directions for my research.

In greater detail, I begin the discussion of all-optical switching in Chapter 2 with two pedagogical examples of all-optical switches. The first switch, shown in Fig. 1.1, is based on the intensity-dependent refractive index of nonlinear optical media. In such

a switch, the nonlinear phase shift experienced by a beam in traversing a nonlinear optical medium can cause constructive or destructive interference when the medium is used in only one arm of an interferometer.

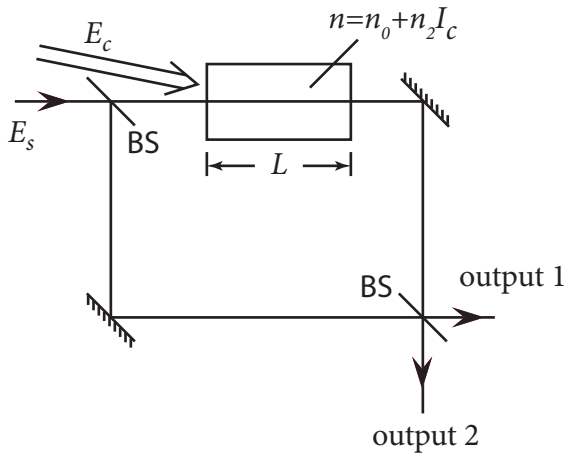

Figure 1.1: The intensity-dependent phase shift experienced by a beam propagating through a nonlinear medium can be used to construct an all-optical switch by placing a nonlinear medium in one arm of an interferometer. A strong control beam affects the nonlinear phase shift and thus the interferometer output.

The second switch, shown in Fig. 1.2, is based on a medium with saturable absorption; specifically, an ensemble of two-level atoms. With a medium that exhibits saturable absorption, one beam of light can serve to saturate the atomic response of the sample, thus allowing a signal beam to pass through with little absorption. When the control beam is turned off, the medium is no longer being saturated, and the signal experiences strong absorption.

I also review recent work in the field of low-light all-optical switching, and describe several different schemes that have been demonstrated. To facilitate comparison between vastly different approaches, I introduce a metric where the input energy density of an all-optical switch is measured in photons per $\lambda^2/(2\pi)$. This metric reports the number of photons required to actuate an all-optical switch that has a transverse di-

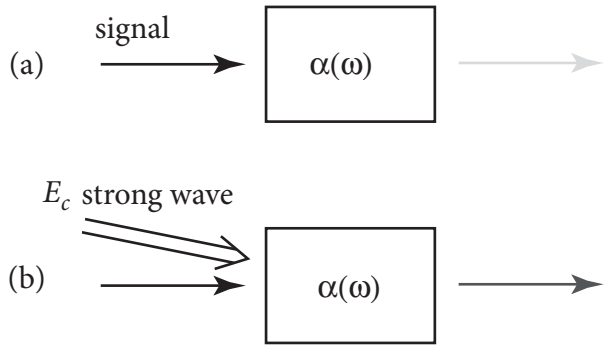

Figure 1.2: A strong control beam serves to saturate the absorption of a nonlinear medium. This beam thus controls the transmission of a signal beam propagating through the medium.

mension equal to $\lambda^2/(2\pi)$, which corresponds, up to a constant, to both the diffraction limit of the interacting fields and the maximum cross-section for a two-level atom. Using this metric, the most sensitive all-optical switch reported to date can be actuated with as few as 10^{-5} photons/$\lambda^2/(2\pi)$ [9].

In Chapter 3, I describe a simple model system: two optical beams counterpropagating in a medium with Kerr-type nonlinearity. This model assumes that the optical medium has an intensity-dependent index of refraction: $n(\omega) = n_0 + n_2 I$, where n_0 is the linear refractive index, n_2 is the nonlinear refractive index, and I is the intensity of the light. By making this assumption, it can be shown that counterpropagating beams couple through this intensity dependence and are unstable to the growth of off-axis beams. A linear stability analysis is performed on the steady-state solutions to the set of counterpropagating beam equations. This analysis provides a conceptual foundation for the generation of off-axis patterns in counterpropagating beam systems. The instability threshold, shown in Fig. 1.3, is found to be lowest for $K^2 L/2k \simeq 3$ where K is the transverse wavevector of the perturbation, L is the medium length, and k is the pump-beam wavevector within the medium. This result implies that, above the instability

threshold, the system will spontaneously emit off-axis beams with transverse wavevector $K = \sqrt{6k/L}$. To continue this introduction, I review a qualitative description of the effects of symmetry-breaking on optical pattern formation. Specifically, I discuss the origin of flowerlike patterns and patterns with hexagonal and two-spot symmetry. Finally, I introduce polarization instabilities, and describe several theoretical treatments and their predictions for my experimental system.

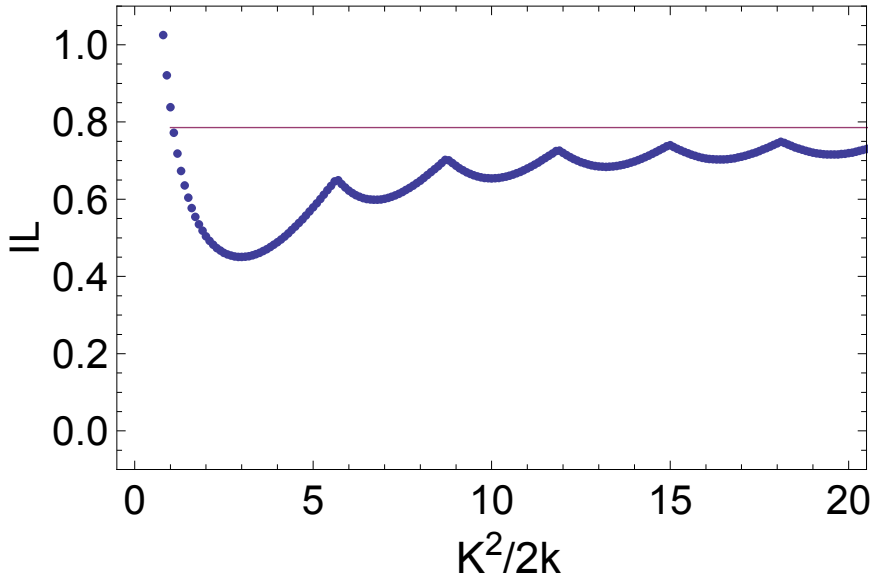

Figure 1.3: The threshold intensity for plane waves counterpropagating within a transparent medium exhibiting an intensity-dependent refractive index, from [10].

In Chapter 4, I present a simple experimental system that gives rise to transverse optical patterns with less than 1 mW of optical pump power. An instability in the system gives rise to mirrorless parametric self-oscillation, which is responsible for generating new beams of light that propagate at an angle to the pump beams and form multi-spot patterns in the far-field, such as those illustrated in Fig. 1.4. I have characterized this instability, and the generated patterns, in terms of several properties of the pump beams: frequency, intensity, size, and alignment. A forward pump beam with 415 μW of power and a backward pump beam with 145 μW of power, both detuned

to the high-frequency side of the ^{87}Rb $F = 1 \rightarrow F' = 1$, D_2 resonance, generate $\sim$3 μW of optical power.

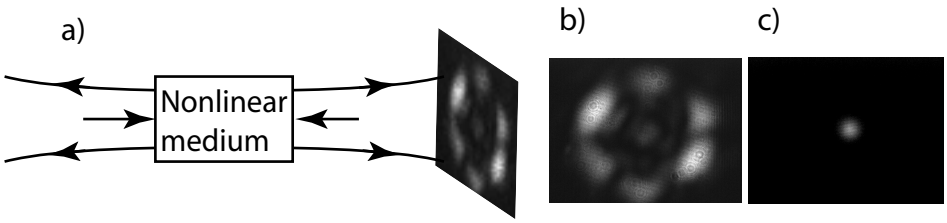

Figure 1.4: Beams counterpropagating through a nonlinear medium give rise to transverse structure in the field in the plane perpendicular to the direction of propagation. a) Beams and nonlinear medium. b) Hexagonal pattern. c) Pump beam transmitted off-resonance (for reference)

This instability is also responsible for the formation of optical patterns. The form of these patterns is two or more spots arranged along a ring corresponding to the projection of a cone of light onto the plane of measurement. The angle between the cone and the pump-beam axis is $\theta \simeq 4$ mrad. Patterns with hexagonal symmetry are observed in addition to patterns with up to 18 spots. Increasing the pump beam intensity or the pump beam size leads to patterns with finer transverse scales, and in general, to patterns with a larger number of spots. Just above threshold, for all pump beam sizes studied, the pattern consists of a pair of spots symmetrically located across the pump-beam axis from one another.

Additionally, I observe a secondary modulational instability that gives rise to fluctuations in the intensity of the generated light. The frequency of these fluctuations depends directly on the angle θ_p between the counterpropagating pump beams. For well-aligned pump beams, this instability is greatly suppressed, for pump beams misaligned by $\theta_p \simeq 0.4$ mrad, the instability has a characteristic frequency of $\sim$245 kHz.

In Chapter 5, I demonstrate the application of transverse optical patterns to ultra-

low-light all-optical switching. The system described in Chapter 4 generates patterns that are extremely sensitive to perturbations. A perturbation in the form of a weak switch beam injected into the nonlinear medium is suitable for controlling the orientation of the generated patterns and thus operating as a switch where each state of the pattern orientation corresponds to a state of the switch. This controlled pattern rotation is illustrated in Fig. 1.5.

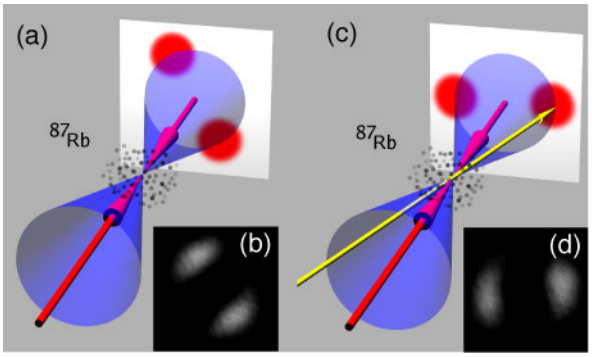

Figure 1.5: A two-spot transverse optical pattern rotates when a switch beam is injected into the rubidium vapor.

Spatial filtering of the generated pattern defines the output ports of the device, and measurements of the switch response show that it can be actuated by as few as 600 $\pm$40 photons. For a switch beam with 1/e field radius $w_0 = 185 \pm 5\,\mu$m, the corresponding energy density is $5.4 \pm 0.7 \times 10^{-4}$ photons/$\lambda^2/(2\pi)$, or about a factor of five times greater than the best electromagnetically-induced transparency (EIT) switch reported to date [9].

The response time of the switch depends on the strength of the perturbation and increases for low switch beam power levels. Figure 1.6 shows the behavior of the switch response time as a function of switch beam power. Also shown is the number of photons required to actuate the switch. I observe switch response with as few as 600 $\pm$40 input photons. This device exhibits sensitivity that is comparable to the best reported EIT-based switch to date, however, single-photon switching is not possible

with my system. As I discuss in Chapter 5, single photon switching may be achieved by extending this concept to related systems such as an anisotropic samples of cold atoms. The ultimate performance limitations of this device are also discussed in Chapter 7.

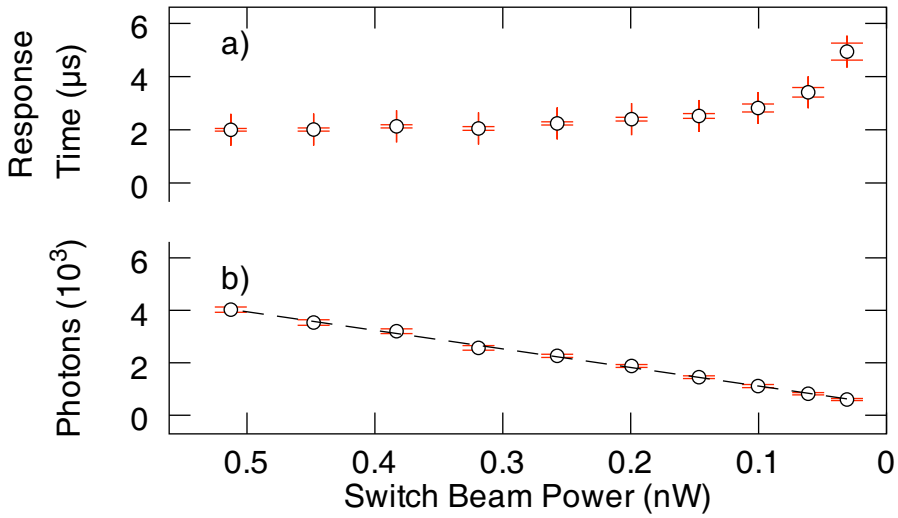

Figure 1.6: Based on the switch beam power, and the response time, I calculate the number of photons required to actuate the switch. The number of switching photons is plotted as a function of input power. The dashed line indicates the fit: $N_p = 7081P_s + 404$ for P_s in nW.

In Chapter 6, I describe a numerical model of a counterpropagating beam system that exhibits pattern formation and sensitive switching. Previous simulations, based on the Kerr model described by Firth and Paré, have been conducted by Chang *et al.* [11] and exhibit the formation of hexagon patterns for a wide range of simulation parameters. In Chapter 6, I extend this result by showing that, not only are hexagonal patterns successfully simulated by this model, the model also describes pattern rotation induced by a very weak external switch beam. Also, I show that the simulated switch responds to switch beams that are six orders of magnitude weaker than the pump beams. Furthermore, this model reproduces qualitatively the relationship between the switch response time and the switch-beam power. Figure 1.7 shows results from

the simulation of all-optical switching with transverse patterns generated by gaussian beams counterpropagating through a Kerr nonlinear medium. The switch response time increases for decreasing switch-beam powers and is qualitatively similar to my experimental observations.

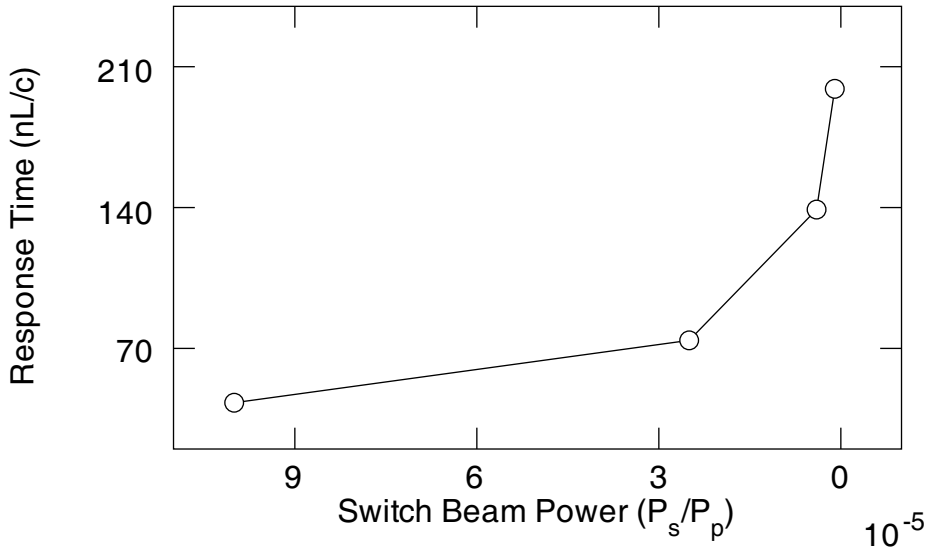

Figure 1.7: Simulation of the switch exhibits an increase in response time for decreasing power that is qualitatively similar to experimental observations. To facilitate comparison to Fig. 5.8(a), the horizontal axis has high switch-beam power to the left and low switch-beam power to the right.

The qualitative agreement between this model and my experimental observations indicates that the nonlinear Kerr medium, although different from rubidium vapor in important ways, exhibits many of the features required to describe transverse optical patterns and pattern-based all-optical switching.

In Chapter 7, I develop a simple 1D model describing the pattern orientation angle as a function of an applied perturbation. This model is based on arguments of symmetry-breaking and a potential which describes the preferred state of orientation. The potential is motivated solely by the observed patterns generated by my system and does not correspond to any physical property of the system as far as I know. Fig-

ure 1.8 shows the potential with an applied perturbation which causes two wells to be global minima, leading to a two spot pattern. The potential has the form of six wells evenly spaced around a ring. The relative depth of these wells and of the entire ring correspond to the preference of the system to emit light in a hexagonal pattern. To describe the pattern orientation using this potential, I consider motion only around the ring, and map this motion to a one-dimensional flow around a circle. With this simple model, I show how the preferred orientation changes by perturbing the potential. The response time of the orientation is large for weak perturbations and small for strong perturbations, in agreement with my experimental and simulated observations.

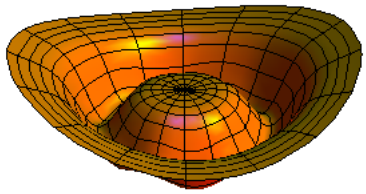

Figure 1.8: The potential surface for a simple model that exhibits critical slowing down of the pattern rotation. The pattern orientation corresponding to global minima of this hexagonal potential shows that critical slowing down can account for the increased response time I observe experimentally for weak switch-beam power.

In Chapter 8, the final chapter, I review my experimental and numerical results, and discuss possible directions for future work.

My preliminary work, conducted in 2004 and 2005, resulted in an all-optical switch that was the first to demonstrate sensitive all-optical switching with transverse patterns [12]. The results of my first switch design were substantially better than previous all-optical switches. I achieved switching with as few as 2,700 photons, where the best competing switches required over 1 million photons. Through the course of my research, many improvements have been made to the design of the all-optical switch described here. These improvements are discussed in detail in Appendix A.

Chapter 2

All-Optical Switching

An all-optical switch is a device that allows us to control of one beam of light with another. Beams of light do not interact when propagating in vacuum due to the linearity of Maxwell's equations, so all-optical switches rely on nonlinear interactions between light and matter. Two fundamental properties of a switch are that the device exhibit at least two distinguishable states, and that the device input and output are distinguishable.

There are many possible configurations for all-optical switches, as shown in Fig. 2.1. In general, all-optical switches can change the output power, direction, or state of polarization of a beam of light that is either propagating through a nonlinear medium or generated within the medium. Figure 2.1 illustrates devices that change the direction or power of either transmitted or generated beams. These are generic devices without specific implementation details. In order to clarify these configurations and introduce other concepts that are fundamental to all-optical switching, the following sections introduce two specific examples of all-optical switches. The first is based on an interferometer and relies on the nonlinear phase shift experienced by beams in one arm of the interferometer. The second uses a saturable absorber as the nonlinear medium, where a strong beam controls the absorption experienced by a weak beam.

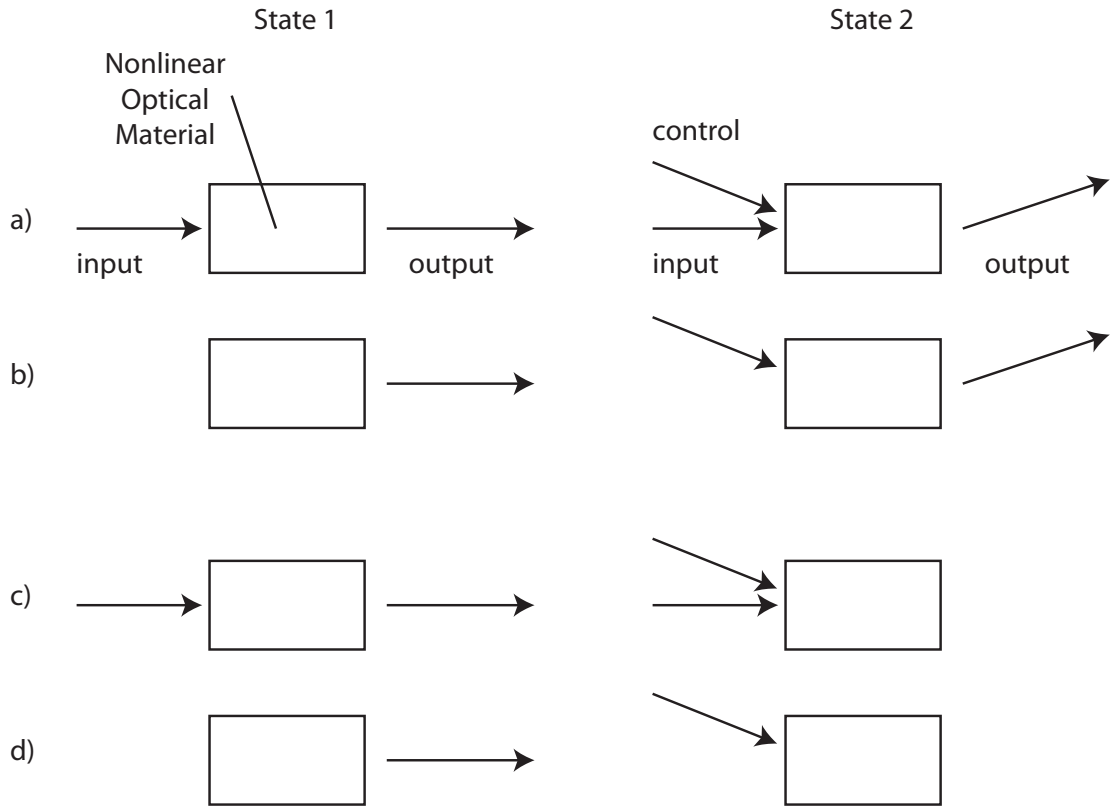

Figure 2.1: Four generic types of all-optical switch. Each switch has two states, indicated by the two columns in the diagram. Each row illustrates one variation on the type of switch. a) The presence of a control beam changes the direction of a beam propagating through the medium. b) The control beam changes the direction of a beam generated within the medium. c) The control beam causes a beam propagating through the medium to be absorbed or scattered. d) The control beam prevents the generation of a beam within the medium.

2.1 All-Optical Switching via Nonlinear Phase Shift

One simple all-optical switch that has been demonstrated in a wide variety of materials is based on the intensity-dependent refractive index of transparent nonlinear optical media. The intensity-dependent refractive index leads to a nonlinear phase shift experienced by a wave propagating through the medium. This effect can be used in all-optical switching by inserting such a medium in one arm of an interferometer.

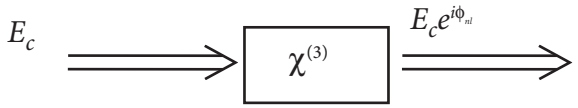

Figure 2.2: A beam traveling through a nonlinear medium experiences a phase shift $\phi_{\rm nl}$ that depends on the intensity of the beam.

To describe the nonlinear phase shift, consider the situation illustrated in Fig. 2.2. A strong beam of monochromatic light with complex field amplitude E_c, modifies its own propagation through a medium and exits with an accumulated nonlinear phase shift $\phi_{\rm nl}$. The total field within the medium is described by

$$\widetilde{E}(\mathbf{r},t) = E_c e^{-i\omega t} + \text{c.c.} \tag{2.1}$$

where ω is the frequency of the field and the complex amplitude E_c contains the spatial dependence of the field $e^{i\mathrm{k_c}\cdot\mathrm{r}}$.[1] The present treatment assumes that all fields have the same state of polarization, hence $\widetilde{E}$ is a scalar quantity. In general, a complete treatment considers both polarization states as described in Sec. 3.7. The effect of the medium on the propagation of this field can be described in terms of the macroscopic

[1] I adopt a notation where the tilde indicates quantities that vary at optical frequencies.

polarization of the medium

$$\widetilde{P} = \epsilon_0 \chi \widetilde{E} \tag{2.2}$$

where χ is the electric susceptibility of the medium, and ϵ_0 is the permittivity of free space. In nonlinear optics, the optical response can often be described by an expansion of Eq. (2.2) in powers of the incident field $\widetilde{E}$

$$\widetilde{P} = \epsilon_0 \left(\chi^{(1)} \widetilde{E} + \chi^{(2)} \widetilde{E}^2 + \chi^{(3)} \widetilde{E}^3 + \ldots \right). \tag{2.3}$$

For isotropic media, such as an atomic vapor, $\chi^{(2)} = 0$, so the lowest-order nonlinear term in the polarization is described by $\chi^{(3)}$ [13]. The linear and nonlinear parts of the polarization can be considered separately as

$$\widetilde{P} = \widetilde{P}^{(1)} + \widetilde{P}^{\mathrm{NL}} \tag{2.4}$$

where $\widetilde{P}^{(1)} = \epsilon_0 \chi^{(1)} \widetilde{E}$ and $\widetilde{P}^{\mathrm{NL}} = \epsilon_0 \chi^{(3)} \widetilde{E}^3$. For simplicity in treating the large number of terms that contribute to the polarization, $\widetilde{P}^{\mathrm{NL}}$ can be expressed in terms of the amplitudes $P(\omega_n)$

$$\widetilde{P}^{\mathrm{NL}} = \sum_n P(\omega_n) e^{-i\omega_n t}. \tag{2.5}$$

For the present case of a single beam, where the total incident field is given by Eq. (2.1), the polarization component of interest, $P(\omega)$, is the one with the same frequency dependence as the incident field. This component of the polarization describes the effect of the nonlinear medium on the incident field with frequency ω.[2] From

[2]There are, of course, many other components of the polarization, each with different frequency dependence including all sum and difference frequencies within $\widetilde{E}^3$.

Eq. (2.1), $\widetilde{E}^3$ contributes three terms to $P(\omega = \omega + \omega - \omega)$

$$E_c E_c E_c^*,\ E_c E_c^* E_c,\ E_c^* E_c E_c \tag{2.6}$$

where, again, the complex conjugate amplitude E_c^* is associated with frequency $-\omega$. The incident field [Eq. (2.1)] thus leads to a nonlinear polarization of the medium given by

$$P^{\mathrm{NL}} = 3\epsilon_0 \chi^{(3)} |E_c|^2 E_c. \tag{2.7}$$

The numerical factor of 3 appearing in Eq. (2.7) is known as the degeneracy factor and is given by the number of distinct permutations [Eq. (2.6)] of the frequencies contributing to P^{NL}. To determine the effect of this nonlinear polarization on the refractive index of the medium, an effective susceptibility χ_{eff} can be defined by

$$P = \epsilon_0 \chi_{\mathrm{eff}} E_c, \tag{2.8}$$

such that

$$\chi_{\mathrm{eff}} = \chi^{(1)} + 3\chi^{(3)} |E_c|^2, \tag{2.9}$$

where $\chi^{(1)}$ is the linear susceptibility of the medium. The index of refraction can be written in terms of the effective susceptibility as follows

$$n = \left(1 + \chi_{\mathrm{eff}}\right)^{1/2} = n_0 \left(1 + \frac{3\chi^{(3)} |E_c|^2}{n_0^2}\right)^{1/2} \simeq n_0 + \frac{3\chi^{(3)} |E_c|^2}{2n_0}, \tag{2.10}$$

where $n_0 = \sqrt{1 + \chi^{(1)}}$ is the background, or linear, refractive index of the medium. For

intensity $I_c = 2\epsilon_0 n_0 c|E_c|^2$, the index of refraction is then given by [13]

$$n = n_0 + n_2 I, \tag{2.11}$$

with

$$n_2 = \frac{3}{4\epsilon_0 n_0^2 c}\chi^{(3)}. \tag{2.12}$$

where c is the speed of light in vacuum and I have assumed $n_2 << n_0$ in order to ignore higher-order terms in the expansion of Eq. (2.10). The phase acquired by the beam due to this nonlinear index of refraction is given by

$$\phi_{\rm nl} = k_{\rm nl} L = \frac{n_2 I \omega L}{c}, \tag{2.13}$$

where $k_{\rm nl}$ is the nonlinear portion of the wavevector $k = n(\omega/c)L$, L is the length of the medium, ω is the optical frequency, and c is the speed of light in vacuum.

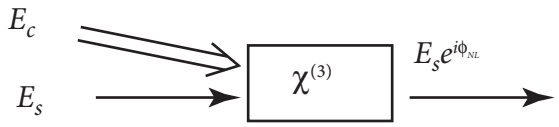

Figure 2.3: A strong beam effects the propagation of a weak beam by inducing a nonlinear phase shift, $\phi_{\rm nl}$.

Another configuration for observing the nonlinear phase shift is shown in Fig. 2.3, where a strong beam of light of amplitude E_c modifies the propagation of a weak beam of amplitude E_s. In this situation, the effect of the strong wave on the weak wave is twice as strong as the effect of the strong wave on itself. The total field for the

two-beam case is

$$\widetilde{E}(\mathbf{r},t) = E_c e^{-i\omega t} + E_s e^{-i\omega t} + \text{c.c.} \tag{2.14}$$

As above, the total field Eq. (2.14) contributes to the polarization $P(\omega = \omega + \omega - \omega)$. Now there are 6 terms in $\widetilde{E}^3$ that have frequency dependence ω

$$E_c E_c^* E_s,\ E_c^* E_c E_s,\ E_c E_s E_c^*,\ E_c^* E_s E_c,\ E_s E_c E_c^*,\ E_s E_c^* E_c. \tag{2.15}$$

The nonlinear polarization of the medium that describes the effect of the control beam E_c on the signal beam E_s is thus given by

$$P^{\text{NL}} = 6\epsilon_0 \chi^{(3)} |E_c|^2 E_s, \tag{2.16}$$

where the degeneracy factor (6) is twice that of Eq. (2.7). The extra degeneracy arises because the fields $E_c(\omega)$ and $E_s(\omega)$, despite having the same frequency, are distinguishable by propagation direction. Following a derivation along the lines of the single-beam case described above, the intensity-dependent index of refraction experienced by the weak wave due to the presence of the strong wave is given by

$$n = n_0 + 2n_2 I_c, \tag{2.17}$$

where the intensity of the control beam is given by $I_c = 2\epsilon_0 n_0 c |E_c|^2$, *i.e.*, it is the intensity of the strong wave that leads to a phase shift experienced by the weak one.

If the nonlinear medium is inserted into one arm of an interferometer, the strong wave of Fig. 2.3 can be used as a control beam, and impart a phase shift in one arm of the interferometer, thus serving to control which output port sees constructive or destructive interference. An illustration of this all-optical switching scheme is shown

in Fig. 2.4.

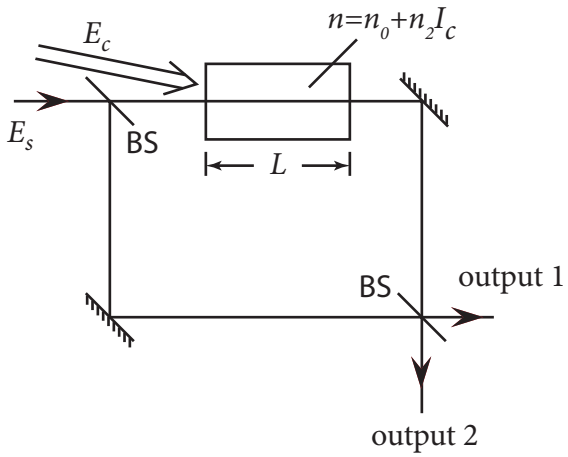

Figure 2.4: In a Mach-Zehnder interferometer, a beamsplitter (BS) splits and then combines an incident beam. Interference is detected in the two output beamsplitter ports as variations in intensity depending on the relative phase shift between the two beam paths. A nonlinear medium is inserted in one path of the interferometer to make an all-optical switch.

The following is a derivation of the interferometer output for a given nonlinear phase shift. The signal field (E_s) enters one port of the first beamsplitter, and the control field (E_c) enters medium at an angle relative to the signal field. In one arm of the Mach-Zehnder interferometer, the weak wave experiences a nonlinear refractive index, $n = n_0 + 2n_2I$. The other arm of the interferometer is linear, where the beam only experiences the usual phase shift due to propagation through a medium of index n_0. The output of the interferometer can be measured at ports 1 and 2, and is described as follows.

We first assume the following beamsplitter relations:[3]

$$r = i\sqrt{R} \tag{2.18}$$

$$t = \sqrt{T} \tag{2.19}$$

$$R + T = 1, \tag{2.20}$$

where r (t) is the reflection (transmission) coefficient for the field, and R (T) is the intensity reflection (transmission) coefficient. The output field, at port 1, can then be written as:

$$E_1 = E_s(rte^{ikL} + rte^{ik_{nl}L}), \tag{2.21}$$

with $k = n_0\omega/c$, and $k_{nl} = (n_0 + 2n_2I)(\omega/c)$ which, dropping the common phase term $\exp[in_0(\omega/c)L]$ gives:

$$E_1 = E_s(rt + rte^{i\phi_{nl}}), \tag{2.22}$$

where I have defined

$$\phi_{nl} = 2\frac{\omega}{c}n_2IL, \tag{2.23}$$

to be the nonlinear phase experienced in one arm of the interferometer. This gives the

[3]This form of the beam-splitter relation ensures that the transfer characteristics obey the Stokes relations.

output intensity at port 1:

$$\begin{aligned}|E_1|^2 &= |E_s|^2(rt + rte^{i\phi_{nl}})(r^*t + r^*te^{-i\phi_{nl}}) \\ &= |E_s|^2(|r|^2|t|^2)(1 + e^{i\phi_{nl}})(1 + e^{-i\phi_{nl}}) \\ &= 2|E_s|^2RT(1 + \cos\phi_{nl}). \end{aligned} \tag{2.24}$$

Similarly, the intensity at output port 2 is given by:

$$\begin{aligned}|E_2|^2 &= |E_s|^2(r^2 + t^2e^{i\phi_{nl}})((r^*)^2 + t^2e^{i\phi_{nl}}) \\ &= |E_s|^2(r^4 + r^2t^2e^{-i\phi_{nl}} + (r^*)^2t^2e^{i\phi_{nl}} + t^4) \\ &= |E_s|^2(R^2 + T^2 - 2RT\cos\phi_{nl}), \end{aligned} \tag{2.25}$$

where $|E_1|^2 + |E_2|^2 = |E_s|^2$.

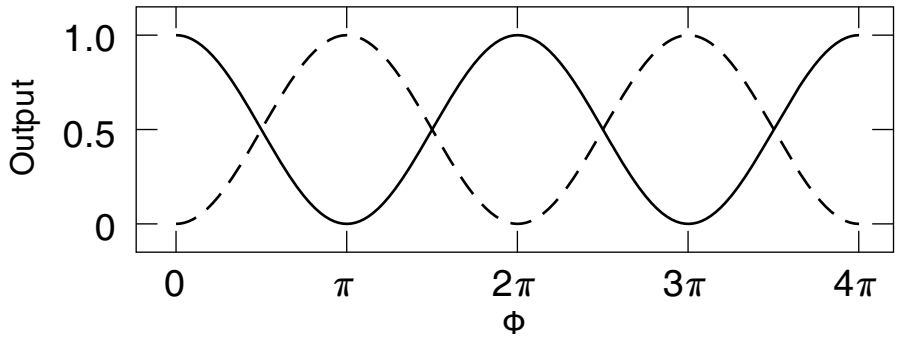

Figure 2.5: The output of the interferometer shown in Fig. 2.4. The solid line is the intensity of output port 1 as a function of phase shift $\phi_{\rm nl}$ in units of $|E_s|^2$. Similarly, the dashed line is the intensity at output port 2. For full-contrast switching, a phase shift of π is required between the two arms of the interferometer. For this figure, $R = T = 1/2$ as appropriate for 50/50 beamsplitters.

The functional form of the output intensities clearly demonstrate the sinusoidal

variation of the output intensity with ϕ_{nl}. Figure 2.5 plots the output intensities at output 1 (solid curve), and output 2 (dashed curve) of the interferometer. The sinusoidal variation with phase is clear, as is the fact that the highest contrast between the two output states is observed when $\phi_{nl} = \pi$.

To illustrate the use of this device, we consider what conditions lead to a nonlinear phase shift of $\phi_{nl} = \pi$, which is required for high-contrast switching. Silica glass is a readily available material that exhibits an intensity-dependent refractive index. The nonlinear susceptibility for silica is $\chi^{(3)} = 3.2 \times 10^{-16}$ (cm^2/W), which is not particularly large. Given Eqs. (2.17) and (2.23), an intensity of 3.9×10^{10} W/cm^2 is required for a π phase shift if the length of the nonlinear medium is only 5 cm. However, as silica glass can be drawn into optical fiber, the medium length can be made large enough to observe a significant effect with typical laser powers. Fifty kilometers of silica glass requires an intensity of 39 kW/cm^2 to achieve a full π phase shift. Light in a silica glass fiber 4 microns in diameter can reach this intensity with a few milliwatts of optical power.

The preceding discussion shows that an all-optical switch based on the nonlinear phase shift requires a nonlinear phase shift on the order of π radians. I have used realistic parameters to model this prototypical device to illustrate another point: the nonlinearity leading to a phase shift is not very strong, and the total intensity required to reach the phase shift necessary for all-optical switching in this configuration can be significant.

2.2 All-Optical Switching via Saturated Absorption

A second type of all optical switch relies on the properties of a *saturable absorber*. The absorption experienced by a wave propagating through a homogeneously-broadened

medium that exhibits saturable absorption depends on the intensity, and decreases for increasing intensity following the relation [13]

$$\alpha = \frac{\alpha_0}{1 + I/I_s}, \tag{2.26}$$

where α_0 is the absorption coefficient experienced by a weak field, I_s is a constant of the medium known as the saturation intensity defined such that when the intensity equals the saturation intensity, $I = I_s$, the absorption α is reduced to half the weak-beam value $\alpha(I = I_s) = \alpha_0/2$.[4]

Using Beer's law for absorption, it is straightforward to describe the attenuation experienced by a wave propagating through a medium with a uniform absorption coefficient α_0:

$$I(z) = I_0 e^{-\alpha_0 z}, \tag{2.27}$$

where I_0 is the intensity before entering the medium. We next modify this attenuation of the field to account for the fact that α depends on the intensity, which will allow me to describe the saturation resulting from an intense wave propagating in the medium. The goal of this derivation is to describe the effect of a strong saturating beam on the absorption experienced by a weak signal beam. This situation is illustrated in Fig. 2.6.

An intensity-dependent absorption coefficient modifies the usual Beer's law absorption Eq. (2.27) as follows. The intensity of a strong wave, which I will call the control wave $I_c(z)$ obeys

$$\frac{dI_c}{dz} = -\alpha_c I_c, \tag{2.28}$$

[4]Most materials exhibit saturable absorption, although some only for very high intensities. Some organic dye solutions and doped solids, however, exhibit reverse saturable absorption where the transmission decreases for larger intensity.

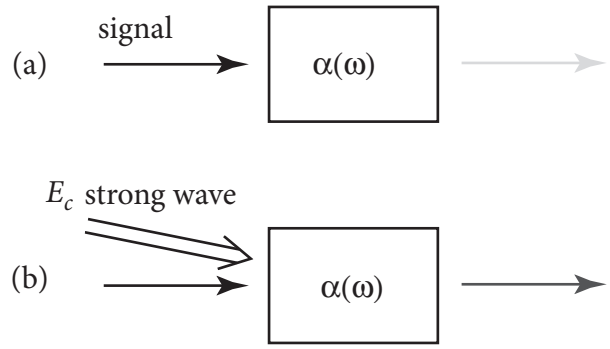

Figure 2.6: An all-optical switch based on saturable absorption. (a) The absorption experienced by the signal wave, is reduced (b) by the presence of a strong control wave that saturates the medium. The attenuation of the signal is thereby controlled by the saturating control wave.

where we have saturable absorption given by Eq. (2.26), which leads to

$$\frac{dI_c}{dz} = -\frac{\alpha_0}{1 + I_c/I_{\text{sat}}} I_c. \tag{2.29}$$

Equation (2.29) can be integrated to yield

$$\frac{I_c}{I_{\text{sat}}} + \ln(I_c) = -\alpha_0 z + A, \tag{2.30}$$

where A is a constant of integration. Exponentiation of both sides reveals that the intensity follows the form of the Lambert W function[5]

$$I_c(z) = I_{\text{sat}} \, \text{W}\left(\frac{A}{I_{\text{sat}}} e^{-\alpha_0 z}\right). \tag{2.31}$$

Finally, A can been replaced with $I_{c,0} e^{I_{c,0}/I_{\text{sat}}}$ by solving for the initial conditions, $I_c(0) =$

[5]The Lambert W function is the inverse of the function $f(w) = we^w$.

$I_{c,0}$, doing so gives

$$I_c(z) = I_{\text{sat}}\,\mathrm{W}\left(\frac{I_{c,0}}{I_{\text{sat}}}e^{\frac{I_{c,0}}{I_{\text{sat}}}-\alpha_0 z}\right). \tag{2.32}$$

Next, we consider the effect of this strong saturating wave on the transmission of a weak wave propagating through the medium with intensity $I_w(z)$. This situation is illustrated in Fig. 2.6(b). For simplicity, I will ignore the intensity grating formed by the interference of the strong and weak wave. The effects of this interference and the associated wave-mixing effects are described in the next chapter. Additionally, I assume $I_w(z) << I_{\text{sat}} < I_c(z)$, or that the weak beam is weak relative to the saturation intensity and the intensity of the control beam will typically be above the saturation intensity. These assumptions give the following expression for the absorption of the weak wave as a function of z

$$\alpha_w(z) = \frac{\alpha_0}{1+\frac{I_c(z)}{I_{\text{sat}}}}, \tag{2.33}$$

where the expression for $I_c(z)$ is given in Eq. (2.32). The intensity of the weak beam is then given by

$$\frac{dI_w}{dz} = -\alpha_w(z)I_w. \tag{2.34}$$

Which can be integrated to yield

$$I_w(z) = I_{w,0}\frac{\mathrm{W}\left(\xi e^{\xi - z\alpha_0}\right)}{\mathrm{W}\left(\xi e^{\xi}\right)} \tag{2.35}$$

with $\xi = I_{c,0}/I_{\text{sat}}$.

To evaluate the response of the absorptive switch, we first examine the behavior of Eq. (2.35). Consider the transmission of the absorbing system, defined as $T = I_w/I_{w,0}$. For various initial intensities $I_{w,0}$, the transmission is plotted as a function of optical

depth, $\alpha_0 L$ where L is the length of the medium, in Fig. 2.7. We interpret this plot as follows, a weak signal beam propagating alone experiences the largest amount of absorption, as shown by the lower solid line. A control beam with intensity equal to the saturation intensity causes the weak signal beam to experience less absorption (indicated by the dotted line). If the control beam intensity is increased to $2I_{\text{sat}}$, the signal beam experiences even less absorption (upper solid curve). Thus, in order to make a switch with large contrast between the on and off states, it is clear from Fig. 2.7 that the control beam intensity must be on the order of the saturation intensity. Furthermore, we see that the ideal optical depth corresponds to where there is the largest difference between the saturated absorption and the unsaturated absorption. It can be shown that this optimum depth is where $\alpha_0 L = 1.3$. Examining Fig. 2.7 by eye confirms that, at $\alpha_0 L = 1.3$, the saturated and unsaturated (dotted and lower-solid curves respectively) are further apart than for any other value of $\alpha_0 L$. At the optimum optical depth, $\alpha_0 L = 1.3$, the transmission of a weak beam through an unsaturated medium is 27%. In the presence of a strong beam with $I_{c,0} = I_{\text{sat}}$, the transmission increases to 47%.

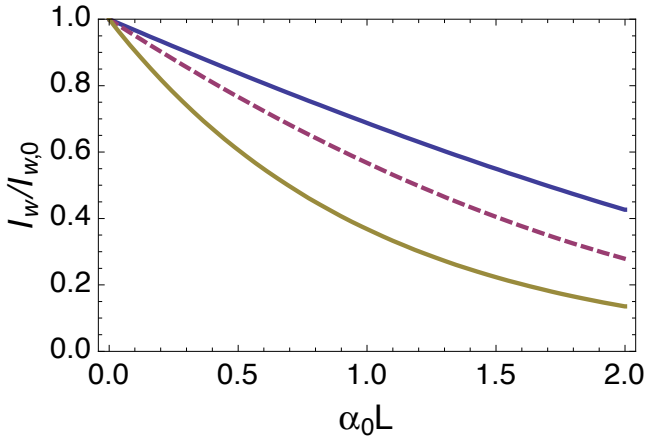

Figure 2.7: Transmission through a saturable absorber for various input intensities. The three curves are $I_{c,0} = 0.0001, 1, 2$ from bottom to top.

In order to realize the switch proposed in Fig. 2.6, the control beam intensity must

be sufficient to saturate the atomic response (*i.e.* $I_{c,0} = I_{\text{sat}}$), but we have yet to quantify I_{sat} for a generic medium. Saturation of a two-level system corresponds to moving a significant amount of the atomic population from the ground state to the excited state. In order to maintain population in the excited state, one photon must be incident on each atom per excited state lifetime. Quantitatively, this condition is [14]

$$I_{\text{sat}} = \frac{\hbar\omega}{\sigma\tau_{\text{sp}}}, \tag{2.36}$$

where τ_{sp} is the excited state lifetime, $\hbar\omega$ is the photon energy, and σ is the atomic cross section. In a material undergoing optical pumping, the relevant time scale is instead the ground-state lifetime τ_g. In an optically-pumped material, the population is redistributed in time τ_g, hence to maintain saturation, one photon must be incident on each atom per τ_g.

The cross section can be interpreted as the effective area of an atom for absorbing radiation from an incident beam of light. For a pair of isolated levels, with incident light tuned to resonance, without collisional or Doppler broadening, and assuming all atoms are optimally aligned to interact with the field, the cross section has a maximum value of [13, 14]

$$\sigma_{\text{max}} = \frac{3\lambda^2}{2\pi}, \tag{2.37}$$

where λ is the wavelength of incident light and the factor of three is replaced with unity for the case of randomly-aligned atomic dipoles [14].

The switch response plotted in Fig. 2.7 can now be evaluated for realistic conditions. A typical cloud of cold-trapped rubidium atoms satisfies the requirements for maximizing σ. The saturation intensity is determined using Eq. (2.36) and the parameters for the rubidium D_2 transition. I find $I_{\text{sat}} = 3$ mW/cm^2 for $\tau_{\text{sp}} = 25$ ns and

$\lambda = 780$ nm. Thus, for a beam with radius 2 mm, an optical power of 0.4 mW would be required to actuate a MOT-based switch, and hence change the transmission of a weak beam from 27% to 47%. Of course, one limitation of the saturation-based switch is that the weak beam must be weak relative to the saturation intensity. In the MOT case described here, the saturation intensity corresponds to a 2 mm diameter beam with $\sim$80 μW of power, hence the power of the signal beam must be much less than 80 μW, and therefore, much less than the power of the control beam.

Rather than evaluate these equations for every saturation-based switch, it is more convenient to establish a metric for comparing different all-optical switches having different geometries. The fact that the maximum atomic cross section depends only on λ leads to one such metric. To make comparisons between all-optical switches of various sizes, we quantify the energy density of the control field in units of photons per $\lambda^2/(2\pi)$. The motivation for this definition is twofold: first, as shown above, the maximum absorption cross section of a randomly-oriented two-level atom is given by $\lambda^2/(2\pi)$. Second, the minimum transverse size of an optical beam is set by the diffraction limit to be on the order of λ^2. Thus, in principle, a larger device that operates at n photons per $\lambda^2/(2\pi)$ can be scaled to the diffraction limit and operate with only n photons.

One caveat in using the energy density for comparison between various all-optical devices is that this metric does not have an implicit unit of time. Clearly one photon per $\lambda^2/(2\pi)$ per year is a very different input from one photon per $\lambda^2/(2\pi)$ per picosecond. It is thus necessary to include the switch response time to accurately compare the sensitivity of devices using the energy density metric. The switch response time is then defined such that the switch can be actuated if the specified energy density is applied for at least the duration of the response time. This caveat arises from the motivation for defining the switching energy density, which is simply to compare a large-scale

all-optical switch to a device that is geometrically optimized to operate at the limit of small optical beams: the diffraction limit.

The origin of the switching energy density metric is the calculation of the energy density required to achieve a notable decrease in the amount of absorption experienced in an ensemble of two-level atoms. A decrease in absorption occurs in an ensemble of two-level atoms if the control beam has sufficient intensity to maintain a significant fraction of the atoms in their excited state. From Eq. (2.36) and Eq. (2.37), we see this is achieved by having an input beam at the saturation intensity, or an energy density that corresponds to approximately one photon per $\lambda^2/(2\pi)$. Energy of this density must be applied for at least the lifetime of the excited state. Otherwise saturation will not occur. The assumption that saturation of the atomic transition is required for observing high-contrast all-optical switching led to the early conclusion that all-optical switches must operate with at least one photon per $\lambda^2/(2\pi)$ [6], a point that is discussed in more detail in Chapter 5.

In terms of the practical nature of the example switch based on saturable absorption, the primary drawback is the requirement that the signal beam must be very weak in comparison to the control beam. A strong signal beam would saturate the absorption itself and be transmitted regardless of the control beam. As I will discuss in the next Section, the requirement of a strong control beam limits the range of applications for a switch based on saturable absorption.

I have presented two prototypical devices that can be used for all-optical switching that use two different nonlinear mechanisms to achieve light-by-light control. The primary purpose of discussing these examples was to introduce the fundamental ideas of nonlinear phase shift, energy density, and absorption cross section. Next, I step back and present an overview of the general requirements for a practical all optical switch. The final section in this chapter is a review of recent progress in the field of all-optical

switching.

2.3 All-Optical Switching: Overview

Switches can be used in two classes of applications: information networks and computing systems. In each of these applications, information can be stored in either classical or quantum degrees of freedom. Hence the requirements for a device vary depending on the intended application.

Classical, all-optical networks require switches to reliably redirect or gate a signal depending on the presence of a control field at the device input. Ideally the switch shows large contrast between on and off output levels and can be actuated by low input powers. If the network carries quantum information, the switch must be triggered by an input field containing only a single quanta (photon). Additionally, in the quantum case, the quantum state of the transmitted signal field must be preserved.

If a switch is to be used as a logic element in a classical computing system, it must have the following characteristics: input-output isolation, cascadability, and signal level restoration [15]. Input-output isolation prohibits the device output from having back-action on the device input. Cascadability requires that a device output have sufficient power to drive the input of at least two identical devices. Signal level restoration occurs in any device that outputs a standard signal level in response to a wide range of input levels. That is, variations in the input level do not cause variations in the output level. Switching devices that satisfy these requirements are considered scalable devices, *i.e.*, the properties of the individual device are suitable for scaling from a one device to a network of many devices.

While scalability describes important properties of a switching device, sensitivity provides one way to quantify its performance. A highly sensitive all-optical switch can

be actuated by a very weak optical field. Typical metrics for quantifying sensitivity are: the input switching energy (in Joules), the input switching energy density (in photons per $\sigma = \lambda^2/2\pi$) [6, 16], and the total number of photons in the input switching pulse.

One may not expect a single device to satisfy all of the requirements for these different applications. For example, a switch operating as a logic element should output a standard level that is insensitive to input fluctuations. This may be at odds with quantum switch operation where the device must preserve the quantum state of the signal field. An interesting question arises from these requirements: What happens when a classical switch is made sensitive enough to respond to a single photon? Reaching the level of single photon sensitivity has been the goal of a large body of recent work that is reviewed below.

2.4 Previous Research on Low-Light-Level Switching

Two primary approaches to low-light-level switching have emerged, both of which seek to to increase the strength of the nonlinear coupling between light and matter. The first method uses fields and atoms confined within, and strongly coupled to, a high-finesse optical cavity. The second method uses traveling waves that induce quantum interference within an optical medium and greatly enhance the effects of light on matter.

Cavity quantum-electrodynamic (QED) systems offer very high sensitivity by decreasing the number of photons required to saturate the response of an atom that is strongly coupled to a mode of the cavity. For small-mode-volume, high-finesse cavities containing a strongly-coupled atom, even a single cavity photon can affect measurable change in the cavity transmission. Among many remarkable experiments, strongly-coupled cavity QED systems have shown nonlinear optical response to fields with much less than a single cavity photon [17], and have also demonstrated the photon blockade

effect where the arrival and absorption of one photon prevents subsequent absorption of a second photon [18]. Both of these observations imply the possible application of cavity QED systems as all-optical switching devices.

In the strong-coupling regime, the rate of coherent, reversible evolution dominates the decoherence rates for the atom-cavity system. Working in this regime, Hood *et al.* measured the transmission of a 10 pW probe beam through a cavity with linewidth $\kappa = 40$ MHz (cavity lifetime 25 ns) while cold caesium atoms were dropped through the cavity mode. When an atom is present in the cavity mode, the effect of a single cavity photon (on average), is an order of magnitude increase in cavity transmission. For 10 cavity photons, the nonlinear optical response is saturated and almost complete transmission is observed [17]. Operating with a cavity mode waist of 15 μm, a single input photon ($\lambda = 852$ nm) represents a switching energy density of $\sim 10^{-4}$ photons/σ and a total input energy of $\sim 10^{-19}$ J. As discussed in later sections, other systems have only recently operated at such high sensitivity levels.

In a similar system, Birnbaum *et al.* [18] observe an effect known as photon-blockade in analogy to the Coulomb-blockade effect observed in semiconductor charge transport. Photon-blockade in cavity QED systems exploits the anharmonic splitting of atomic energy levels for atoms strongly coupled to a high-finesse cavity. This level splitting allows the absorption of a single photon to prevent subsequent absorption of a second photon. For the probe frequency used in these experiments, the single-photon process is resonant with the lowest excited dressed-state of the atom-cavity system while the two-photon absorption process is suppressed. With an average of 0.21 photons in the cavity (mode waist $w = 23.4$ μm), the sensitivity of this system is $\sim 10^{-5}$ photons/σ, comparable to the lowest reported to date [9].

Cavity QED systems offer an extremely high sensitivity and are currently a leading candidate for nodes in a photon-based quantum-information-network. Although a sin-

gle two-level atom in free space exhibits an effect similar to photon blockade: once excited it cannot immediately absorb a second photon, interactions between single photons and single atoms in free space are exceedingly difficult to control. Hence one major achievement of cavity QED is to make the single-photon, single-atom regime accessible, stable, and repeatable. The primary drawback to integrating cavity-QED-based devices into switching networks is that the cavity system is designed to operate in a single field mode, which limits the number of input and output channels to one channel per polarization. For the photon-blockade effect, controlling the transmission of later photons requires the presence of an initial photon in the same mode. One must then discriminate between signal photons and control photons in some way other than by input mode (such as by polarization).

Of the scalability requirements for an all-optical switch, cavity QED systems do not satisfy cascadability. While coupling light into and out of an atom contained in the cavity is very efficient, all input and output signals are coupled strongly. Thus a weak input cannot have an effect on the transmission of a strong signal because the strong signal itself is coupled to the atom. The input and the output must have similar powers otherwise the stronger beam completely overrides the effect of the weaker beam. While well suited for interacting with single photons, cavity QED systems are not designed to allow single photon inputs to control strong, many-photon outputs.

A different technique for all-optical switching in cavities relies on creating and controlling cavity solitons. Cavity solitons are spatially localized structures appearing as intensity peaks in the field emitted by a nonlinear microresonator. The most recent experiments on all-optical switching with cavity solitons use vertical cavity surface emitting lasers (VCSELs) as the nonlinear cavity [19]. A VCSEL can be prepared for cavity solitons by injecting a wide holding beam along the cavity axis the cavity. A narrow beam superimposed on the larger holding beam and traveling through the

laser cavity serves as a write beam that induces a cavity soliton. Typically, the solitons persist until the original holding beam is turned off, hence this system naturally serves as a pixel-based optical memory, where solitons are written to and stored in the cavity field.

Cavity solitons in VCSEL systems are well-suited to applications in optical networks. The solitons function as pixels and can be addressed individually, alleviating the single-channel limitation of cavity QED systems. Lower sensitivity is the primary limitation of the cavity soliton systems. Although the soliton turn-on is very fast (500-800 ps), typical powers for the hold and write beams are 8 mW and 150 μW respectively. The lowest reported write beam power is 10 μW for a holding beam of 27 mW suggesting a compromise can be made to lower the required write power by increasing the hold beam power. Injecting 10 μW for 500 ps corresponds to an input pulse containing $\sim$24,000 photons, and a switching energy density of $\sim$140 photons/σ (write beam diameter 10 μm, $\lambda = 960 - 980$ nm). Extinguishing solitons (as would be required for operation as a switch) involves either cycling the holding beam or injecting a second "write" pulse out of phase to erase the soliton. Either modification adds a slight complication to the device.

In terms of the scalability criteria discussed above, cavity soliton devices satisfy the requirements of signal level restoration because the soliton intensity stabilizes to a consistent level for a large range of write beam intensities. Unlike cavity QED devices, large-area cavity soliton systems are inherently multi-mode and can be made very parallel with each potential soliton location serving as an isolated input/output channel. Cascadability may present a challenge for cavity soliton devices, however. Each cavity soliton would have to emit enough power to seed solitons in two or more subsequent devices and imaging or other beam shaping techniques may be required to properly image the output soliton into a second cavity. To the best of my knowledge

this problem has not been addressed in the literature.

In contrast to cavity systems, traveling wave approaches can operate with multi-mode optical fields and also achieve few-photon sensitivity. Recent progress in traveling-wave low-light-level nonlinear optics has been made through the techniques of electromagnetically induced transparency (EIT) [9, 20–24]. As an example, Harris and Yamamoto [16] proposed a switching scheme using the strong nonlinearities that exist in specific states of four-level atoms where, in the ideal limit, a single photon at one frequency causes the absorption of light at another frequency. To achieve the lowest switching energies, the narrowest possible atomic resonances are required which is the main challenge in implementing this proposal. Suitably narrow resonances can be obtained in complex experimental environments, for example, trapped cold atoms [9, 23–26].

Using trapped cold atoms, and the Harris-Yamamoto scheme, Braje *et al.* [23] first observed all-optical switching in an EIT medium with an input energy density of $\sim$23 photons/σ. Subsequent work by Chen *et al.* [24] confirmed that the EIT switching scheme operates at the 1 photon/σ level. Using a modified version of the Harris-Yamamoto scheme with an additional EIT coupling field, Zhang *et al.* [9] recently observed switching with $\sim$20 photons (10^{-12} W for τ_r =0.7 μs with a 0.5 mm beam diameter) corresponding to 10^{-5} photons/σ. This is the highest all-optical switching sensitivity reported to date.

Althought EIT switches are very sensitive, the input and output fields are necessarily of the same strength so the requirements for cascadability are not met. The other feature of scalable devices missing from these proposals is signal level restoration. The output level for EIT based switches is a monatonically decreasing function of input level [23], thus the output level is sensitive to variations in the input level. The signal level will not undergo any correction or restoration in passing from one device to

another.

Other low-light-level all-optical switching experiments have also been demonstrated recently in traveling-wave systems. By modifying the correlation between down-converted photons, Resch *et al.* [27] created a conditional-phase switch that operates at the single photon level. Using six-wave mixing in cold atoms, Kang *et al.* [28] demonstrated optical control of a field with 0.2 photons/σ with a 2 photon/σ input switching field ($\sim 10^8$ input photons, over $\sim$0.54 μs in a $\sim$0.5 mm diameter beam). Both of these results exhibit high sensitivity but are limited to control fields that are stronger than the output field.

Another approach combines the field enhancement offered by optical cavities with the strong coupling of coherently prepared atoms. Bistability in the output of a cavity filled with a large-Kerr, EIT medium [29] exhibits switching that is sensitive to 0.4 mW of input power over a few microseconds ($\sim 10^9$ total photons or $\sim 10^8$ photons/σ, 80 μm radius, $\sim$2 μs response time). Photonic crystal nanocavities have also shown bistability switching. Tanabe *et al.* [30] demonstrated switching with 74 fJ pulses and a switching speed of $<$ 100 ps ($\sim$500,000 photons) in a Silicon photonic crystal nanocavity system. There has also been a recent proposal to use photonic crystal microcavities filled with an ultra-slow-light EIT medium [31] as a switching platform. Simulations for such a system suggest switching could be achieved with less than 3000 photons[6]. Taking a different approach, Islam *et al.* [32] exploit a modulational instability in an optical fiber interferometer to gate the transmission of 184 mW by injecting only 4.4 μW, which corresponds to injecting less than 2,000 photons during the 50 psec switching time. Furthermore, with an effective area of 2.6×10^{-7} cm^2, this sensitivity corresponds to 24 photons/σ.

[6]Because the system has already been reduced to the minimum possible transverse dimension, the mode volume of the proposed photonic crystal microcavity is less than λ^3 and the photons/σ metric is no longer applicable to photonic crystal systems.

Many of these other systems satisfy some, but not all, of the criteria for scalability. Of the two most sensitive systems just discussed, EIT-filled photonic crystal microcavities, suffers from the same drawbacks as cold-atom EIT systems: the input and output fields are required to have the same power, making them not cascadable. The other highly sensitive system, a modulational-instability fiber interferometer, is both cascadable and exhibits signal level restoration. In several ways the latter system is similar to ours: it exploits the sensitivity of instabilities and uses a sensitive detector (in their case the interferometer, in my case pattern orientation) to distinguish states of the switch.

Finally, there has been a very recent proposal that does not use cavities or traveling optical fields, but instead takes advantage of photon-induced surface plasmons excited in a conducting nano-wire that couple strongly to a two-level emitter placed nearby. This strong coupling enables effects that are similar to those observed in cavity QED. Specifically, Chang *et al.* [33] suggest that a system consisting of a nano-wire coupled to a dielectric waveguide could be used to create an optical transistor that is sensitive to a single photon [33]. Photons in the dielectric waveguide are efficiently coupled to plasmons that propagate along the nanowire. A two-level emitter placed close to the nanowire has a strong effect on the plasmon transmission. The absorption of a single photon by the emitter is sufficient to change the nanowire from complete plasmon reflection to complete plasmon transmission.

This system is very similar in effect to cavity QED systems, with the added advantage that the input and output are separate modes and thus separate channels. There are certainly experimental challenges to implementing this proposal but there do not appear to be any fundamental limitations to its application in an optical network. If implemented as proposed, a surface-plasmon transistor could operate with single-photon input levels, and gate signals containing many photons. The strength of the gated sig-

nal is limited by the effective Purcell factor, which depends on the nano-wire diameter, and ranges from 1 to 1000 for nanowire diameters in the range of 100 to 3 nm [33]. Hence the one-photon transistor could control a signal containing up to 1000 photons, indicating such a device would be cascadable.

Many all-optical switches have been successfully demonstrated over a period spanning several decades. However, in almost every case, one or more important features is missing from the switching device. With the requirements of scalability and sensitivity in mind, this thesis reports on a new approach to all-optical switching.

2.4.1 Switching with Transverse Optical Patterns

My approach to all-optical switching is to exploit collective instabilities that occur when laser beams interact with a nonlinear medium [5]. One such collective instability occurs when laser beams counterpropagate through an atomic vapor. In this configuration, given sufficiently strong nonlinear interaction strength, it is known that mirrorless parametric self-oscillation gives rise to stationary, periodic, or chaotic behavior of the intensity [34, 35] and/or polarization [36–38].

Another well-known feature of counterpropagating beam instabilities is the formation of transverse optical patterns, *i.e.*, the formation of spatial structure of the electromagnetic field in the plane perpendicular to the propagation direction [5, 39]. This is also true for my experiment where a wide variety of patterns can be generated, including rings and multi-spot off-axis patterns in agreement with previous experiments [38–40].

Building an all-optical switch from transverse optical patterns combines several well-known features of nonlinear optics in a novel way. Near-resonance enhancement of the atom-photon coupling makes my system sensitive to weak optical fields. Using

optical fields with a counterpropagating beam geometry allows for interactions with atoms in specific velocity groups leading to sub-Doppler nonlinear optics without requiring cold atoms. Finally, using the different orientations of a transverse pattern as distinct states of a switch allows me to maximize the sensitivity of the pattern forming instability. Instabilities, by nature, are sensitive to perturbations, so by combining instabilities with resonantly-enhanced, sub-Doppler nonlinearities I created a switch with very high sensitivity.

Before describing my experimental setup and results, it is important to include a more complete background for the treatment of optical interactions in nonlinear media. Specifically, there are several fundamental concepts that are important to understanding the origin of transverse pattern formation in nonlinear optics. The following chapter presents a basic model for the interaction between light waves in nonlinear media.

Chapter 3

Pattern forming nonlinear optics

Transverse optical patterns are fundamental to the operation of the all-optical switch I present in this thesis. This chapter serves to outline the minimum ingredients needed to observe transverse patterns in a nonlinear optical system.

The primary requirement for transverse pattern formation is a mechanism that provides gain for the portion of a wave that propagates with an off-axis wavevector. If such off-axis gain is large enough, the stable state of plane-wave, or gaussian-beam propagation can become unstable and exhibit growth of off-axis components. These off-axis components results in transverse field structure that can be observed as an intensity pattern in the far field. An example pattern, shown in Fig. 3.1, is the set of six spots that I typically observe in my experiment. Since the patterns I use for all-optical switching exhibit hexagonal symmetry, the ultimate goal of this chapter is to demonstrate the necessary ingredients for a model that exhibits hexagonal pattern formation.

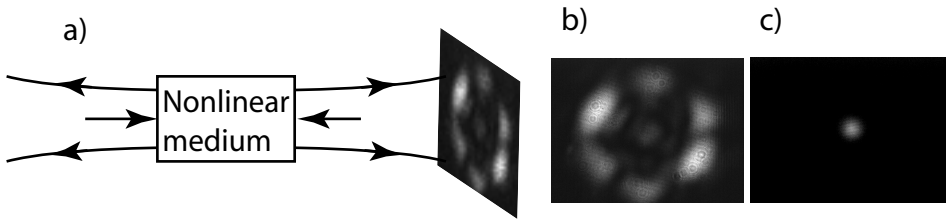

Figure 3.1: Beams counterpropagating through a nonlinear medium give rise to transverse structure in the field in the plane perpendicular to the direction of propagation. a) Beams and nonlinear medium. b) Hexagonal pattern. c) Pump beam transmitted off-resonance (for reference)

Many optical systems exhibit pattern formation through various mechanisms. As an

example, a single laser beam propagating through a gas of sodium atoms will exhibit transverse pattern formation if the beam intensity is large enough [41]. However, for a pattern-forming system to be applicable to ultra-low-light all-optical switching, the power required for pattern generation should be minimized. The use of two beams in the counterpropagating geometry serves to reduce the intensity required for the generation of transverse patterns [42], as will be shown near the end of this chapter. Hence, two beams counterpropagating through a nonlinear medium form the specific class of pattern forming systems that are the focus of the following sections.

Throughout the past thirty years there have been several dozen experimental investigations of counterpropagating beam instabilities that explore the system's rich nonlinear nature and large parameter space (see Ref. [42] and references therein). Although the large number of possible beam configurations and experimental conditions have only been partially investigated, the observed instabilities exhibit several generic features such as periodic and chaotic power fluctuations, polarization and amplitude bistability, and off-axis pattern generation.

Different theoretical treatments account for each of these features independently but few theories explain all of them simultaneously. The primary difficulty lies in describing the details of the nonlinear response to the applied field. A reasonable approximation is to treat the medium as a Kerr medium, with an intensity-dependent refractive index $n = n_0 + n_2 I$. The Kerr model, by including only intensity-dependent terms, ignores nonlinearities above third-order. It also assumes a transparent medium, *i.e.*, one with no absorption. Despite these approximations, this model has been very successful at describing a wide range of nonlinear phenomena [13]. In certain cases, such as near an atomic resonance, other models of the nonlinear medium have better quantitative accuracy, but often exhibit qualitative features that are similar to those described by Kerr nonlinearity. Finally, the Kerr model is well studied and, as the

following sections show, it includes sufficient details of the nonlinear optical interaction to account for the generation of transverse optical patterns in a counterpropagating-beam system.

In a Kerr medium, an instability that occurs on the pump-beam axis can be described by a one dimensional theory (along the pump beam direction). However, for instabilities that generate light off-axis, accurate descriptions require the inclusion of transverse dimensions, or, at a minimum, one beam with a transverse component. A further complication is that many of the standard nonlinear optics approximations are not valid when the frequency of an optical field is tuned close to an atomic resonance, or when the vector nature of the field significantly changes the nonlinear interaction. For atomic vapors, the nonlinear response is due to optical pumping. When the incident intensity is sufficient to transfer population among the atomic states, the level populations must be included in a model for it to be quantitatively accurate. Some of these issues have been addressed in the various theoretical treatments that describe features of counterpropagating beam instabilities and the text below summarizes several important treatments that successfully capture the important features of counterpropagating beam systems.

Considering on-axis instabilities in the scalar approximation, where the vector nature of the electric field is neglected and the nonlinear atomic polarization is assumed to follow the form $P^{\mathrm{NL}} = \epsilon_0 \chi^{(3)} E^3$, Silberberg and Bar-Joseph [34] found that counterpropagating beams become unstable, exhibiting periodic and chaotic intensity fluctuations.[1] Extensions of this result by Kaplan and Law [43] that allow for two field polarizations show on-axis polarization bistability that has since been experimentally verified [38].

[1] Here, ϵ_0 is the permittivity of free space, $\chi^{(3)}$ is the third-order nonlinear susceptibility and E is the electric field amplitude, all in SI units.

Off-axis generated light is described in an early treatment of counterpropagating beams by Yariv and Pepper [44] where they propose an interaction now known as mirrorless parametric oscillation in which the gain in a parametric process diverges. Infinite gain indicates that vacuum fluctuations in the field can seed the generation of new beams of light. Depending on phase-matching conditions, these beams can emerge at an angle θ to the pump-beam axis, making this interaction one possible mechanism for generating off-axis patterns [40]. However, the generated light described by mirrorless parametric oscillation in [44] is in the same state of polarization as the pump beams, which is not the case for all experimental results (see [45] and references therein).

To account for the generation of cross-polarized fields with transverse wavevector components, a more complete theoretical treatment must be used. Gaeta and Boyd [42] consider the tensor properties of the nonlinear interaction and specify the thresholds for both amplitude and polarization instabilities with wavevector components in the transverse plane.

Finally, it should be noted that the majority of the stability analyses appearing in the literature are for equal-amplitude pump waves. For imbalanced pump waves, oscillatory instabilities can occur in addition to exponential-growth instabilities [42], which would suggest that unbalanced pump beams reproduce qualitatively similar results with quantitatively different instability thresholds. Additionally, off-axis cross-polarized generated light is expected and experimentally confirmed for unbalanced pump beam powers [12, 38, 46].

In the remaining sections of this chapter, I first describe a simple estimate for the angle θ between pump beams and generated off-axis beams. This estimate is based on the phenomena of weak-wave retardation that was discussed in Sec. 2.1. Following this estimate, I present three treatments, each of which includes new physics and

describes an additional aspect of transverse pattern formation. I begin with the treatment of Yariv and Pepper and introduce the physical process known as backward four-wave mixing (BFWM) which can be used to describe gain experienced by an off-axis beam. Following this, I introduce forward four-wave mixing (FFWM) and then review the treatment by Grynberg and Paye that includes both FFWM and BFWM effects to describe the finite pattern angle observed in counterpropagating beam systems (see Fig. 3.1). Finally, I discuss the model considered by Firth and Paré in which FFWM, BFWM, cross-coupling and transverse dimensions are simultaneously considered. Although this model remains simple by assuming scalar fields, an instantaneous nonlinear response, and no absorption, it demonstrates that transverse effects and counterpropagation are sufficient to result in spatial and temporal instabilities. Furthermore, as I show in Chapter 6, this model exhibits patterns and switching behavior that are qualitatively similar to those I observe experimentally.

3.1 Weak-wave retardation

From the discussion in Sec. 2.1, we are familiar with the idea of weak-wave retardation. Originally discussed by Chiao [47], weak-wave retardation describes the phenomena that the nonlinear index of refraction experienced by a weak wave due to a strong wave is twice as large as the the nonlinear index of refraction experienced by a single strong wave due to the self nonlinear phase shift. The origin of this effect is the degeneracy factor in the description of the electric polarization of the material, and hence the two beams must be distinguishable either in frequency or propagation direction (or both). Because a strong wave and a weak wave experience different indices of

refraction, they will necessarily have different propagation vectors

$$k_{w,s} = n_{w,s}\omega/c, \tag{3.1}$$

where

$$n_w = n_0 + 2n_2 I \tag{3.2}$$

$$n_s = n_0 + n_2 I, \tag{3.3}$$

(for the derivation, see Sec. 2.1). For a process involving weak waves, such as those generated by a pattern forming instability, and strong waves, such as the pump beams driving the system, weak-wave retardation provides the following simple argument for why the generated beams propagate at an angle to the pump beams.[2]

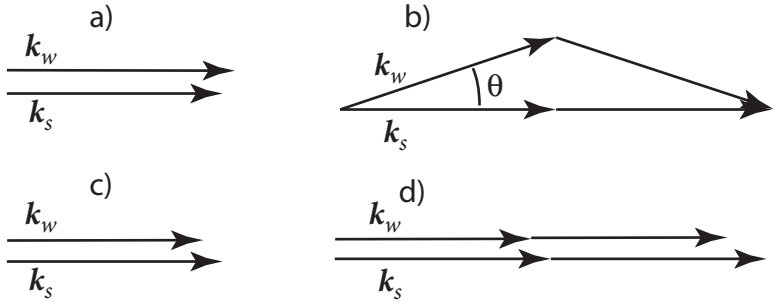

Figure 3.2: Weak-wave retardation provides an estimate for the phase-matching angle θ for a forward process involving a strong wave with wavevector k_s and a weak wave with wavevector k_w. a) For $n_2 > 0$, k_w is longer than k_s. b) k_w and k_s propagate at an angle θ. c) For $n_2 < 0$, k_w is shorter than k_s, and d) the process cannot be phase matched for any angle.

Consider two waves, one weak and one strong, with wavevectors k_w, and k_s respectively. If we assume the weak wave is generated by a wave-mixing process that

[2]It should be noted that I am not assuming anything about the mechanism of this instability, simply that some physical process involving forward-moving beams gives rise to weak fields and requires the generated fields be phase-matched in order for the process to occur efficiently. Specifically this process is known as forward four-wave mixing and is discussed in more detail in Sec. 3.3.

requires it to be phase matched with a strong pump wave propagating along the z-axis, then their projections along the z-axis must be equal. This is illustrated in Fig. 3.2. If the nonlinear refractive index is positive ($n_2 > 0$) the weak wave will have a longer k-vector due to the larger nonlinear refractive index and must propagate at an angle θ to the pump-beam axis z. We now estimate θ for a system that exhibits a nonlinear phase shift $k_s^{\mathrm{NL}} L = \pi/2$, where I define $k_s = k_0 + k_s^{\mathrm{NL}}$ as a sum of linear and nonlinear contributions to the wavevector. Recall from Sec. 2.1 that a relative phase shift of $\phi = \pi/2$ is required for an all-optical switch based on the nonlinear phase shift.

From geometrical arguments based on Fig. 3.2, we begin with

$$\cos\theta = \frac{k_s}{k_w}. \tag{3.4}$$

Separating the linear and nonlinear contributions to the wavevector gives

$$\cos\theta = \frac{k_0 + k_s^{\mathrm{NL}}}{k_0 + k_w^{\mathrm{NL}}}, \tag{3.5}$$

where the nonlinear phase shift experienced by the strong wave corresponds to $k_s^{\mathrm{NL}} = \pi/2L$. Weak wave retardation thus implies the phase shift experienced by the weak wave is twice a large, hence $k_w^{\mathrm{NL}} = \pi/L$. Finally, from $k_0 = n_0\omega/c \simeq 2\pi/\lambda$, where I have approximated[3] $n_0 \simeq 1$, we have

$$\cos\theta = \frac{\frac{2\pi}{\lambda} + \frac{\pi}{2L}}{\frac{2\pi}{\lambda} + \frac{\pi}{L}} = \frac{1 + \frac{\lambda}{4L}}{1 + \frac{\lambda}{2L}} \simeq 1 - \frac{\lambda}{4L}, \tag{3.6}$$

[3]The approximation $n_0 \simeq 1$ is valid for a dilute vapor. If the nonlinear medium were a transparent solid, n_0 would have a value greater than unity.

where I have assumed that $\lambda << L$. The small angle approximation is valid in this case, and thus

$$1 - \frac{\theta^2}{2} \simeq 1 - \frac{\lambda}{4L}$$

$$\theta \simeq \sqrt{\frac{\lambda}{2L}}. \tag{3.7}$$

If I substitute my experimental values, $\lambda = 780$ nm and $L = 5$ cm, into Eq. (3.7), I find that $\theta \simeq 2.8$ mrad. This agrees qualitatively with what is measured in experiments (typically in the range of 2-4 mrad). Weak-wave retardation thus provides a good estimate for the origin of off-axis effects in wave mixing processes. The following sections outline such processes in more detail, and demonstrate their specific roles in the formation of transverse patterns.

3.2 Backward four-wave mixing

Backward four-wave mixing in a nonlinear medium, illustrated in Fig. 3.3, can be described in terms of a diffraction grating induced by the interference between two beams. In the case illustrated, a forward (right-moving) probe wave with amplitude A_3 interferes with a backward-moving pump wave, amplitude A_2, propagating at an angle θ to the z-axis. The intensity pattern due to this interference gives rise to a spatial variation of the index of refraction via the nonlinear index of refraction $n = n_0 + n_2 I$. A second pump wave, propagating in the forward direction, scatters off the index grating, into the direction opposite the incident probe.

To examine the origins of gain in backward four-wave mixing (BFWM), consider the situation illustrated in Fig. 3.4, where two pump waves counterpropagate through

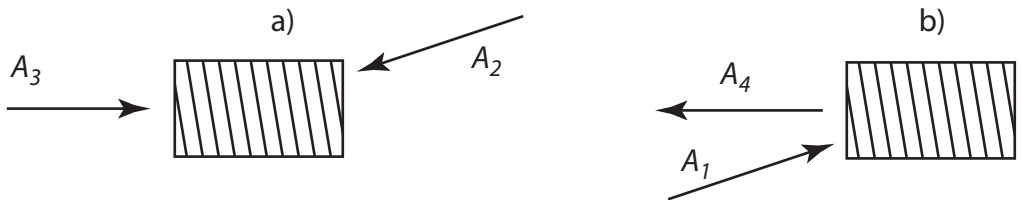

Figure 3.3: Backward four-wave mixing in a nonlinear medium. a) An intensity grating established by the interference of one pump wave, A_2 incident from the right, and the signal wave, A_3 incident from the left, creates a refractive index grating. b) The second pump wave A_1, incident from the left, scatters off the index grating to provide the conjugate beam A_4, which exits the medium to the left.

a nonlinear medium at an angle to the z-axis and a second pair of waves counterpropagate along the z-axis. The fields are taken to be degenerate plane waves with frequency ω, and can be represented by

$$\widetilde{E}_i(\mathbf{r},t) = E_i(\mathbf{r})e^{i\omega t} + \text{c.c.} \tag{3.8}$$

$$= A_i(\mathbf{r})e^{i(\mathbf{k_i}\cdot\mathbf{r}-\omega t)} + \text{c.c.}, \tag{3.9}$$

for $i = 1,2,3,4$, where $A_i(\mathbf{r})$ describes the slowly varying envelope for each wave. With counterpropagating waves, we have

$$\mathbf{k_1} + \mathbf{k_2} = 0, \quad \mathbf{k_3} + \mathbf{k_4} = 0. \tag{3.10}$$

If the signal and conjugate fields remain weak, it is reasonable to ignore the modification of the pump waves due to the nonlinear interaction. This model also ignores the effects of weak-wave retardation. Furthermore, by considering only the waves indicated in Fig. 3.4, the forward four-wave mixing is also ignored. Phase matching, which enters the analysis for forward four wave mixing, is automatic in the backward geometry. The expression given in Eq. (3.10), indicates that BFWM is automatically phase matched. These assumptions lead to the following four expressions for the nonlinear

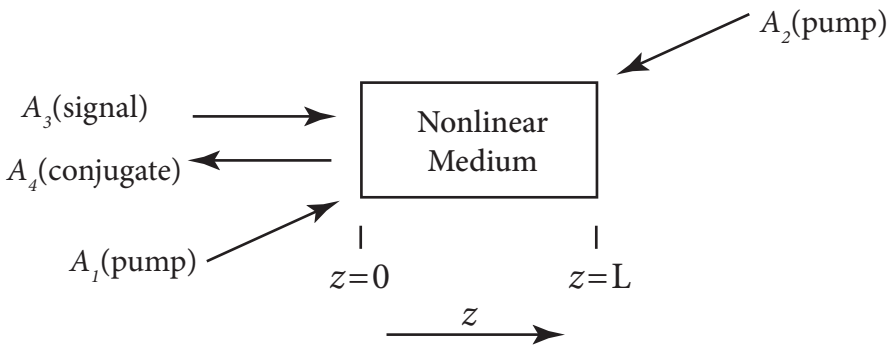

Figure 3.4: Four wave mixing in the phase conjugate geometry. Two strong pump waves with amplitudes A_1 and A_2 counterpropagate through a nonlinear medium and at an angle to the z-axis. An incident wave propagating along z with amplitude A_3 undergoes phase conjugate reflection and a fourth wave with amplitude A_4 exits the medium propagating along $-z$.

polarization produced by the fields in the medium

$$P_1 = P_2 = 0, \quad P_3 = 6\epsilon_0 \chi^{(3)} E_1 E_2 E_4^*, \quad P_4 = 6\epsilon_0 \chi^{(3)} E_1 E_2 E_3^*. \tag{3.11}$$

Each of the interacting waves obeys the wave equation in the form

$$\nabla^2 \widetilde{E}_i - \frac{n^2}{c^2} \frac{\partial^2 \widetilde{E}_i}{\partial t^2} = \frac{1}{\epsilon_0 c^2} \frac{\partial^2 \widetilde{P}_i}{\partial t^2}, \tag{3.12}$$

where n is the linear index of refraction in the medium. We see that the nonlinear polarization $\widetilde{P}_i$ acts as a source term driving the wave equation. Physically, this indicates the role of the polarization in generating new waves. In general, the generated waves may have wavevectors that are not present in the incident fields. It is clear that each term P_i of the polarization given in Eq. (3.11) drives the wave equation and gives rise to waves that couple to E_i. Thus, the nonlinear polarization of the medium plays the role of coupling the four interacting waves. This coupling can be determined by solving Eq. (3.12) in the slowly varying amplitude approximation, and neglecting the

depletion of the pumps. The result is a pair of amplitude equations for the signal and conjugate waves [44]

$$\frac{dA_3}{dz} = i\kappa A_4^* \tag{3.13}$$

$$\frac{dA_4}{dz} = -i\kappa A_3^*, \tag{3.14}$$

where

$$\kappa = \frac{3\omega}{nc}\chi^{(3)}A_1A_2, \tag{3.15}$$

is the coupling coefficient.

A physically interesting case is that of a single input $A_3(0)$ at $z = 0$, and $A_4(L) = 0$. This corresponds to injecting both pump waves, and the signal wave, in order to observe the output spontaneously generated as the fourth wave, which is typically called the conjugate wave for this geometry. In this case the reflected (conjugate) wave at the input ($z = 0$) is

$$A_4(0) = i\left(\frac{\kappa}{|\kappa|}\tan|\kappa|L\right)A_3^*(0), \tag{3.16}$$

and the transmitted wave at $z = L$ is

$$A_3^*(L) = \frac{A_3^*(0)}{\cos|\kappa|L}. \tag{3.17}$$

The most significant implication of this result is that the gain for the transmitted wave given by Eq. (3.17) is infinite when $|\kappa|L = \pi/2$. The same is true for the reflected wave given by Eq. (3.16). Physically, this implies that the presence of even a single photon in the mode corresponding to $A_3(0)$ is sufficient to generate a macroscopic field at $A_3(L)$. This infinite gain (and reflectivity) is one origin off-axis beams generated

by four-wave mixing processes. The spontaneous generation of this off-axis beam is known as mirrorless parametric oscillation. This analysis has only allowed for the possibility of four plane waves interacting in the system, and conditions exist whereby quantum fluctuations are sufficient to induce new beams of light. The next section introduces another wave-mixing process known as forward four-wave mixing (FFWM). Later sections show that including FFWM in the model of a counterpropagating beam system serves to reduce the gain necessary for self-oscillation and determines the angle at which oscillation occurs.

3.3 Forward four-wave mixing

The treatment of Yariv and Pepper specified only enough fields to allow for the possibility of backward four-wave mixing. However, there is another four-wave mixing process with a different geometry that plays a role in generating off-axis fields. Known as forward four-wave mixing, this process takes place between three fields that propagate in the forward direction and are mutually coupled, giving rise to gain in the off-axis beams. The forward four-wave mixing process is illustrated in Fig. 3.5.

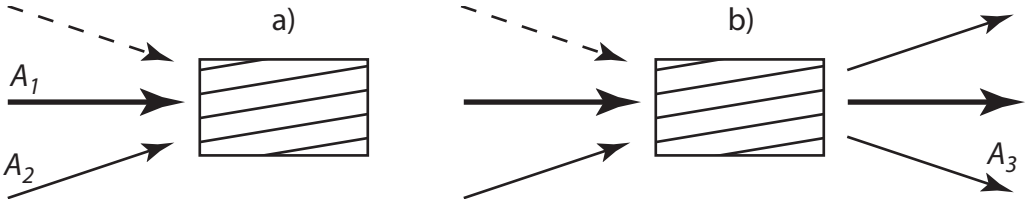

Figure 3.5: Forward four-wave mixing geometry. A strong pump wave with amplitude A_1 propagates through a nonlinear medium along the z-axis. Two other incident waves, typically taken to be weak probe waves, propagate at an angle to the z-axis with amplitudes A_2 and A_3.

The parametric FFWM process is illustrated in Fig. 3.5 where a strong pump wave with amplitude A_1 propagates along the z-axis and a probe wave with amplitude A_2

is incident on the nonlinear medium at a small angle θ. The dashed arrow indicates a second probe wave, also incident at a symmetric angle θ to the pump wave. To account for FFWM in theoretical treatments, this probe wave must be included initially, but can later be set to have zero incident amplitude. Forward four-wave mixing is the interaction between A_1 and A_2 that gives rise to gain in the direction of A_3. In the grating picture, the pump and probe wave interfere to induce the grating indicated in Fig. 3.5. The pump wave can then scatter off this grating into the direction of A_3.

Treating the coupling between the fields shown in Fig. 3.5 begins with an expression for the nonlinear polarization analogous to that given in Eq. (3.11). Phase matching is not automatic as it was for the backward geometry; hence, an additional term describes the phase mis-match and the polarization that gives rise to A_3 is given by

$$P_3 = 6\epsilon_0 \chi^{(3)} E_1 E_1 E_3^* \exp\left[i\left(\vec{k}_1 + \vec{k}_1 - \vec{k}_3\right)\cdot\vec{r} - i\omega t\right]. \tag{3.18}$$

Just as in BFWM, each of the interacting waves shown in Fig. 3.5 obeys the wave equation given in Eq. (3.12). The coupling of the three waves is determined by solving (3.12) in the slowly-varying amplitude approximation, and neglecting the depletion of the pumps. The result if a pair of amplitude equations for the two weak waves A_2 and A_3

$$\frac{dA_3}{dz} = i\kappa A_2^* \exp(i\Delta k z) \tag{3.19}$$

$$\frac{dA_2}{dz} = i\kappa A_3^* \exp(i\Delta k z), \tag{3.20}$$

where $\Delta k = (2\vec{k}_1 - \vec{k}_2 - \vec{k}_3)\cdot\hat{z}$ is the component of the wavevector mis-match along

the z-axis, and

$$\kappa = \frac{3\omega}{nc}\chi^{(3)}A_1^2, \tag{3.21}$$

is the FFWM coupling coefficient.

Given the waves illustrated in Fig. 3.5, a physically interesting case is that of only one incident off-axis wave, *i.e.*, $A_3(0) = 0$ and only the forward pump $A_1(0)$ and $A_2(0)$ are nonzero. The solution to Eqs. (3.19), subject to these boundary conditions, is given by

$$A_3(z) = e^{i\Delta kz}\frac{i\kappa}{g}A_2^*(0)\sinh(gz) \tag{3.22}$$

$$A_2(z) = e^{i\Delta kz}A_2(0)\left[\cosh(gz) - \frac{i\Delta k}{2g}\sinh(gz)\right], \tag{3.23}$$

where

$$g = \sqrt{|\kappa|^2 - \left(\frac{\Delta k}{2}\right)^2}, \tag{3.24}$$

is a coefficient that describes the gain experienced by both off-axis waves.

The behavior of the amplitude equations give in Eqs. (3.22) is not as obvious as it was in the case of the BWFM amplitude equations (Eqs. (3.16) and (3.17)). For this reason, it is useful to consider a specific case and plot the amplitude as a function of position z. The three parameters to consider are the initial amplitude of the weak injected wave $A_2(0)$, the coupling parameter κ, and the phase mismatch Δk. I have shown in Sec. 3.1 that weak-wave retardation can serve to phase-match the forward four-wave mixing process at a specific angle θ between the pump-beam and the off-axis beams. For the purpose of illustration, I will assume this is the case and that the forward four-wave mixing process is phase-matched so that $\Delta k = 0$. An appropriate

value for the nonlinear coupling can be determined by setting $\kappa L = \pi/4$. This is half the value of κL required for self-oscillation in the Yariv and Pepper treatment, but as the following sections will show, $\kappa L = \pi/4$ is near the threshold condition when both FFWM and BFWM processes are considered simultaneously.

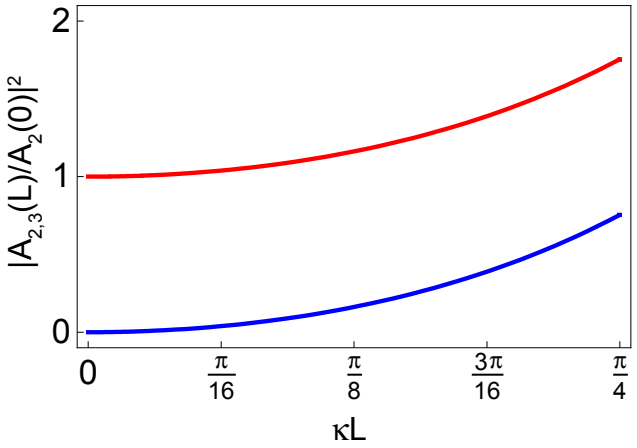

Figure 3.6: The off-axis amplitudes for forward four-wave mixing. The weak injected beam with amplitude $A_2(z)$ (upper curve) experiences gain, and a symmetric off-axis wave with amplitude $A_3(z)$ (lower curve) is generated and grows as it propagates in the medium. The amplitudes are given by Eq. 3.22 with $\Delta k = 0$, $A_2(0) = 1$ and $A_3(0) = 0$.

Figure 3.6 illustrates the gain experienced by both off-axis waves A_2 and A_3. The initial amplitude $A_2(0) = 1$ experiences gain as it propagates through the medium. Additionally, the other off-axis wave, with amplitude $A_3(0) = 0$, is generated by the interaction and grows with increasing z as well (lower curve in Fig. 3.6). I have assumed the FFWM process is phase matched in this example, but if this is not the case, *i.e.*, if the injected wave is propagating at an angle larger than $\theta \simeq \sqrt{\lambda/2L}$ then the coefficient g decreases for increasing Δk.

The processes I have considered thus far, BFWM and FFWM, can easily occur simultaneously for beams that propagate with small θ such that the FFWM process can be phase-matched or nearly phase-matched. By considering the combination of the

FFWM process and the BFWM process, Grynberg extends the analysis of Yariv and Pepper [48, 49] as described in the following section.

3.3.1 Coherent addition of FFWM and BFWM

In a straightforward extension of the work of Yariv and Pepper, Grynberg demonstrated that including a second probe wave allows both forward and backward four-wave mixing processes to contribute to mirrorless oscillation [48]. The treatment in [48] is a more rigorous version of the arguments I presented above based on weak-wave retardation. Grynberg shows that using the established expressions for the weak- and strong-beam susceptibilities, rather than my estimated phase shift of $\pi/2$, weak-wave retardation causes the forward four-wave mixing process to be phased matched at a specific angle. The result, however, is very similar to my estimate and predicts θ on the order of a few miliradians depending on specific system parameters.

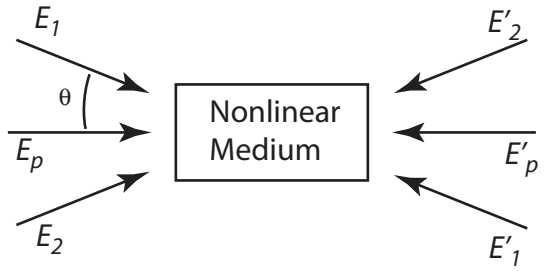

Figure 3.7: Forward- and Backward-four-wave-mixing add coherently to determine θ. The theoretical treatment of both FFWM, and BFWM requires the consideration of six waves. Two counterpropagating pump waves, E_p and E'_p, and two pairs of counter-propagating probe waves, E_1 (E'_1) and E_2 (E'_2). θ is the angle between the probe waves and the pump waves.

In a more quantitatively complete treatment, Grynberg and Paye include FFWM, BFWM, and a third parametric wave-mixing processes that occurs in the geometry shown in Fig. 3.7 [49]. By considering six waves, this treatment explicitly allows both forward and backward wave mixing processes to occur. Furthermore, the stability of

the amplitude equations derived for the four probe waves can be evaluated as a function of the angle θ. Such a stability analysis shows several key features. First, the threshold for mirrorless self-oscillation is infinite for $\theta = 0$ implying that no oscillation is possible on the pump beam axis. This is consistent with Silberberg and Bar-Joseph because the fields treated here are degenerate, whereas Silberberg and Bar-Joseph considered coupling between non-degenerate fields, and predicted no instability for the degenerate case [50]. Second, the lowest threshold occurs for a unique value of θ and corresponds to $|\kappa|L = \pi/4$, a factor of 2 smaller than the threshold predicted by Yariv and Pepper. For large θ, the threshold tends toward $|\kappa|L = \pi/2$, the value predicted by Yariv and Pepper, implying that forward four-wave mixing is not important to the analysis for large θ. For large θ, only backward four-wave mixing can be phase matched.

Not only is the instability threshold lower in the model that includes both FFWM and BFWM, but the phase-matching condition for the FFWM process specifies a unique angle θ where BFWM and FFWM coherently add, thus implying that mirrorless parametric oscillation occurs with conical emission [49].

3.4 Transverse patterns

The treatments of counterpropagating waves presented above have assumed only plane-wave optical fields with distinct wave vectors. Firth and Paré extend these treatments by deriving amplitude equations that include the transverse components of the field for counterpropagating fields in a nonlinear medium. By including the transverse degrees of freedom and allowing for multiple four-wave-mixing interactions, they show that transverse effects and counterpropagating pump beams are sufficient ingredients for the system to exhibit spatio-temporal instability [10]. Furthermore, with the in-

clusion of transverse components, the threshold for self-oscillation can be significantly lower than that originally shown by Yariv and Pepper, and comparable to that shown by Grynberg and Paye.

In fact, there are many similarities between the analyses of Grynberg and Paye and Firth and Paré. Both models include FFWM, BFWM, and other parametric interactions. Rather than assuming a pair of probe waves at angle θ to the pump-beam axis, as in [49], Firth and Paré treat one longitudinal dimension, and one continuous transverse dimension with off-axis effects included by analyzing the stability of the wave equation to perturbations with a general wavevector K. This treatment can thus be easily generalized to two transverse dimensions. For this reason, it serves as the basis for my numerical simulations presented in Chapter 6.

3.4.1 Model of Firth and Paré

The interaction considered in this section is familiar from earlier sections, and illustrated in Fig. 3.8. To study the origin of transverse pattern formation, we consider waves that satisfy Maxwell's equations under the following simplifying assumptions. If the nonlinear medium is isotropic, dispersionless, and the waves propagate primarily along one axis, the wave equation can again be taken to have the form shown in Eq. (3.12). Consider two waves that counterpropagate through a nonlinear medium

and are described by

$$\widetilde{E}_F(\mathbf{r},t) = E_1(\mathbf{r},t)e^{-i\omega t} + \text{c.c.}$$

$$= F(\mathbf{r},t)e^{i(kz-\omega t)} + \text{c.c.} \tag{3.25}$$

$$\widetilde{E}_B(\mathbf{r},t) = E_2(\mathbf{r},t)e^{-i\omega t} + \text{c.c.}$$

$$= B(\mathbf{r},t)e^{i(-kz-\omega t)} + \text{c.c.}, \tag{3.26}$$

where $k = n_0\omega/c$, E_i is a field amplitude with spatial dependence e^{ikz}, and $F(B)$ is a slowly varying amplitude describing the forward (backward) wave.

Figure 3.8: Two waves with amplitudes $F(\mathbf{r},t)$ and $B(\mathbf{r},t)$ counterpropagate within a nonlinear medium.

To go from the wave equation to a quantitative description of the field amplitudes in a counterpropagating beam system, we substitute Eq. (3.25) into Eq. (3.12) and match terms that exhibit the same spatial dependence as the pump beams, thus coupling the waves generated by the nonlinear polarization to the pump waves. The primary difference between this analysis and that of Grynberg and Paye is that the latter considers only two specific probe-beam wavevectors, and here all transverse wavevectors are allowed in the model, and treated as a Fourier decomposition.

There are many possible terms that contribute to the polarization $\widetilde{P}_i$, but most of them do not couple strongly to either of the pump waves and are thus neglected. The

two terms that provide coupling between the pump waves are

$$P_1 = 3\epsilon_0 \chi^{(3)} \left(E_1^2 E_1 + 2E_1 E_2 E_2^* \right) \tag{3.27}$$

$$P_2 = 3\epsilon_0 \chi^{(3)} \left(E_2^2 E_2 + 2E_2 E_1 E_1^* \right), \tag{3.28}$$

where P_1 (P_2) generates a wave that couples to E_1 (E_2). Using the expressions for the incident waves Eq. (3.25), these polarization terms, when substituted into Eq. (3.12) yield amplitude equations for the forward and backward fields. In doing so, it is usually permissible to make the slowly-varying amplitude (SVA) approximation, which is valid as long as

$$\left| \frac{d^2 E_{1,2}}{dz^2} \right| << \left| k_{1,2} \frac{dE_{1,2}}{dz} \right|. \tag{3.29}$$

The SVA approximation, which applies to the present situation of continous-wave counterpropagating fields, implies that the fractional change in the field amplitude over a single wavelength is much smaller than unity [13]. Under the SVA approximation, the forward and backward fields are described by the following amplitude equations

$$\frac{\partial F}{\partial z} + \frac{n_0}{c} \frac{\partial F}{\partial t} - \frac{i}{2k} \frac{\partial^2 F}{\partial x^2} = i \left[|F|^2 + 2|B|^2 \right] F, \tag{3.30}$$

$$-\frac{\partial B}{\partial z} + \frac{n_0}{c} \frac{\partial B}{\partial t} - \frac{i}{2k} \frac{\partial^2 B}{\partial x^2} = i \left[2|F|^2 + |B|^2 \right] B, \tag{3.31}$$

where the nonlinear constant n_2 has been scaled into the field amplitudes by the relation

$$F = \sqrt{2\epsilon_0 n_0 n_2 \omega} F', \tag{3.32}$$

where F' is the field amplitude with physical units. This also has the consequence of letting $I = |F|^2 = \kappa$ which allows comparison to the results of the previous section. It

should also be noted that weak-wave retardation is evident in these equations. The term

$$\left[|F|^2 + 2|B|^2\right] F$$

shows that the effect of B on F is twice as large as the effect of F on itself. A symmetric term exists in the equations for B.

3.4.2 Linear Stability Analysis

To determine the stability of the field amplitudes Eqs. (3.30), we consider perturbations about the steady-state plane-wave solutions $F_0(z)$ and $B_0(z)$ of the form

$$F(x,z,t) = F_0(z)\left[1 + \epsilon f_+(x,z)e^{\lambda t} + \epsilon f_-^*(x,z)e^{\lambda^* t}\right], \tag{3.33}$$

and a similar equation for $B(x,z,t)$. The form of these perturbations (*i.e.*, the inclusion of the conjugate terms) is necessary as the interaction, Eq. (3.27), mixes conjugate terms. The perturbations are assumed to obey

$$\frac{\partial^2}{\partial x^2} f_\pm \simeq -K^2 f_\pm, \quad \frac{\partial^2}{\partial x^2} b_\pm \simeq -K^2 b_\pm, \tag{3.34}$$

where K describes the transverse component of the perturbation. This form of the perturbations allows for a variety of four-wave-mixing couplings, including those treated by Grynberg and Paye [10, 48, 49, 51]. Substituting Eq. (3.33) into Eqs. (3.30) and linearizing about the steady state solutions gives a set of four coupled equations for the perturbation amplitudes $f_\pm$ and $b_\pm$. Instability will occur whenever these four equations have a nontrivial solution with $\mathrm{Re}\,\lambda > 0$. The boundary between stable states and unstable states is known as the instability threshold. Above threshold the system

is unstable and perturbations grow, while below threshold the system is stable and perturbations die out and the system returns to its steady state.

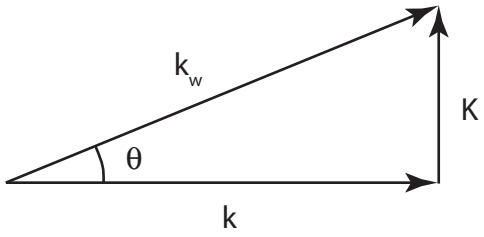

Figure 3.9: The off-axis wave with transverse wavevector K and total wavevector k_w propagates at an angle θ to the pump beam with wavevector k.

For this instability, the threshold curve is shown in Fig. 3.10. This plot can be understood to indicate the boundary between stable and unstable states of the system. The vertical axis represents increasing intensity or increasing length. The nonlinear refractive index n_2 has been scaled into the field amplitudes so in this model, IL has the same units as κL in the previous sections. The horizontal axis indicates the transverse component of the perturbing wavevector, and the quantity $K^2L/2k$ represents the phase difference between the off-axis waves and the pump waves. This can be seen by considering the pump-beam and off-axis wave with wavevectors illustrated in Fig. 3.9. The difference $\Delta k = k_w - k$ is given by

$$\Delta k = k_w - k = k\left(\frac{k_w - k}{k}\right) = k\left(\frac{1}{\cos\theta} - 1\right) \simeq k\frac{\theta^2}{2} = \frac{K^2}{2k}, \tag{3.35}$$

where I have made the small angle approximations, $\theta = K/k$, and $\cos\theta \simeq 1 - \theta^2/2$. Thus, from Fig. 3.10, we see that, as the intensity increases (imagine moving a horizontal bar up from the $IL = 0$ axis), the first point we reach on the curve indicates that the transverse wavevector with the lowest threshold for self-oscillation corresponds to

$K^2L/2k \simeq 3$, with $IL \simeq 0.45$. Other wavevectors have higher self-oscillation thresholds. The scalloped nature of the threshold curve results from plotting the minima of multiple solutions. In this case, six solutions are shown, each contributing one scallop. These multiple solutions indicate the periodic nature of the phase-matching condition for the underlying four-wave mixing processes. The threshold is lowest for off-axis waves, which are most nearly phase-matched, but there are other off-axis waves that are also nearly phase matched and thus lead to local minima in the instability threshold.

It is also important to note that the on-axis plane-wave ($K = 0$) threshold is infinite, in agreement with the results of Silberberg and Bar-Joseph for the case of an instantaneous nonlinear response. Also plotted in Fig. 3.10 is the threshold predicted by including only backward four-wave mixing, $IL = \pi/4$. Clearly, the transverse instability occurs at a lower overall threshold, but the threshold curve approaches $IL = \pi/4$ in the limit of large K. Hence, in the large-K limit (large θ) the contribution due to forward four-wave mixing is small due to poor phase-matching.

Finally, it is instructive to apply these results to a physical situation. As an example, consider a rubidium system. The prediction that self-oscillation occurs at $K^2L/2k \simeq 3$ implies that the angle between the waves with wavevector K and the pump waves is approximately $\theta \simeq K/k \simeq 3.9$ mrad for a 5 cm sample of rubidium vapor, λ =780 nm. Furthermore, this result can be compared to the estimate presented in Sec. 3.1 by writing θ in terms of λ and L. Using the small-angle approximation, we have

$$\theta \simeq \frac{K}{k} = \frac{1}{k}\sqrt{\frac{6k}{L}} = \sqrt{\frac{3\lambda}{\pi L}}, \tag{3.36}$$

which differs from the weak-wave retardation estimate, $\theta \simeq \sqrt{\frac{\lambda}{2L}}$, by a factor of

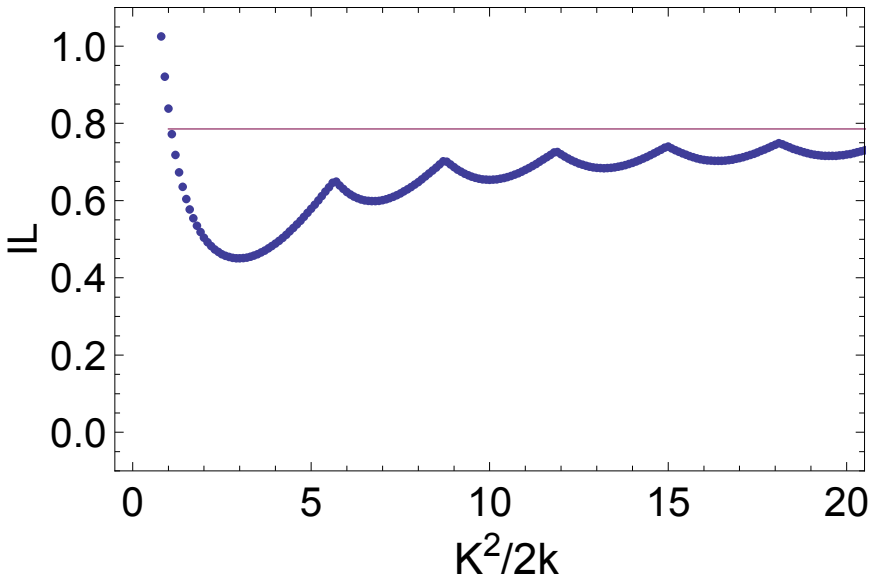

Figure 3.10: Threshold intensity for self-focusing media with phase grating, from [10]. The vertical axis is in units of IL, and the horizontal axis is in units of $K^2L/2k$ where K is the off-axis component of the perturbation wavevector.

$\sqrt{6/\pi} \simeq 1.4$. In the next chapter, I present a pattern forming system consisting of two pump waves that counterpropagate in rubidium vapor. Based on the analysis here, it should not be surprising that this system generates a cone of light that propagates at an angle to the pump waves of $\simeq 4$ mrad.

3.5 Hexagonal pattern formation

Simulations based on the model of Firth and Paré exhibit hexagonal pattern formation, which is in agreement with a number of experimental results [40, 52–55]. Grynberg, in [48], gives a qualitative explanation of the origin of these hexagons. First, recall that the gain of the weak fields in the parametric processes of FFWM and BFWM is associated with the depletion of the pump fields, with two photons being absorbed from the pump beam(s). There are, however, secondary four-wave mixing processes whereby only one pump photon is absorbed and the second input photon comes from

the generated off-axis beams. For example, in the forward direction, one pump photon can be absorbed along with one photon from the off-axis beam E_2, resulting in emission of two photons, one in beam E_4 and one in beam E_5 (see Fig. 3.11). The phase matching condition requires that the directions of E_1, E_4, and E_5 form an equilateral triangle. Likewise, a pump photon and a photon from E_1 can be absorbed, leading to gain in E_3 and E_6. One can think of this process in terms of *photon generations* where each photon from the first generation can contribute, along with a pump photon, to the creation of a second generation of photons.

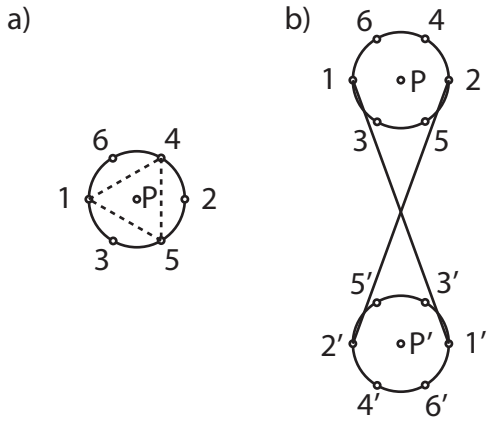

Figure 3.11: Hexagonal patterns in terms of secondary wave-mixing processes. a) The six weak waves that form a hexagon, contribute to processes that absorb one pump photon and one weak-wave photon and emit two weak-wave photons. b) These processes happen in both directions, generating hexagons in both outputs.

Considering these secondary processes, we count the processes that contribute gain to the weak fields, and those that require absorption from the weak fields. To this order, where one pump photon is absorbed and one off-axis photon is absorbed, there are two forward processes that create a photon for each spot on the hexagon, and only one forward process that requires absorption from that spot. The net result is that a process that breaks the symmetry of the system will cause the pattern to collapse from a Uring pattern to six spots in a hexagon. This symmetry-breaking can be intentional, via

misalignment of the pump beams, or unintentional, via aberrations in the windows of a vapor cell, or other optical imperfections. For the case of strongly-broken symmetry, *i.e.* if the pump beams are significantly misaligned, only two spots will be phase matched and the pattern is oriented perpendicular to the plane containing the pump beams.

3.6 Higher-order patterns

The previous section presents a conceptual argument for why counterpropagating plane-waves exhibit hexagonal symmetry in off-axis pattern formation. There are extensions to this argument that explain the generation of patterns with more than six spots. An analysis by Grynberg, Maître and Petrossian [56] of the single-mirror feedback system, flowerlike patterns are expected when the material exhibits a saturable nonlinearity. In contrast to a Kerr media, where the nonlinear effect is proportional to the intensity without bound, the strength of a saturable nonlinearity increases more slowly above a saturation intensity. Using Gaussian pump beams in a single-mirror feedback geometry propagating through warm rubidium vapor, Grynberg *et al.* show that patterns with 10 to 24 spots can be generated. Theoretical description of these patterns can be made by considering the conditions under which a Laguerre-Gauss mode with the same waist and phase curvature as the pump beam can oscillate between the nonlinear material and the feedback mirror. The resulting symmetry, *i.e.*, the number of spots, of the driven modes depends on the degree to which the nonlinearity is saturated. For an unsaturated nonlinear response, the pump beams do not couple strongly to higher-order modes and the generated patterns are expected to have few spots. For a saturated nonlinear response, the spatial extent of the nonlinear effect is broadened compared to the Gaussian pump intensity and thus higher-order modes can oscillate, generating more spots.

Although the single-mirror feedback system is distinctly different from the case of two counterpropagating beams, the similarities in observed patterns suggest a similar argument holds for the counterpropagating system as well. As I will show in the next Chapter, my experimental observations are also consistent with this discussion. For pump beam intensities just above threshold, I observe two- and six-spot patterns, and for pump beam intensities well-above threshold, where the nonlinearity is likely to be saturated, I observe similar flowerlike patterns.

3.7 Polarization instabilities

The prior discussion of pattern forming instabilities has been based on a scalar model of the nonlinear optical response. In a scalar model, the polarization degree of freedom is explicitly ignored. Polarization instabilities, however, are readily observed in a wide range of counterpropagating-beam systems [37, 42, 57, 58]. To discuss the origins of polarization instabilities, I first describe a vector model of the nonlinear optical response. For an isotropic nonlinear material, such as atomic vapor, one can often describe the nonlinear polarization in terms of an effective linear susceptibility

$$P_i = \epsilon_0 \sum_j \chi_{ij}^{\text{eff}} E_j, \tag{3.37}$$

where the indices $i, j = x, y, z$ correspond to the three cartesian coordinates and [13]

$$\chi_{ij}^{\text{eff}} = \left(A - \frac{B}{2}\right)(\mathbf{E}\cdot\mathbf{E}^*)\,\delta_{ij} + \frac{B}{2}\left(E_i E_j^* + E_i^* E_j\right). \tag{3.38}$$

The second term in Eq. (3.38) allows a field polarized in one direction to drive a material polarization that will radiate with a different state of polarization. As an

example, one of the terms contained in Eq. (3.38) gives rise to a nonlinear polarization of the form

$$P_x = \epsilon_0 \frac{B}{2} \left(E_x E_y^* + E_x^* E_y \right) E_y, \tag{3.39}$$

which describes the coupling between two orthogonally polarized fields E_x and E_y via polarization P_x. Clearly, this model requires $B \neq 0$ in order for the two polarization states to couple, *i.e.*, if $B = 0$ no polarization instability is expected.

The relative magnitudes of the A and B coefficients in this model depend on the nature of the physical processes responsible for the optical nonlinearity [13]. For optical nonlinearity arising from resonant atomic response, the A and B coefficients are determined by the different angular momenta of the atomic states involved [59].

Gaeta and Boyd [42] perform a linear stability analysis of counterpropagating beams that extends the analysis of Firth and Paré by including the vector nature of the field, *i.e.*, allowing polarization degrees of freedom. This analysis is based on the effective-χ model presented above [Eq. (3.38)] and shows that the nature of the instability with the lowest threshold depends both on the ratio B/A and on the polarization states of the counterpropagating pump beams. My experiment utilizes linearly co-polarized pump beams, a configuration that Gaeta and Boyd show is unstable to off-axis amplitude fluctuations, as in the Firth and Paré treatment. However, as long as B/A is positive, this configuration does exhibit a polarization instability at input intensities that are higher than the intensity needed for amplitude instabilities.

The polarization instabilities studied in [42] are predicted by the treatment based on Eq. (3.38). However, Pinard *et al.* [60] have shown that this treatment is not complete for the case of two counterpropagating beams in Doppler-broadened medium. They find that, instead of two constants, A and B, five constants are required in general to describe the nonlinearity, but still in the third-order ($\chi^{(3)}$) approximation. For

the case of an optical pumping nonlinearity, only four of these are independent and they correspond to the magnetization and electric-quadrupole moment of the medium induced by the forward and backward beams. Naturally, these parameters depend on the angular momentum states coupled by the counterpropagating beams, and thus depend on the specific transitions excited by the pump fields.

To determine how well these treatments agree with my experimental results, I consider the following details. As I will discuss in Sec. 4.2.1, I observe pattern formation on the high-frequency side of the $^5S_{1/2}(F = 1) \rightarrow {}^5P_{3/2}(F' = 1)$ hyperfine transition in rubidium. Based on the treatment given in Ref. [59], these angular momentum states lead to $B = 0$ and hence Eq. 3.38 predicts that there is no polarization instability due to the $(F = 1) \rightarrow (F' = 1)$ transition. The treatment by Pinard *et al.* [60] makes a similar prediction: the $(F = 1) \rightarrow (F' = 1)$ transition does not give rise to polarization instability. Clearly, these treatments alone are not adequate for explaining my observation of a polarization instability near Rb $^5S_{1/2}(F = 1) \rightarrow {}^5P_{3/2}(F' = 1)$.

My observation of off-axis pattern formation for pump beams tuned above the $(F = 1) \rightarrow (F' = 1)$ transition is, however, consistent with the treatment given by Pinard *et al.* [60]. The angular momenta of these states are appropriate for observing self-focusing on the high-frequency side of the resonance. Self-focusing, or positive n_2, is assumed in the model of Firth and Paré and is crucial for off-axis pattern formation as it is required for the forward four-wave mixing process to be phase-matched (see Sec. 3.1).

The poor agreement between these treatments and my observation of polarization instability suggests that either Eq. (3.38) is not adequate to describe the nonlinearity in my system, or the results of Saikan [59] are not accurate for my case. Pinard *et al.* suggest the former is true and generalize Eq. (3.38) to treat the case of counterpropagating beams in a Doppler-broadened medium. However, their treatment also fails to

account for my observation of a polarization instability. Some features of my experiment, such as which side of resonance exhibits self-focusing are correctly described, but further theoretical treatment is necessary to describe the origins of the polarization instability I observe. The perturbative (third-order) approach of Pinard *et al.* assumes that the two-level transition is unsaturated and that the ground state is closed. I operate well above the two-level saturation intensity and, in rubidium, the ($F' = 1$) excited state can decay to the ($F = 2$) ground state which is detuned from the pump beams by over 6 GHz (*i.e.*, the transition is open). Thus, a theoretical treatment based on F-state pumping or on a non-perturbative approach may yield more accurate results.

3.8 Summary

In this Chapter, I have described the forward and backward four-wave mixing processes (FFWM and BFWM), and presented three theoretical treatments that consider the roles these processes play in instabilities that spontaneously generate off-axis light. The treatment of Yariv and Pepper considers only backward four-wave mixing and describes an instability that is automatically phase-matched to occur in any direction [44]. Grynberg and Paye refine this treatment by considering the combination of forward and backward four-wave mixing processes and show that the two processes only add coherently at a finite angle θ leading to conical emission of instability generated light. In another treatment considering both FFWM and BFWM, Firth and Paré include a continuous transverse dimension allowing for arbitrary transverse wavevector components. This analysis also predicts that instability-generated light will be emitted at a finite angle θ on the order of a few mrad. Furthermore, the treatments of Grynberg and Paye, and Firth and Paré predict instability thresholds that are roughly half that predicted by Yariv and Pepper [10, 49].

Additionally, I have given a qualitative argument, originally presented by Grynberg, that suggests conical emission is replaced by hexagonal pattern formation when weak symmetry-breaking is present in the system [48]. I have also argued that higher order patterns can be observed and are expected for systems exhibiting saturable nonlinearities. Finally, I have described polarization instabilities, and several treatments that predict polarization instabilities for various experimental conditions. These treatments do not account for all of my experimental observations, however, they serve to introduce the relevant concepts and suggest directions for future theoretical work. The next Chapter presents my experimental observations of counterpropagating beam instabilities, including pattern formation, in a system where warm rubidium vapor serves as the nonlinear medium.

Chapter 4

Pattern Formation in Rubidium Vapor

In the previous chapter, I presented a theoretical framework for describing a system consisting of two pump beams that counterpropagate through a nonlinear medium. The primary conclusion of Chapter 3 is that a pair of beams counterpropagating through a nonlinear optical medium give rise to patterns formed by light that is spontaneously emitted at an angle to the pump-beam axis. This chapter presents my experimental results of pattern formation in a counterpropagating beam system where a sample of warm rubidium vapor serves as the nonlinear medium. I first describe my experimental setup, then describe the light and patterns generated by the system for various experimental parameters. It should be noted that preliminary results for this work were acquired using a slightly different experimental setup. Appendix A contains a discussion of the differences between the original system and the current system, and a review of the problems overcome by various modifications to the system.

4.1 Experimental apparatus

A diagram of my experimental setup is shown in Fig. 4.1. Two beams of light from a common laser source counterpropagate through warm rubidium vapor contained in a glass cell. The light source is a frequency-stabilized continuous-wave Ti:Sapphire laser, the output of which is spatially filtered using a single-mode optical fiber with an angled entrance face and a flat-polished exit face. The beam is then collimated using a pair of convex lenses arranged as a telescope. The spot size (1/e field radius), denoted

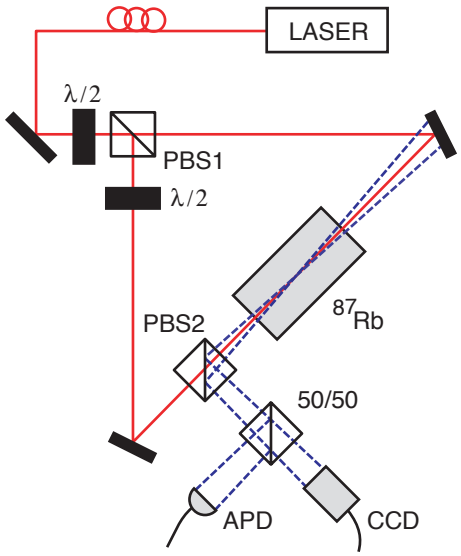

Figure 4.1: Experimental setup for transverse optical pattern generation. The output of a frequency-stabilized cw Ti:Sapphire laser serves as the source. A polarizing beamsplitter (PBS1) separates the forward (cw) and backward (ccw) beams within the triangular ring cavity. The backward beam is brought into horizontal polarization by a half-wave plate ($\lambda/2$). The forward and backward beams counterpropagate through a warm ^{87}Rb vapor contained in a 5-cm glass cell. A polarizing beam-splitter (PBS2) reflects instability-generated light in the vertical polarization which is observed by a CCD camera and avalanche photodiode (APD).

w_0 is controlled by the configuration of the telescope, and the beam waist is located in the center of the vapor cell. The power ratio between the pump beams is controlled by a half-wave plate at the input of the first polarizing beam splitter (PBS1). I denote the beam passing through PBS1 as the forward beam and the reflected beam as the backward beam. A second half-wave plate in the backward beam path rotates the polarization such that the pump beams are linearly polarized with parallel polarizations.

The cell is 5 cm long, 2 cm in diameter, and contains a droplet of rubidium, melting point 39.3 °C, which is in equilibrium with rubidium vapor. The rubidium contained in the cell has not been isotopically enriched and thus contains the two naturally abundant isotopes: $\sim$ 72% ^{85}Rb, 28% ^{87}Rb. Figure 4.2 shows the dependence of the ^{87}Rb number density on the cell temperature. The cell is heated to 80 °C corresponding to an atomic number density for ^{87}Rb of 2×10^{11} atoms/cm^3. The cell has uncoated quartz windows that have fixed and opposing tilt angles of $\pm$11 degrees with respect to the incident laser beams to prevent possible oscillation between the windows. The cell has no paraffin coating on the interior walls that would prevent depolarization of the ground-state coherence, nor does it contain a buffer gas that would slow diffusion of atoms out of the pump laser beams. The Doppler-broadened linewidth of the transition at this temperature is $\sim$550 MHz. To prevent the occurrence of magnetically-induced instabilities and reduce Faraday rotation, a cylindrical μ-metal shield surrounds the cell and attenuates the ambient magnetic fields by a factor of $> 10^3$. In order to attenuate the static magnetic field created by the heater coils, the shield is located within the resistive heaters used to heat the cell.

A polarizing beam splitter (PBS2) placed in the beam path separates light polarized orthogonally to the pump beam (see Fig. 4.3). This light, henceforth referred to as *output* light, is subsequently split with a 50/50 beamsplitter and then observed simultaneously using any two of the following: a CCD-camera (Marshall V-1050A), an

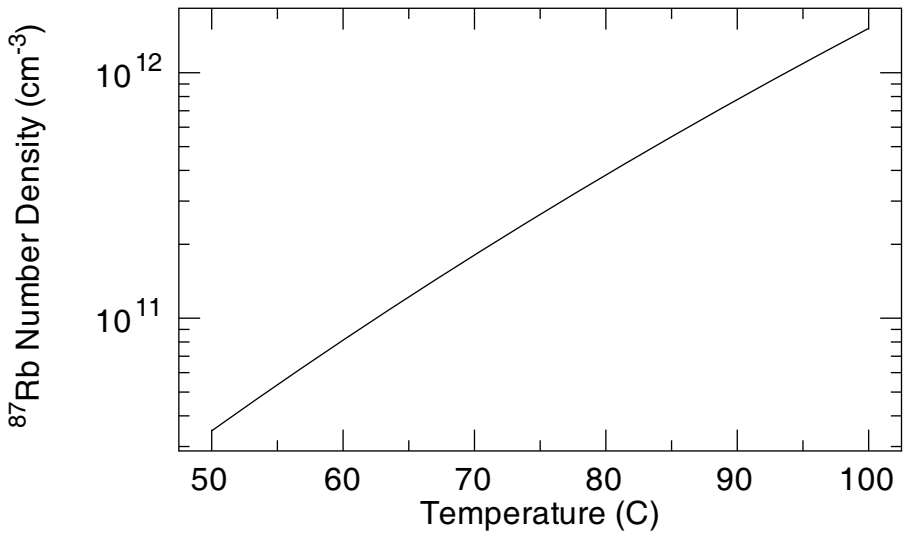

Figure 4.2: ^{87}Rb number density as a function of temperature, taken from the model given in [61].

avalanche photodiode (Hamamatsu C5460), or a photomultiplier tube (Hamamatsu H6780-20) as shown in Fig. 4.1.

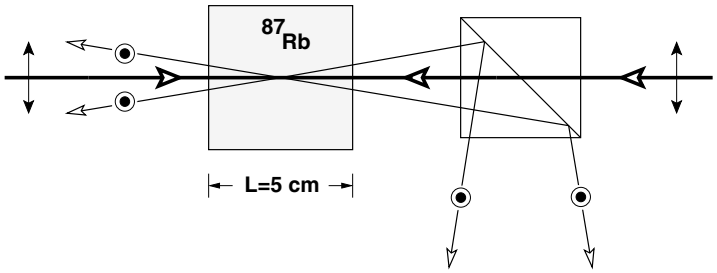

Figure 4.3: The pump beams are co-polarized in the horizontal plane, indicated by arrows, while the generated light is vertically polarized, indicated by circled dots. A polarizing beamsplitter separates the forward generated light from the transmitted forward pump beam. Polarization provides a straightforward way to isolate the generated light from transmitted pump light.

4.2 Instability generated light

In the experimental setup described above, I observe instability generated light (output light) in the state of polarization orthogonal to that of the pump beams and with the same frequency as the pump beams. The following sections describe features of the instability as well as the conditions required for observing pattern formation. The experimental variables are the frequency of the pump light, the alignment and intensity of the pump beams, and the pump beam waist w_0. The vapor pressure is held constant by maintaining the cell temperature at 80° C, which I have found is optimum for all other parameters I have explored. The path length through the vapor is fixed by the cell length $L = 5$ cm.

The fixed cell length has been chosen to balance large optical depth, which increases with increasing L, and available transverse modes, which decrease with increasing L. The Fresnel number,

$$\mathscr{F} = \frac{w_0^2}{\lambda L}, \tag{4.1}$$

quantifies the number of transverse modes supported by the geometry where w_0 is the pump-beam waist (1/e field radius), L is the longitudinal dimension, and λ is the wavelength [14]. I have observed light generated off-axis for Fresnel numbers between 1.9 and 7.8, corresponding to w_0 between 270 μm and 550 μm. Except where otherwise noted, the results presented below correspond to $w_0 = 455$ μm with $\lambda = 780$ nm, or $\mathscr{F} = w_0^2/(\lambda L) = 5.3$.

The other fixed parameter, the temperature, has been chosen based on optimizing the pattern-formation. Changing the temperature of the cell effects both the temperature of the atomic vapor and the atomic number density. For this work, changing the atomic number density primarily effects the optical depth of the vapor. As described

in Chapter 2, Eq. (2.27), the optical depth determines the amount of absorption experienced by a beam propagating through a an absorbing medium. By varying the cell temperature, and observing the amount of optical power generated by the instability, I find that the optimum temperature is 80° C. Fitting the absorption profile at $T = 80°$ C to a model for Rubidium absorption, I find that the maximum Doppler-broadened optical depth at this temperature is $\alpha L = 55$.

Both the cell temperature and the cell length are fixed at these optimum values for all data presented in this thesis. Appendix A describes results obtained under different conditions, and the following two sections describe the properties of the generated light for various pump-beam frequencies and intensities.

It is important to note that this optimal value $\alpha L = 55$ is much larger than the optimum value for an all-optical switch based on saturable absorption, $\alpha L = 1.3$ as described in Sec. 2.2. The switch I present in the next Chapter is not an absorption-based switch and in order to observe patterns suitable for use in all-optical switching, I use an optically thick medium, $\alpha L >> 1$, with pump beam intensity that is significantly higher than the saturation intensity. For these conditions, absorption in a sample of two-level atoms is known to improve the nonlinear wave-mixing, especially for the case where the forward pump-beam intensity is larger than the backward pump-beam intensity [62].

4.2.1 Pump-beam frequency

I find that the power of the output light is maximized (and the threshold for the instability is lowest) when the frequency of the pump beams is set near an atomic resonance, *i.e.*, the instability occurs near either the D_1 or D_2 transition of ^{87}Rb. For this thesis, I describe results for pump-beam frequencies near the D_2 transition ($^5S_{1/2} \rightarrow {}^5P_{3/2}$,

780 nm wavelength) shown in Fig. 4.4.

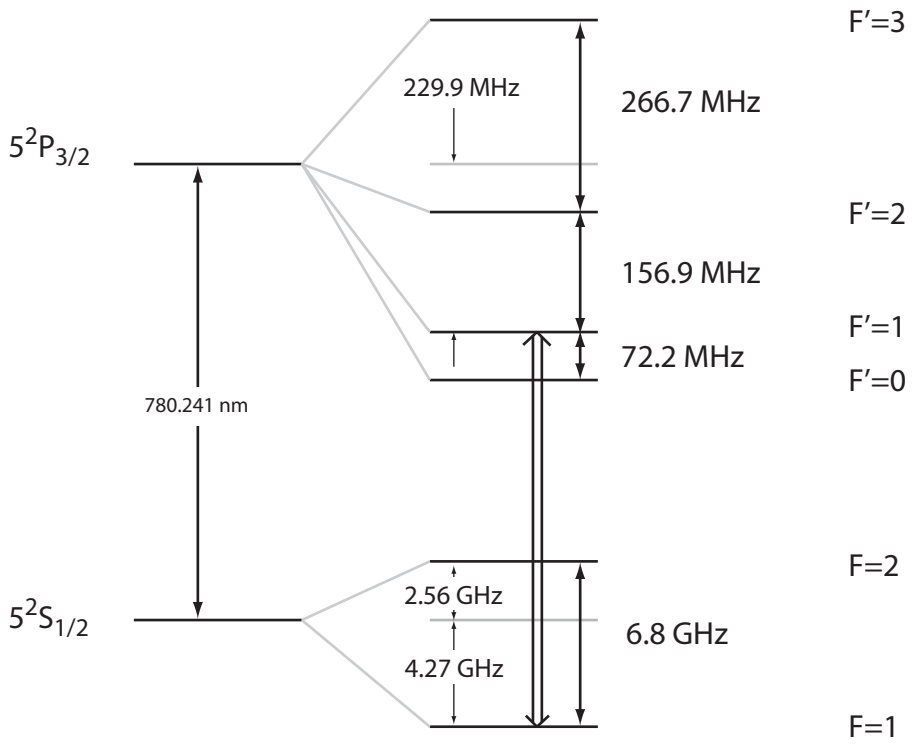

Figure 4.4: Energy level diagram for the D_2 line of ^{87}Rb showing the hyperfine levels and frequency difference in Hz ($\Delta E = \hbar\omega = h\nu$). The double arrow indicates the $F = 1 \rightarrow F' = 1$ transition where my experiments are conducted.

Figure 4.5 shows the power of the output light as a function of pump frequency detuning, defined as $\Delta = \nu - \nu_{F=1,F'=1}$ in cycles/s. I observe several sub-Doppler features, where the maximum power emitted in the orthogonal polarization occurs when the laser frequency ν is tuned $\Delta = +25$ MHz. For this detuning, 3.5 μW of output light is generated in the forward direction, indicating that $\sim 1\%$ of the incident

pump power is being converted to the orthogonal polarization. Because the detuning is small relative to the Doppler width, a significant amount of the pump light is absorbed by the medium. Of the 50 μW of light transmitted in the forward direction, $\sim$ 7% is being converted to the orthogonal polarization. In the next section, I discuss how the presence of absorption affects the instability.

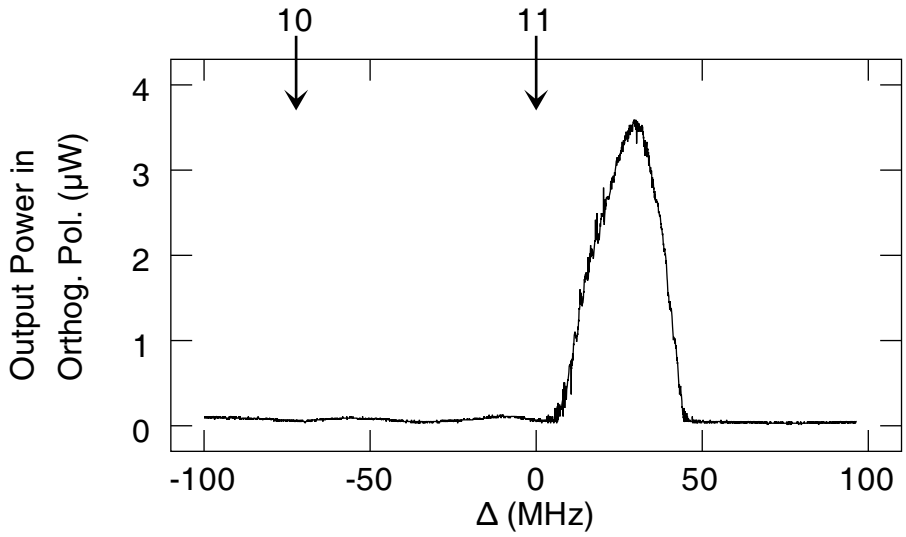

Figure 4.5: Instability-generated optical power as a function of pump laser frequency detuning ($\Delta = \nu - \nu_{F=1,F'=1}$). The plot shows the power generated in the forward direction and in the state of polarization orthogonal to that of the pump beams. These data correspond to a single scan through the $^5S_{1/2}(F = 1) \rightarrow {}^5P_{3/2}(F')$ transition in ^{87}Rb from low to high frequency. The bold tick marks at the top of the frame indicate the hyperfine transitions labeled by FF', where F (F') is the ground (excited) state quantum number. Pump beam power levels for this data are 415 μW forward and 145 μW backward, and $w_0 = 455\,\mu$m. The Doppler-broadened linewidth of the transition at this temperature is $\sim$ 550 MHz, hence the generated light is only emitted for pump frequencies in a narrow range within the Doppler profile.

The instability clearly occurs on the blue-detuned (high-frequency) side of the $^5S_{1/2}(F = 1) \rightarrow {}^5P_{3/2}(F' = 1)$ transition. This is the side of the resonance where the nonlinear refractive index has a positive value and hence self-focusing is expected to occur. This experimental observation agrees with theoretical models including the simple argument I presented in Chapter 3 based on weak-wave retardation. The for-

ward four-wave-mixing process can only become phase matched for off-axis beams if the nonlinear refractive index n_2 has a positive value, *i.e.*, on the high-frequency side of an atomic resonance [13]. If n_2 is negative, the off-axis wavevectors are shortened, and thus cannot be phase-matched to the pump-beams regardless of the angle θ (see Fig. 3.2) [13, 48]. It should also be noted that the analysis of Firth and Paré assumed a positive value for n_2 and thus my observations of off-axis pattern formation for pump beams detuned above a resonant frequency is consistent with their result.

The width of the feature shown in Fig. 4.5 changes with pump power such that it is narrower near threshold. This change indicates that phase matching depends on the pump power such that for large pump power, a wider range of frequencies are phase-matched. The amount of power generated in the orthogonal polarization is also lower near threshold and increases linearly with increasing pump power as described in the following section.

4.2.2 Pump-beam intensity

The instability observed in this system has a very low threshold; the power required to induce self-oscillation is less than 1 mW, which is comparable results from coherently-prepared atomic media as I discuss later in this section. A common way to measure the instability threshold for a setup with counterpropagating beams is to fix the power of one of the beams and measure the output power as a function of the power in the second pump beam [22, 37]. For a pump-beam detuning of $\Delta = +25$ MHz and with a fixed forward pump power of 415 μW, I find that the backward pump power threshold is $\sim$75 μW, corresponding to a total pump power of 490 μW.

Another way to measure the instability threshold is to determine the minimum total pump power necessary to generate output light. Figure 4.6 shows the result of such

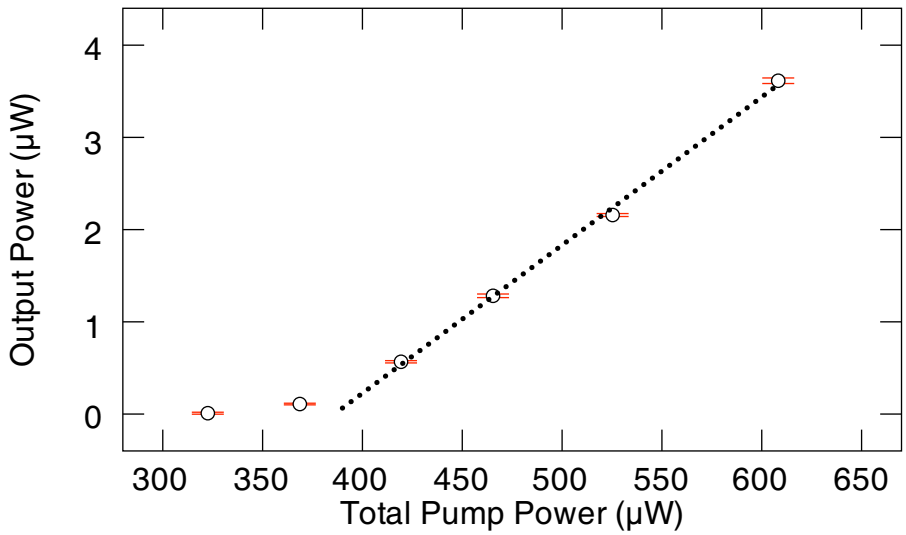

Figure 4.6: Instability thresholds. Generated optical power as a function of total pump beam power. The instability occurs with a threshold of 385 μW. Data shown corresponds to a fixed pump beam power ratio of 3-to-1 (forward to backward).

a measurement for my experiment. I find that there is an optimum ratio of forward power to backward power of ~3-to-1. At this ratio, I determine the threshold for off-axis emission to be 385 μW which is slightly lower than the threshold measured with fixed forward beam power. I typically observe patterns and switching with ~560 μW of total power, corresponding to 40% above threshold.

Both threshold measures demonstrate that the nonlinear process that generates new light is induced by a pair of very weak fields indicating very strong nonlinear matter-light interaction comparable with the best reported results to date for warm-vapor counterpropagating beam systems [22].

For most of the early observations of nearly-degenerate instabilities, strong pump fields were used (typically hundreds of mW) [39, 40, 45]. A considerably higher threshold was reported for the first observation of polarization instabilities in a sodium vapor [37], where a threshold of tens of mW was found when the pump fields were

tuned near an atomic resonance. More recently, Zibrov *et al.* [22] observed parametric self-oscillation with pump powers in the μW regime using a more involved experimental setup ("double-Λ" configuration) designed specifically to lower the instability threshold. In their experiment, atomic coherence effects increase the nonlinear coupling efficiency. They report oscillation with several mW of total pump power. With 5 mW of forward-beam power, their instability threshold corresponds to 20 μW in the backward beam. In contrast, the results reported in this thesis demonstrate that spontaneous parametric oscillations are induced by μW-power counterpropagating pump-beams without the need for special coherent preparation of the medium. Furthermore, Zibrov *et al.* observe only on-axis emission, whereas, I find that off-axis emission requires roughly half as much pump power as on-axis emission with my pump beam configuration. In situations where low power and high sensitivity are important, such as in all-optical switching, the lower instability threshold may make off-axis instabilities preferable.

4.2.3 Forward four-wave mixing gain

To compare my experimental observations of this instability to the predictions based on the Kerr model discussed in Chapter 3, I perform a measurement of the gain experienced by a weak probe beam propagating through the medium in the forward direction at an angle $\theta = 4 \pm 0.2$ mrad (see Fig. 4.7). When the pump beam intensity is below the threshold for self-oscillation, forward four-wave mixing is expected to give rise to gain experienced by this probe beam. If, on the other hand, the pump beam intensity is above threshold, self-oscillation occurs and light is spontaneously emitted in the forward direction.

Using a 6 nW probe beam, and 323 μW total pump beam power in a 3-to-1 forward

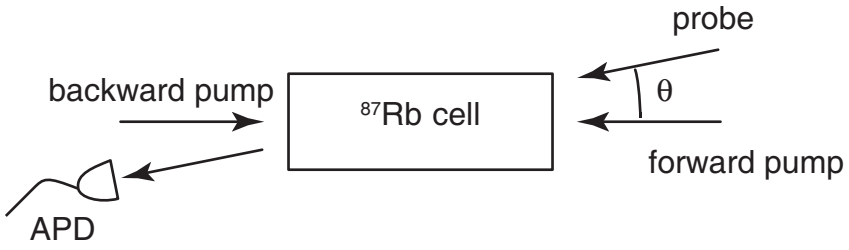

Figure 4.7: Experimental setup for measuring the forward four-wave mixing gain below threshold. A weak probe beam propagates through the rubidium vapor in the forward direction and at an angle $\theta = 4 \pm 0.2$ mrad to the pump-beam axis.

to backward pump power ratio, I measure a gain of $P_o/P_i = 6.2 \pm 0.6$ where P_o is the output power in the probe beam and P_i is the input probe-beam power. To compare this measured value to predictions based on the Kerr model, I solve numerically the model of Firth and Paré given in Sec. 3.4.1.[1] Firth and Paré predict that off-axis self-oscillation occurs for $\kappa L \geq 0.45$ radians. By simulating the propagation of a weak off-axis beam ($\theta = 4 \pm 0.2$ mrad) identical to the setup shown in Fig. 4.7, I determine that the Kerr model predicts forward gain of $P_o/P_i = 1.45$ just below threshold ($\kappa L = 0.44$). The discrepancy between my measured value and the prediction based on a Kerr model suggests that absorption, which is not included in the Kerr model, serves to raise the threshold for self-oscillation in the experimental system. Specifically, the nonlinear phase shift at threshold in my experiment is somewhat larger than that predicted by the Kerr model. Using the model of forward four-wave mixing described in Sec. 3.3, *i.e.*, approximating the forward gain as a hyperbolic cosine function of κL, I estimate that the nonlinear phase shift at threshold is approximately equal to $\kappa L = \pi/2.8 = 1.1$. The additional gain I measure experimentally is thus required to overcome absorption loss before oscillation can occur.

Remarkably, the discrepancy between the Kerr model and my experimental result

[1]The implementation of this numerical model is discussed in more detail in Chapter 6.

is not large. The system parameters for this measurement, with the exception of using lower pump beam power, are identical to the conditions under which I observe self-oscillation. Namely, the pump beams are tuned very near an atomic resonance $\Delta = +25$ MHz. Typically, in this regime, the Kerr model is not quantitatively accurate, yet there is order-of-magnitude agreement between the Kerr model and my experiment. The relative accuracy of the Kerr model in describing my experiment is likely due to the fact that the pump beams are well above the saturation intensity for the atomic medium, and hence the medium is much more transparent than it would be if it were unsaturated. Hence, despite the absence of absorption in the Kerr model, it corresponds reasonably well to the experimental conditions under which I observe mirrorless self-oscillation.

4.2.4 Patterns

In the context of all-optical switching, pattern formation is the most notable feature of the counterpropagating beam instability that I observe. When the pump beams are above threshold, *i.e.* have total power greater than 420 μW, generated light is emitted at an angle $\theta \simeq 4$ mrad to the pump beam axis as shown in Fig. 4.8(a). The angle θ observed in my experiments is slightly larger than the angle predicted by the models described in Chapter 3. This is consistent with the interpretation presented above that my experimental system exhibits a larger nonlinear phase shift in order to overcome absorption: the larger nonlinearity leads to longer weak-beam off-axis wavevectors which are thus phase-matched at a larger angle. A perfectly symmetric system is expected to generate light with intensity that is distributed evenly around the azimuthal angle, and hence would form a ring pattern in the far field. Perfect symmetry, however, is unattainable in the laboratory where imperfections in optical elements impart

small perturbations on the phase and amplitude of the beams. The instability responds to such perturbations by generating patterns that are not cylindrically symmetric. For this reason, the most common patterns I observe consist of two, four, or six spots in a variety of arrangements. In all cases, the spots are located along the ring projected by the cones onto the detection plane as illustrated in Fig. 4.8(b-d).

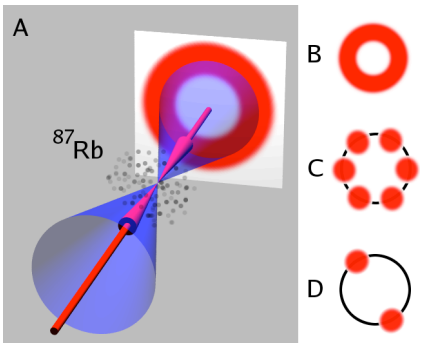

Figure 4.8: When pump beams (red) of a sufficient intensity counterpropagate through warm rubidium vapor, light is generated along cones (blue) centered on the pump-beam axis. A far-field detection plane shows patterns formed by the generated light. b) A ring pattern is expected for a perfectly symmetric system. c) Six spots form a hexagon, the typical pattern for pump beam powers more than 20% above threshold. d) Two spots are observed just above threshold or when the pump beams are mis-aligned.

The theoretical treatments presented in Chapter 3, and the discussion above, have all considered only the case where the pump beams are strictly counterpropagating. In theoretical work, this corresponds to the pump beams having equal and opposite wavevectors, and in experimental work this implies that the pump beams propagate in opposite directions and overlap one another for all space. In experiments, it is common to have slight mis-alignment between the pump beams. This misalignment can be either intentional or accidental.

When the pump beams are misaligned in my experiment, the generated patterns change. This change is due to change in the phase-matching conditions for the different azimuthal angles. Hence, there are different amounts of gain for different off-axis

beams, and for those beams that experience gain that is sufficient for self-oscillation, a spot will be generated in the pattern.

I observe experimentally that the cone of light that describes the pattern generated in the forward direction remains centered on the forward-beam pump axis. The backward beam alignment, therefore, primarily effects the intensity of the generated light (by changing the coupling between waves) and the orientation of the pattern (by changing the wave matching conditions). The opposite is true if I observe the pattern generated in the backward direction: the cone is centered on the backward pump beam and the forward pump beam primarily effects the intensity of the generated light. Therefore, in the case of misaligned pump beams, the axis of the cone of light generated in one direction is set by the axis of the pump beam which travels in that direction.

A selection of observed patterns are shown in Fig. 4.9 for various pump beam intensities and sizes (w_0). The patterns shown are for well-aligned pump beams tuned to $\Delta = +25$ MHz, the peak of the generated output shown in Fig. 4.5. They exhibit the general trend that increasing the pump beam intensity leads to a larger number of generated spots on the ring corresponding to $\theta \simeq 4$ mrad. As the pump beam size increases, the Fresnel number, Eq. (4.1), also increases, and thus more transverse modes are supported by the system. Consequently, for a given intensity, larger pump beams induce patterns with finer structure than do smaller pump beams. This is most clearly illustrated by the image in the upper right, showing 18 spots whereas the upper left image (which was taken at higher intensity) shows only 8, and two are clearly brigher than the others. There are generally two spots that dominate the others, this is due to the fundamental symmetry breaking in the system. As Grynberg suggests, these spots correspond to the directions with the largest four-wave mixing gain, and the other spots are generated in turn by secondary wave-mixing processes [48].

The pattern surrounded by a grey border exhibits the hexagonal symmetry that was explained in Chapter 3, and rather than a single pair of spots being dominant, two pairs (a total of four spots) exhibit roughly equal intensity. This pattern corresponds to the pump beam size and intensity used in the switching experiments, and as I will explain in more detail in the next Chapter, patterns with four equal-intensity spots exhibit the highest sensitivity to external perturbations, hence they are the most effective for all-optical switching.

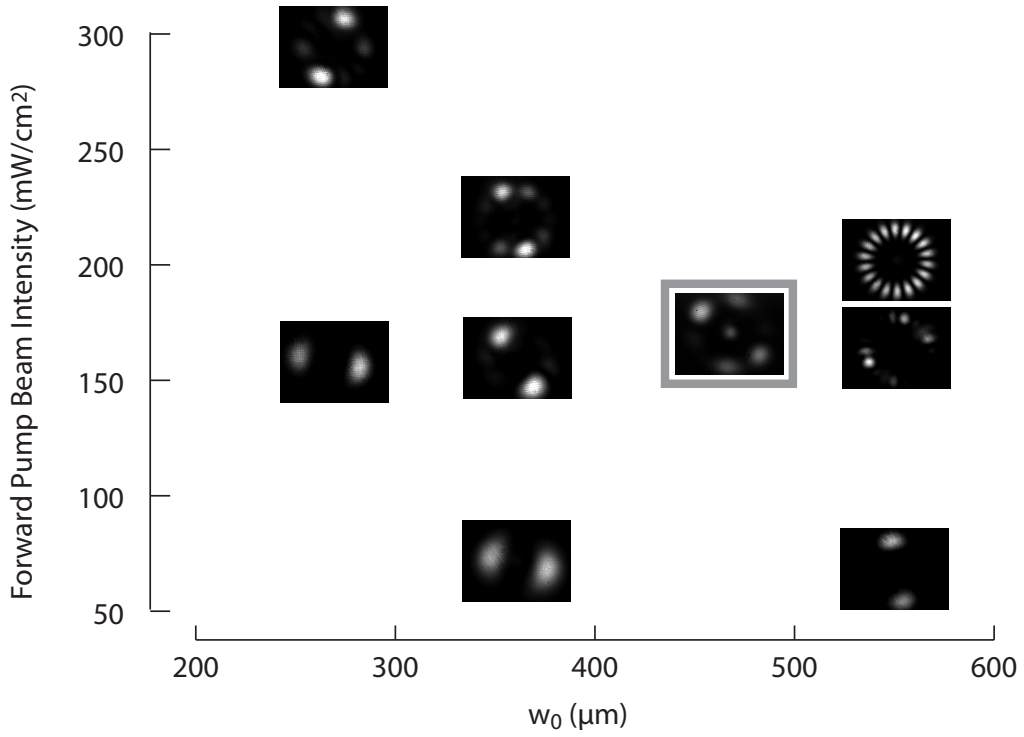

Figure 4.9: A map of the patterns observed for a range of pump-beam intensities and sizes where w_0 is the $1/e$ field radius of the pump-beams. The pattern corresponding to the parameters used in my experiments on optical switching is indicated with a grey border.

4.2.5 Secondary instability

In addition to the instability responsible for mirroless parametric self-oscillation, the system exhibits a secondary modulational instability (MI) that is manifested as oscillations in the intensity of the generated light. The frequency of the intensity oscillations due to this instability depends on the alignment of the pump beams. For well-aligned beams, counterpropagating along a common axis, the MI is generally suppressed as long as the pump-beam intensity is not significantly far above threshold.[2] Figure 4.10 illustrates the onset of this secondary instability. The threshold behavior illustrated in Fig. 4.6 is evident here as well: the power generated in the orthogonal polarization increases linearly above 385 μW total pump power. Also visible is the saturation of the pattern-forming instability near 800 μW, where increasing the total pump power no longer increases the generated power. The height of the vertical bars indicates the peak-to-peak amplitude of oscillations due to the secondary MI. There is a notable increase in the amplitude of the MI oscillations above 560 μW total pump power (indicated in the figure), and a significant increase above 800 μW total pump power.

When the pump beams are made to counterpropagate at a small angle, observing the photodetector signal with a spectrum analyzer reveals a harmonic series with a fundamental frequency that increases for larger angular separation of the pump beam axes. The spectrum is shown in Fig. 4.11 for pump beams misaligned by an angle $\theta_p \sim 0.4$ mrad, which is the pump beam alignment that exhibits sensitive switching as discussed in the next Chapter. In this case, the fundamental frequency is ∼245 kHz, and the first harmonic is visible at ∼490 kHz.

[2] As shown above, I typically observe patterns and switching with 560 μW of total power corresponding to an intensity that is roughly 40% above threshold.

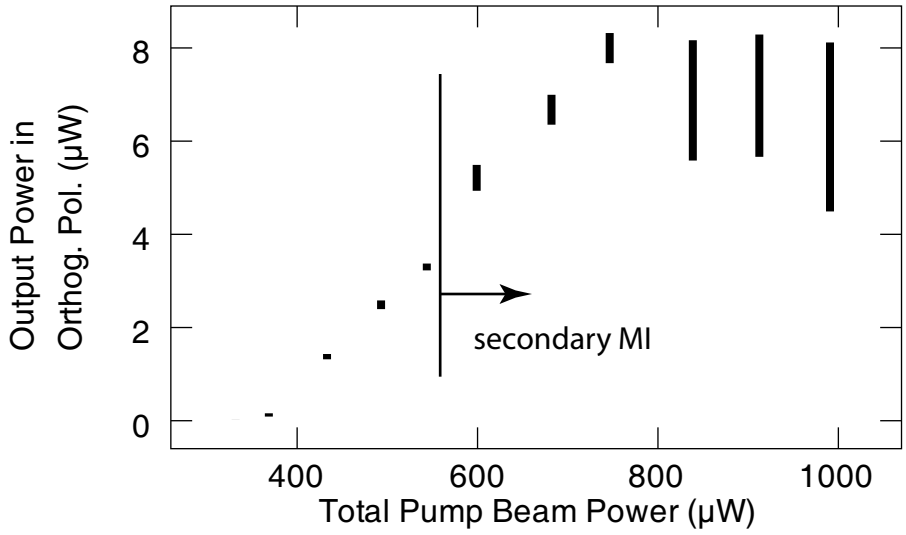

Figure 4.10: The peak-to-peak oscillations generated by the secondary modulational instability are indicated by the vertical bars. The output light generated in the orthogonal polarization is plotted as a function of total pump-beam power. Data are collected with fixed forward-to-backward pump-beam power ratio of 3:1, and detuning $\Delta = +25$ MHz.

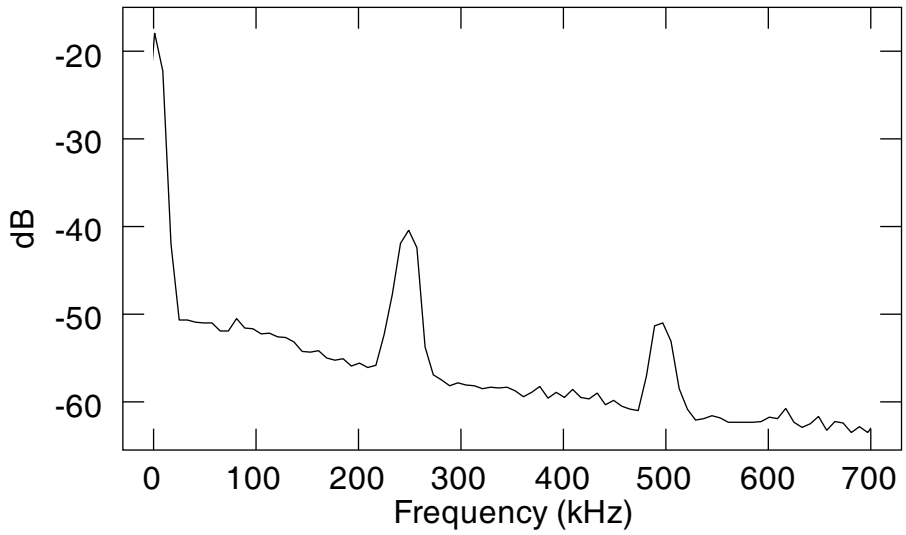

Figure 4.11: With pump-beam misalignment of $\simeq$0.4 mrad, the RF spectrum of the generated light shows a fundamental frequency of 245 kHz and the first harmonic at 490 kHz.

4.3 Summary

In this chapter I have presented a simple experimental system that gives rise to transverse optical patterns with less than 1 mW of optical pump power. An instability in the system gives rise to mirrorless parametric self-oscillation which is responsible for generating new beams of light that propagate at an angle to the pump beams and form multi-spot patterns in the far-field. I have characterized this instability, and the generated patterns, in terms of several properties of the pump beams: frequency, intensity, size, and alignment. A forward pump beam with 415 μW of power and a backward pump beam with 145 μW of power, both detuned to the high-frequency side of the ^{8}7Rb $F = 1 \rightarrow F' = 1$ D_2 resonance, generate $\sim$3 μW of optical power.

This instability is also responsible for the formation of optical patterns. The form of these patterns is two or more spots arranged along a ring corresponding to the projection of a cone of light onto the plane of measurement. The opening angle for the cone is $\sim$ 4 mrad. Patterns with hexagonal symmetry are observed in addition to patterns with up to 18 spots. Increasing the pump beam intensity or the pump beam size leads to patterns with finer transverse scales, and in general, to patterns with a larger number of spots. Just above threshold, for all pump beam sizes studied, the pattern consists of a pair of spots symmetrically located across the pump-beam axis from one another.

Finally, I observe a secondary modulational instability that gives rise to fluctuations in the intensity of the generated light. The frequency of these fluctuations depends directly on the angle between the counterpropagating pump beams. For well-aligned pump beams, this instability is greatly suppressed, for pump beams misaligned by $\theta_p \simeq 0.4$ mrad, the instability has a characteristic frequency of $\sim$245 kHz. In the next Chapter, I present an all-optical switch that is based on controlling the orientation of

the transverse optical patterns discussed above.

Chapter 5

A Cascadable All-Optical Switch

In Chapter 4, I presented a counterpropagating beam system in rubidium vapor that exhibits pattern formation. The focus of this Chapter, and the primary focus of this thesis, is the application of this pattern forming system to ultra-low-light-level all-optical switching. At first glance, a system that generates transverse patterns and an all-optical switch may seem to have little in common. However, as I will demonstrate in the first section of this Chapter, certain features of the generated patterns make them particularly useful to switching.

5.1 Switching with patterns

As described in Chapter 4, a pair of counterpropagating pump beams, with sufficient intensity and misaligned by $\theta_p \sim 0.4$ mrad, generate a pattern that takes the form of a pair of spots. The spots are symmetrically located on a cone characterized by a cone angle $\theta = 4$ mrad between the surface of the cone and the pump beam axis. This situation is illustrated in Fig. 5.1(a), and a typical image of the pattern generated for this case is shown in Fig. 5.1(b). This system can be used as an all-optical switch because the orientation of the generated patterns is extremely sensitive to perturbations. As discussed in Sec. 4.2.4, the pump beam alignment and any optical imperfections influence the orientation of the patterns. A perturbation can then be used to control the orientation of the patterns, such as a weak beam that is injected into the nonlinear medium. For clarity, I will refer to such a weak beam as the switch beam, because it

serves as the input, or control, to the device. When a switch beam with the same state of polarization as the generated patterns is injected into the rubidium vapor and along the surface of the cone, I observe that the pattern rotates such that one of the spots is aligned with the switch beam, see Fig. 5.1(c,d). Thus, there are two states of pattern orientation, one for the unperturbed case, and one for the perturbed case. These two states of the pattern orientation can be defined as two states of the switch, *off* and *on* respectively.

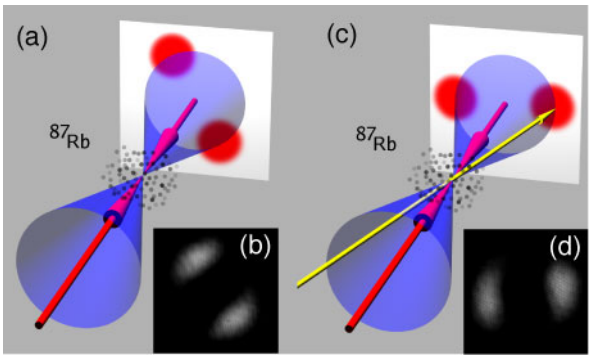

Figure 5.1: A two-spot transverse optical pattern rotates when a switch beam is injected into the rubidium vapor.

In accordance with the cylindrical coordinates appropriate to this system, I refer to the orientation angle of the patterns as the azimuthal angle. I define 0° as the orientation of the unperturbed pattern, as indicated in Fig. 5.2. I find the pattern is most sensitive to the switch beam when it is injected at an azimuthal angle of ±60°. This can be understood in terms of the hexagonal symmetry of the pattern-forming instability discussed in Chapters 3 and 4. For a given pump-beam alignment there are six preferred spot locations. The weak symmetry breaking inherent to the system sets the orientation of these six locations, and the pump beam misalignment selects the two locations to be illuminated. Figure 5.2 illustrates this underlying symmetry of the system. In the absence of a switch beam, I observe the orientation of the pattern is stable for several days provided the optical system and pump-beam alignment have

not been modified. This pattern orientation, however, is only weakly preferred over other two orientations shown in Fig. 5.2. In particular, the two other orientations with azimuthal angles $\pm 60^\circ$ are supported by the fundamental hexagonal symmetry of the pattern-forming process and are preferred over orientations with arbitrary azimuthal angles.

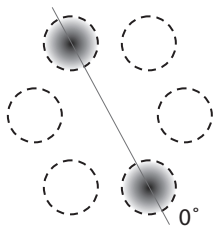

Figure 5.2: The symmetry of the pattern-forming system shows six preferred directions of emission. The two dark spots illustrate the typical two-spot pattern I observe for misaligned pump beams.

The preference toward one pattern orientation can be controlled via the pump-beam misalignment. With large misalignment ($\theta_p \geq 1$ mrad), the pattern is a pair of spots whose orientation is strongly pinned and requires a larger perturbation to induce rotation. With small or no misalignment ($\theta_p \leq 0.1$ mrad), the pattern exhibits more than two spots and the pattern orientation is observed to spontaneously changes between the preferred states. Achieving sensitive all-optical switching requires striking a balance between both regimes. If the patterns are strongly pinned, actuating the switch requires more switch-beam power, and if the patterns are weakly pinned, the switch will not be stable.

I have shown how the pattern orientation can be controlled by an external perturbation, but this device does not yet have well-defined output channels. To be practical as an all-optical switch, the generated patterns must be directed in such a way that the device output corresponds to one of the generic all-optical switch types introduced

in Fig. 2.1. This can be accomplished via spatial filtering where two apertures select portions of the pattern that are either dark or illuminated depending on the orientation state of the pattern, see Fig. 5.3. Placing an aperture around the location of a spot in the *on* state defines one output port of the device, and likewise an aperture that passes one of the *off*-state spots defines a second output port. These apertures could readily be replaced by optical fibers that constitute two different communications channels.

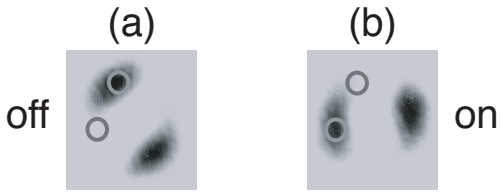

Figure 5.3: Apertures spatially filter spots corresponding to the two states of the switch. a) The *off* state. b) The *on* state.

This spatial filtering could be expanded to include a second *on* state, where the azimuthal angle is $-60°$. In this case, there would be three outputs, and three switch states. This configuration might be used as a router, where signals are routed to one of three outputs. The signal used in a router could be encoded by amplitude modulation of the pump-beams which would thus modulate the intensity of the generated light. Rotating the patterns would then correspond to routing the encoded signal to one of three possible output channels.

The next section describes the experimental setup I use to observe ultra-low-light all-optical switching with transverse optical patterns. The remainder of the chapter includes a characterization of the response of the device to various input power levels, measurements of the number of photons required to actuate the device, and a discussion of these results.

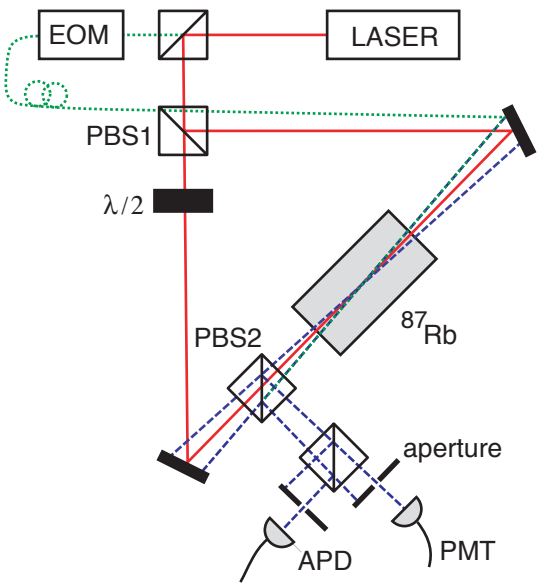

Figure 5.4: Experimental setup for all-optical switching with transverse patterns. The output of a frequency-stabilized cw Ti:Sapphire laser serves as the source. A polarizing beamsplitter (PBS1) separates the forward (cw) and backward (ccw) beams within the triangular ring cavity. The backward beam is brought into horizontal polarization by a half-wave plate ($\lambda/2$). The forward and backward beams counterpropagate through a warm ^{87}Rb vapor contained in a 5-cm glass cell. A polarizing beam-splitter (PBS2) reflects instability-generated light in the vertical polarization which is observed by a photomultiplier tube module (PMT) and an avalanche photodiode (APD). An aperture placed in front of each detector spatially selects one spot from either the *on* state or the *off* state of the pattern orientation. A weak switching beam (dashed green) with the same polarization as the generated patterns (orthogonal to that of the pump beams) is modulated using a Mach-Zehnder electro-optic modulator (EOM) and injected into the cell at a slight angle $\theta = 4$ mrad to the pump beam axis.

5.2 Experimental setup

The experimental setup is nearly identical to that described in Sec. 4.1. The only changes are the addition of the switch beam, and the installation of a photomultiplier tube module in place of the CCD camera. The additional detector allows simultaneous observation of both output ports of the device.

The switch beam is derived from the same master laser and is amplitude modulated by a fiber-based Mach-Zehnder electro-optic modulator (EOM). The EOM operates by inducing an equal and opposite phase shift in two arms of a lithium-niobate

($LiNbO_3$) waveguide arranged as a Mach-Zehnder interferometer. This configuration allows high-speed amplitude modulation with an on-off extinction ratio greater than 20 dB using drive signals on the order of 2 V. The EOM has an operating bandwidth of 20 GHz and is driven by the output of an arbitrary waveform generator (Stanford Research Systems SRS345, 30 MHz bandwidth) with a programmed waveform. The response time of the EOM under these driving conditions (∼10 ns), is significantly faster than the response time of the pattern rotation (∼2 μs).

The switch beam is collimated with 1/e field radius $w_0 = 185\,\mu$m and has a state of polarization identical to that of the generated light, and thus orthogonal to that of the pump beams. This polarization configuration is selected to efficiently seed the generation of off-axis light, thus allowing very weak switch beams to rotate the generated pattern.

Other parameters of the system have been fixed at values I have optimized for switch sensitivity. The temperature of the cell is held at 80° C, the pump beam power is 415 μW in the forward direction, and 145 μW in the backward direction. The pump beams are collimated with 1/e field radius ($1/e^2$ intensity radius) $w_0 = 450\,\mu$m located at the center of the cell. As mentioned above, the pump beams are slightly misaligned with an angle $\theta_p \sim 0.4$ mrad between their axes.

5.3 Switch Response

To quantify the dynamic behavior of the switch, I inject of series of pulses by turning the switch beam on and off with the EOM. Spatially filtering the output pattern enables direct measurement of the switch behavior. High-contrast switching is confirmed by simultaneously measuring two output ports. Figure 5.5(a) indicates the power of the injected switch beam as a function of time. The signal from the off-state detector

is shown in Fig. 5.5(b) and is high when the switch beam is not applied and low during a switch-beam pulse. The on-state detector is shown in Fig. 5.5(c) and shows the opposite behavior, it is low when the switch beam is not applied and high during each switch-beam pulse. These alternating signals demonstrate switching of the power from one switch state to another with high contrast. As discussed in Chapter 4, the total power generated in the pattern is $\sim 3\,\mu$W. Each aperture selects one of the two generated spots, so the switch output power is $\sim 1.5\,\mu$W per aperture. Of course, two apertures could be used per switch state to transmit the full $\sim 3\,\mu$W output.

As shown in Fig. 5.5(a), I inject switch beam pulses that steadily decrease in power, which allows me to sample the response of the system to various input levels. The data shown in Fig. 5.5 are collected in a single shot that contains 22 additional ten-pulse sets with similar response. No signal averaging has been performed on the switch response data (Fig. 5.5(b,c)) the measured switch-beam power shown in Fig. 5.5(a) is averaged over 10 shots. One notable feature of the system response is the transition from complete switching to partial switching. The first three pulses in Fig. 5.5 show that the on-state detector is fully illuminated and the off-state detector is dark. This indicates that the switch beam has caused complete rotation of the pattern and transferred all of the power from the off-state spots to the on-state spots. For the last seven pulses in the series, the system exhibits partial switching, where the on-state detector is partially illuminated and the off-state detector is partially darkened. This partial response indicates that the off-state spots are suppressed but not extinguished when the switch beam is applied with less than 900 pW. Similarly the on-state spots are generated but not at full power. In this intermediate regime, from 900 pW to <300 pW, the response depends on the input power.

To explore the low-input-power regime more thoroughly, I decrease the overall switch beam power so that the 10 input pulses range from 510 pW to 35 pW. The

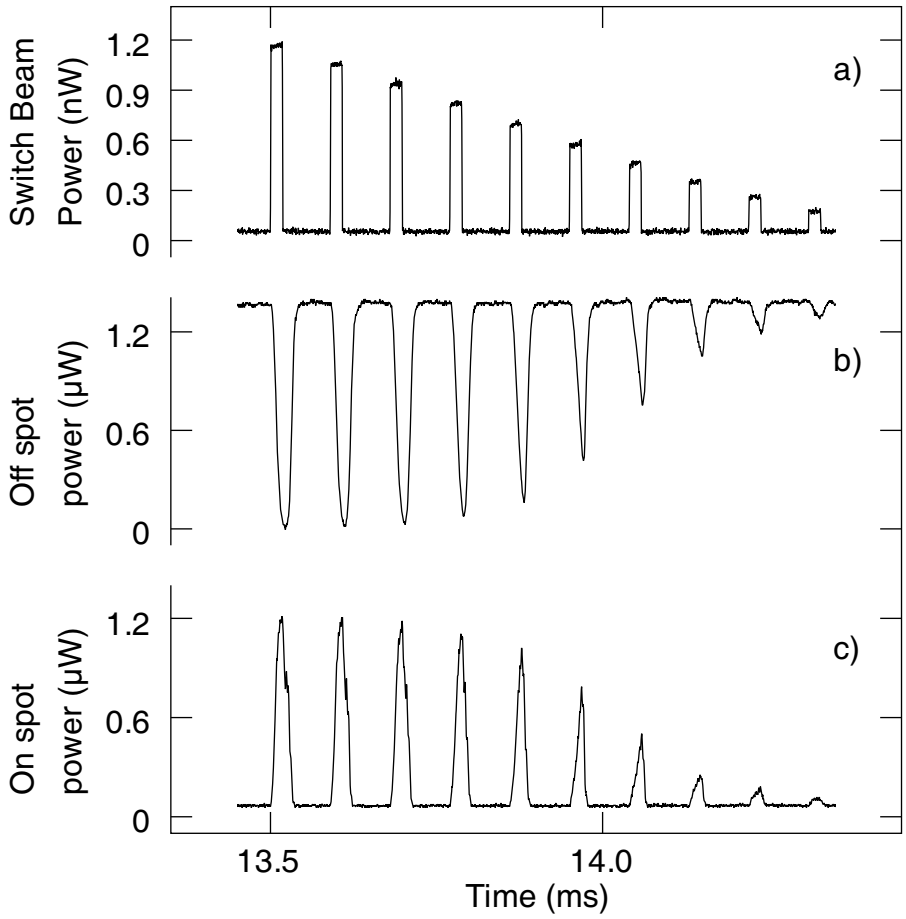

Figure 5.5: The switch responds to a series of ten pulses by transferring power from the *off* state spots to the *on* state spots. a) The switch beam power steadily decreases in power from 1.2 nW to 200 pW. b) The off spot is extinguished in the presence of the switch beam. c) The on spot power increases in the presence of the switch beam.

switch response corresponding to this lower input range is shown in Fig. 5.6. Again, Fig. 5.6(a) shows the switch-beam power, Fig. 5.6(b) shows the off-state signal which decreases during the application of the switch beam, and Fig. 5.6(c) shows the on-state signal, which increases during the application of the switch beam. The response shown is similar to the final few pulses of Fig. 5.5 in that the off-spot is suppressed rather than extinguished, and the on-spot is illuminated but not saturated. The linear response of the switch to low input power is clear from this data as well, and both the on-spot and the off-spot respond proportionally to the input.

Also visible in Figs. 5.6 and 5.5 is a weak secondary modulational instability (MI) that causes oscillations in the total output power. These oscillations are more clear in Fig. 5.7, an enlarged trace showing only the eighth on-spot pulse of Fig. 5.6. As discussed in Sec. 4.2.5, the frequency of this instability is determined by the pump-beam misalignment. For the typical alignment, $\theta_p \simeq 0.4$ mrad, the frequency is 250 kHz, also evident in Fig. 5.7. I observe switching with low input power only when the pump beams are misaligned, hence the MI is unavoidable to a certain degree. To limit the effect of the MI on the switch response, I operate with the pump beam power $\simeq$15% above threshold. Under different experimental conditions, the MI can be significantly larger. In optimizing the performance of this device, I have found specific ways to reduce the MI to the level shown here. The details of how to minimize the MI while maintaining sensitive switching are given in Appendix A.

The modulation period of this secondary instability and the characteristic response time of my switch both correspond to the transit time of a thermal atom through the pump beams. Assuming a Maxwell-Boltzman speed distribution, the average speed of

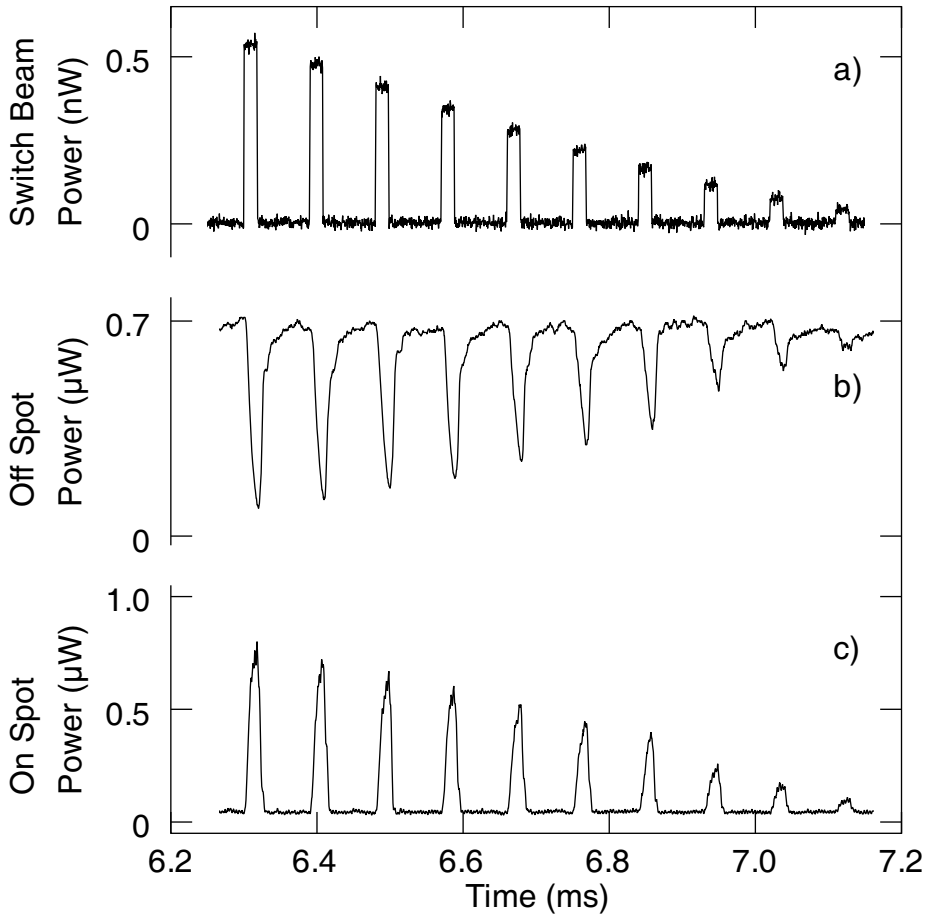

Figure 5.6: The switch responds to a series of ten pulses by transferring power from the *off* state spots to the *on* state spots. a) The switch beam power steadily decreases in power from 510 pW to 35 pW. b) The off spot is suppressed in the presence of the switch beam. c) The on spot power increases in the presence of the switch beam.

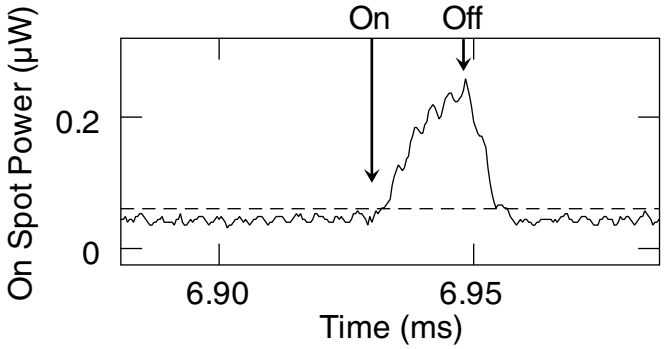

Figure 5.7: A single on-spot pulse where the secondary modulational instability is visible as a 250 kHz (4 μs period) oscillation in the detected power. The dashed line indicates the threshold level used to determine the response time τ_r. The data shown correspond to the eighth peak in Fig. 5.6(c) where the switch beam power is 100 pW. The arrows indicate the rising and falling edges of the electronic signal driving the EOM.

an atom at $T = 355$ K=80 °C is

$$\bar{v} = \left(\frac{8kT}{\pi m}\right)^{1/2} = 290\,\mathrm{m/s}. \tag{5.1}$$

where $k = 1.38 \times 10^{-23}$ J/K is Boltzmann's constant and m is the atomic mass. The transit time through pump beams with radius $w_0 = 455$ μm is then 3 μs. Physically, the transit time limits the amount of time any single atom interacts with the pump beams, and therefore is a characteristic time-scale for the nonlinearity due to optical pumping. On average, every transit time, new atoms with thermalized population distributions enter the pump beams, and the ensemble of optically-pumped atoms exits the interaction region.

This time-scale suggests that the pattern-forming instability and the secondary instability are both induced by the nonlinear response of the rubidium vapor due to optical pumping. Near an atomic resonance, optical pumping is known to provide large nonlinearities that are known to lead to bistability, instabilities, and chaos [37, 38, 60].

I also observe that the switch response exhibits a rise-time that is slower than its fall-time. The arrows in Fig. 5.7 indicate when the switch-beam is initially applied and when it is turned off. The on-spot signal increases gradually during the entire 20 μs switch-beam pulse yet the signal falls back to the baseline less than ~ 7 μs after the switch-beam is turned off. One possible explanation for this observation is that the pattern orientation is being seeded by the switch-beam and gradually builds up in a manner analogous to laser oscillation build up. Once the switch-beam is turned off, there is no seed for the new orientation and the pump beams quickly drive the pattern back to the preferred orientation. The secondary instability also contributes to the dynamics of the pattern so it is also possible that the pattern orientation is being driven parametrically by the secondary instability, and once the switch beam is turned off, the orientation is quickly driven back to the off-state by the secondary instability.

5.3.1 Switching photon number

To quantify the sensitivity of the system, I measure the response time and from this calculate the number of photons N_p required to actuate the switch. I define the response time τ_r of the device as the time between the initial rising edge of the electronic signal driving the EOM and the point where the on-spot signal crosses a threshold level set to roughly correspond to a signal-to-noise ratio of $\sim$3 dB, see Fig. 5.7.[1] The SNR$\sim$3 dB criterion corresponds to the threshold where the bit-error-rate decreases below 0.05, *i.e.*, it is the point where pulses can be correctly detected with probability greater than 5% [63]. Results using this threshold are shown in Fig. 5.8(a) and I find that the measured response time increases as the input switch beam power decreases.

The response times for the switch are on the order of a few μs, whereas the re-

[1]For the data shown, the threshold is applied in post-processing and is chosen to be as low as possible without decreasing the data fidelity. This could, of course, be automated in the real-time detection using standard error-checking algorithms.

sponse time of the measurement system is on the order of 35 ns. The avalanche photodiode used to collect the data shown in Figs. 5.5-5.7 has a signal bandwidth of 10 MHz, and the data is digitized using an oscilloscope with 500 MHz bandwidth. The delay between the switch beam turn-on, and the initial rising edge of the electronic EOM drive signal is less than 35 ns, and is thus two orders of magnitude smaller than the response time of the switch.

The number of photons required to actuate the switch is given by $N_p = \tau_r P_s / E_p$ where τ_r is the response time, P_s is the switch beam power and $E_p = 2.54 \times 10^{-19}$ J is the photon energy. For the ten switch-beam powers corresponding to Fig. 5.6(a), the response time is plotted in Fig. 5.8(a), and the number of switching photons is plotted in Fig. 5.8(b). The response time is longer for weak switch-beam powers so the photon number decreases gradually as the input power decreases. The error bars represent one standard deviation in the response times observed for a single oscilloscope trace containing 22 sequential sets of 10 pulses each. Hence, the data points correspond to the average of 22 data points corresponding to each switch-beam pulse.

The implication of the linear regression shown in Fig. 5.8(b) is that, in the limit as $P_s \rightarrow 0$, the number of switching photons $N_p \rightarrow 400$. This would indicate that the minimum number of photons capable of actuating the switch is roughly 400. The final data point shown correspond to switching with $N_p = 600 \pm 40$, only 200 photons above this limit, and a factor of ∼5 lower than my first reported observation of all-optical switching with 2,700 photons [12].[2] This estimate of a minimum photon number is addressed in more detail in Chapter 7 where I discusses the ultimate performance limitations facing this device. Also, the improvements I have made to the experimental system since the conducting the preliminary work are described in Appendix A.

[2]The error reported in this value of N_p is a combination of systematic error in the measurement accuracy of the switch-beam power (∼0.5%), and statistical variations in the response time measured for 22 sequential shots (∼5%).

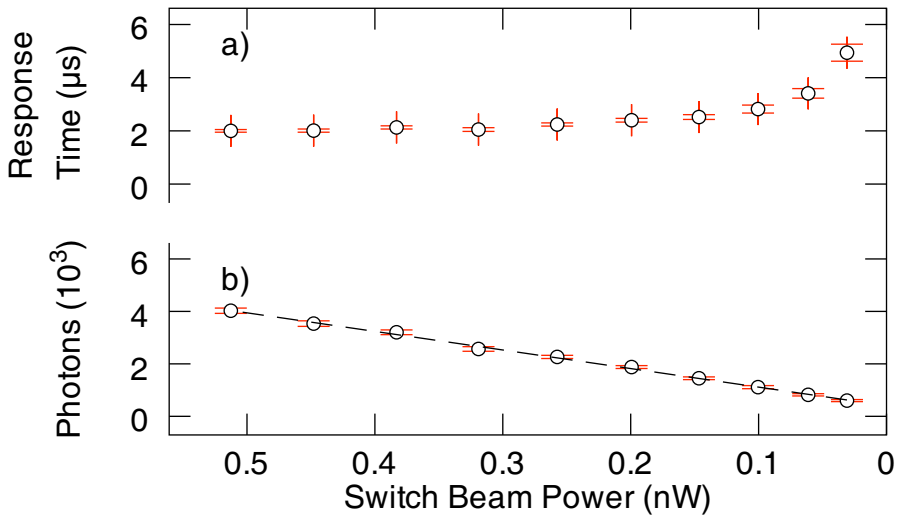

Figure 5.8: The response time τ_r and number of switching photons N_p as a function of input power. Data are generated from 22 sequential traces like the one shown in Fig. 5.6 acquired after a single trigger. The error bars indicate one standard deviation of the measured values. The dashed line indicates the fit: $N_p = 7081P_s + 404$ for P_s in nW.

5.3.2 Transistorlike response

The response shown in Fig. 5.5, demonstrating the saturated and linear response regimes, suggests that this device operates in a manner that is analogous to an electronic transistor. Furthermore, the two response regimes exhibited by the switch indicate that the output satisfies the conditions for signal level restoration, as discussed in Sec. 2.3.

For a device to exhibit signal level restoration, variations in the input level cannot cause variations in the output level. In every device, however, there is a narrow range of input levels, known as the intermediate region, that lead to intermediate output levels. For input levels above or below the intermediate range the output is *saturated* as a logic high or low respectively. In the case of my switch, this intermediate region is between 900 pW and <35 pW. For input levels above 900 pW, the output is high with

a level set by the pump beam power.

Signal level restoration is a key property of the electronic transistor enabling large networks of electronic logic elements. This demonstration of an optical logic element that exhibits level restoration is a key step towards practical optical switches. An all-optical transistor would have applications in many data processing and communication networks in the future.

5.4 Discussion

To compare the sensitivity of my switch to those discussed in Sec. 2.4, I evaluate the energy density in photons per $\lambda^2/(2\pi)$. For the switching beam spot size used, (1/e field radius) $w_0 = 185 \pm 5\,\mu$m, 600 $\pm$40 switching photons correspond to a switching beam energy density of $5.4 \pm 0.7 \times 10^{-4}$ photons/$\lambda^2/(2\pi)$. Therefore, both EIT-based switches [9] and my pattern-based switch have surpassed the minimum value (1 photon/$\lambda^2/(2\pi)$) originally expected for optical logic operations [6]. Both approaches operate at very low light levels, although my system is markedly simpler than cold-atom EIT systems or cavity QED systems, requiring only one optical frequency and occurring in warm atomic vapor.

In addition to being extremely sensitive, the output generated by my switch is much larger than the required input. While I observe switching with as few as 600 photons, the output ($\sim 3\,\mu$W) corresponds to over 23 million photons for $\tau_r = 2\,\mu$s. The output of this switch could thus actuate thousands of similar switches, and hence the switch is cascadable.

Another figure of merit in all-optical switching is the contrast-to-noise ratio (CNR). This is defined as the ratio of the on-off difference to the noise in either state. As discussed in Sec. 5.3, the noise is dominated by the secondary modulational instability.

For the saturated response shown in the first pulse of Fig. 5.5 the peak of the pulse is 1.23 μW and the modulation amplitude due to the secondary instability is 0.0062 μW, corresponding to a CNR of 200-to-1. Even for the final pulse in the partial-switching regime shown in Fig. 5.6, the on-off contrast is 0.05 μW, and the amplitude of the noise is 0.008 μW, corresponding to a CNR of 6.3-to-1.

The two primary limitations of this device are that the response time typically ranges from $\tau_r = 2 - 5\,\mu$s, and that it cannot be actuated by a single photon. The response time implies that the switch can only operate with data rates on the order of 500 kb/s, far too low for modern optical communications bandwidths of 40 Gb/s and higher. There are several potential avenues for improving the response time and sensitivity of an all-optical switch based on transverse pattern formation. Two promising options involve replacing the nonlinear medium. Instead of warm rubidium vapor, cold atoms held in a long-narrow trap may provide a medium capable of switching with a single photon. I have contributed to recent work developing a sample of cold atoms with comparable optical depth, large nonlinear phase shift, and naturally-broadened atomic transitions [64]. Working in cold atoms has two major benefits. First, the atomic motion is limited, hence the wave mixing processes do not suffer from refractive-index grating wash-out. Second, the amount of absorption experienced by a near-resonant beam is significantly lower when the atomic transitions are not Doppler broadened. Thus, the benefit of resonant enhancement of the nonlinearities is not outweighed by increased absorption. To put it another way, for a given frequency near an atomic resonance, the amount of absorption relative to the nonlinear phase shift is much lower in cold atoms. The decrease in absorption can potentially increase the sensitivity of a pattern-based switch and may be sufficient to reach the single-photon switching level.

Using cold rubidium atoms will not, however, improve the response time of the

switch. For this, a medium with inherently faster nonlinear response is required. Very recent work by Schumacher *et al.* [65], motivated by my results, shows that planar semiconductor microcavities are a nonlinear medium that may be used in high-speed transverse-pattern all-optical switching. Four-wave mixing instabilities can occur in a single semiconductor quantum well via nonlinear excitonic processes. Such instabilities have been shown theoretically to give rise to forward four-wave mixing gain similar to what I observe in my experiment. Furthermore, numerical models of such instabilities demonstrate that they may be suitable for use as all-optical switches using a similar switching scheme based on rotating patterns between preferred states with hexagonal symmetry [65]. The model in [65] considers the coupling between the six directions corresponding to each of the six spots in a hexagonal pattern. These numerical results show the response time of a quantum well switch can be less than 1 ns. However, the sensitivity of this switch is not high enough to exhibit single-photon switching. A model that includes the full two-dimensional system may show different results, but these initial findings are very promising and will hopefully demonstrate the use of high-speed all-optical switches based on transverse-patterns.

An interesting observation is that the response time of my switch and the typical period of the secondary modulational instability (MI) are of the same order: $2-4\,\mu$s. This time scale also corresponds to the typical ground-state optical pumping time for rubidium. The origin of the nonlinearity in the rubidium vapor is due to optical pumping, so it is likely that this time scale is fundamental to the nonlinearity responsible for the pattern-forming instability. However, there appears to be a synergistic relationship between the MI and the pattern-forming instability. I observe that the sensitivity of the switch is highest when the pump beams are misaligned such that the MI has a characteristic time scale of $2\,\mu$s. Hence, the MI helps de-stabilize the pattern and thus increases the sensitivity of the switch. If the pump beams are well aligned, the pattern

is observed to spontaneously switch between the preferred states, so a small amount of pump-beam misalignment is crucial to increasing the stability of the switch. However, if the patterns are strongly pinned, more power is required in the switch beam to induce rotation and thus actuate the switch. The MI, therefore, introduces some 'jiggle' that allows a weak switch beam to induce pattern rotation.

The question naturally arises: What limits the sensitivity of the switch? As shown in Fig. 5.8, an estimate for the minimum number of photons capable of actuating the switch is 400 photons. The switch sensitivity is largely limited by spontaneous pattern rotation, which appears as spontaneous switching if the pump beams are not sufficiently misaligned. It may be that this spontaneous switching is in fact induced by very weak perturbations provided by photons arriving in the various modes corresponding to any of the other preferred pattern orientations. However, before this conclusion could be accurately drawn, all other potential sources of perturbing beams would have to be ruled out. As an example, the pump beams scatter from the entrance and exit windows of the cell and may depolarize slightly, introducing light that could induce rotation. Other sources of symmetry-breaking are typically time-dependent, such as beam pointing noise and vibration of the optics. The system exhibits extreme sensitivity to perturbations, hence it can be used as a sensitive all-optical switch. This sensitivity, however, is limited by the degree of control over all other sources of symmetry breaking in the system.

5.5 Summary

This chapter has demonstrated the application of transverse optical patterns to ultra-low-light all-optical switching. The system described in Chapter 4 generates patterns that are extremely sensitive to perturbations. A perturbation in the form of a weak

switch beam injected into the nonlinear medium is suitable for controlling the orientation of the generated patterns and thus operating as a switch where each state of the pattern orientation corresponds to a state of the switch. Spatial filtering of the generated pattern defines the output ports of the device, and measurements of the switch response show that it can be actuated by as few as 600 ±40 photons. For a switch beam with 1/e field radius $w_0 = 185 \pm 5\,\mu$m, 600 ±40 photons correspond to $5.4 \pm 0.7 \times 10^{-4}$ photons/$\lambda^2/(2\pi)$. My approach to all-optical switching operates at very low light levels, exhibits cascadability and transistorlike response, and is markedly simpler than cold-atom EIT systems or cavity QED systems, requiring only one optical frequency and occurring in warm atomic vapor.

Chapter 6

Numerical Modeling of the All-Optical Switch

In Chapter 3, I presented a theoretical model that describes pattern formation in counterpropagating beam systems. Chapters 4 and 5 describe my experimental observations of pattern formation and all-optical switching, respectively, in such a system where warm rubidium vapor serves as the nonlinear material. In parallel to my experimental work, I seek to determine the minimum ingredients required for a theoretical model to describe the switching behavior I observe experimentally. Previous attempts to simulate numerically all-optical pattern formation have been successful. Based on the model of Firth and Paré, numerical simulations performed by Chang *et al.* describe hexagonal pattern formation in a counterpropagating beam system [11]. This model, and the results of Chang *et al.* , serve as a starting point for my own numerical simulations.

The purpose of this Chapter is to describe my extension of [11] to simulate all-optical switching with transverse patterns. Specifically, I simulate the effect of a weak switch beam on the orientation of the hexagonal pattern generated by gaussian pump beams that counterpropagate through a Kerr-type nonlinear medium. Simulations of the time response of this system show behavior that is qualitatively similar to my experimental observations. In particular, the response time increases as the switch-beam power decreases.

In regards to the content of this Chapter, I owe extra thanks to Dr. Alex Gaeta of Cornell University for providing me with working Fortran code that implemented the split-step beam-propagation method in one transverse dimension (see Sec. 6.3).

Although none of the original code remains in my simulations, without getting started by standing on his shoulders, I would not have been as readily successful.

6.1 3-D nonlinear model

In order to simulate a full three-dimensional system, the model of Firth and Paré, presented in Sec. 3.4, is generalized here to include both transverse dimensions. This model is scalar, *i.e.* it does not account for the vector nature of the fields, and hence cannot describe polarization instabilities, and it also does not include absorption effects. Nonetheless, it is sufficient to describe pattern formation in counterpropagating-beam nonlinear optical systems. As presented in Chapter 3, the following two equations describe the forward and backward fields counterpropagating through a Kerr medium, (also see Eq. (3.30)),

$$\left(\frac{\partial}{\partial z}+\frac{n_0}{c}\frac{\partial}{\partial t}\right)F=\frac{i}{2k}\frac{\partial^2}{\partial x^2}F+i(|F|^2+2|B|^2)F \tag{6.1}$$

$$\left(-\frac{\partial}{\partial z}+\frac{n_0}{c}\frac{\partial}{\partial t}\right)B=\frac{i}{2k}\frac{\partial^2}{\partial x^2}B+i(|B|^2+2|F|^2)B, \tag{6.2}$$

where n_0 is the linear refractive index in the medium, c is the speed of light in vacuum, k is the wavevector within the medium, and F (B) is the forward (backward) field amplitude. These equations further assume a nonlinear medium with positive n_2 as appropriate for my experimental system, described in Chapter 5.

To normalize the variables in this model, I choose to scale the longitudinal units by the cell length L, the transverse units by the beam waist w_0, and hence the field strength carries additional length units as illustrated in Table. 6.1, where $t_r = n_0 L/c$ is the transit time through the medium and the Fresnel number of the system ($\mathscr{F} =$

$w_0^2/\lambda L$) relates the transverse and longitudinal length scales. The Fresnel number can also be considered as a measure of the number of transverse modes supported by the geometry of the system. For large $\mathscr{F}$, many transverse modes are allowed and rich spatial structure is typically observed. The numerical results presented in this chapter are for $\mathscr{F} = 5.3$, corresponding to the experimental results presented in Chapter 5.

Normalized	Original
$\tilde{z}$	z/L
$\tilde{x}$	x/L
$\tilde{t}$	t/t_r
$\tilde{F}$	$F\sqrt{L}$
$\tilde{B}$	$B\sqrt{L}$
κ	Kw_0

Table 6.1: Equivalence between normalized units and the original physical units.

Rewriting Eqs. (6.1) and (6.2) using these variables yields the following pair of dimensionless equations:

$$\left(\frac{\partial}{\partial\tilde{z}} + \frac{\partial}{\partial\tilde{t}}\right)\tilde{F} = \frac{i}{4\pi\mathscr{F}}\frac{\partial^2}{\partial\tilde{x}^2}\tilde{F} + i(|\tilde{F}|^2 + 2|\tilde{B}|^2)\tilde{F} \tag{6.3}$$

$$\left(-\frac{\partial}{\partial\tilde{z}} + \frac{\partial}{\partial\tilde{t}}\right)\tilde{B} = \frac{i}{4\pi\mathscr{F}}\frac{\partial^2}{\partial\tilde{x}^2}\tilde{B} + i(|\tilde{B}|^2 + 2|\tilde{F}|^2)\tilde{B}. \tag{6.4}$$

Generalizing this model to two transverse dimensions is straightforward. The transverse derivative in x is simply replaced by the transverse Laplacian operator

$$\nabla_\perp^2 = \frac{\partial^2}{\partial x^2} + \frac{\partial^2}{\partial y^2}. \tag{6.5}$$

For simplicity, I will drop the tilde notation, and for the remainder of this Chapter, the variables are assumed to be in their normalized units, unless otherwise noted. The

amplitude equations, including two transverse dimensions, are thus given by

$$\left(\frac{\partial}{\partial z}+\frac{\partial}{\partial t}\right)F=\frac{i}{4\pi\mathscr{F}}\nabla_{\perp}^{2}F+i(|F|^{2}+2|B|^{2})F \tag{6.6}$$

$$\left(-\frac{\partial}{\partial z}+\frac{\partial}{\partial t}\right)B=\frac{i}{4\pi\mathscr{F}}\nabla_{\perp}^{2}B+i(|B|^{2}+2|F|^{2})B. \tag{6.7}$$

These amplitude equations can now be integrated by numerical methods. The following section describes a technique for reducing this set of PDEs to a pair of ODEs, and the following section describes a particularly efficient numerical integration scheme known as the split-step beam-propagation method (BPM) [66–68].

6.2 Method of Characteristics

For a first-order hyperbolic partial differential equation (PDE), such as Eqs. (6.6,6.7), the method of characteristics can be used to find curves, known as characteristics, along which the behavior of the PDE is simplified and can be described by an ordinary differential equation (ODE). To solve for the characteristics of Eqs. (6.6,6.7), and for notational simplification that will become clear in later sections, it is useful to re-write the amplitude equations in terms of two operators $\mathscr{L}$ and $\mathscr{N}$

$$\left(\frac{\partial}{\partial z}+\frac{\partial}{\partial t}\right)F=(\mathscr{L}+\mathscr{N})F, \tag{6.8}$$

where

$$\mathscr{L}(F)=\frac{i}{4\pi\mathscr{F}}\nabla_{\perp}^{2}F, \tag{6.9}$$

$$\mathscr{N}(F)=i(|F|^{2}+2|B|^{2})F, \tag{6.10}$$

are operators describing linear diffraction and nonlinear wave mixing respectively, with similar equations for B. To apply the method of characteristics to Eq. (6.6), I start by parameterizing z and t as $z = z(s), t = t(s)$ for the parameter s and assume an initial point on the characteristic (z_1, t_1). Thus, I want to solve for the characteristic starting at (z_1, t_1), such that the evolution of F along the characteristic is described by dF/ds. This characteristic is illustrated in Fig. 6.1 where it traces a path in the space defined by z and t. The chain rule allows me to rewrite the left hand side of Eq. (6.8) as:

$$\frac{dF}{ds} = \frac{dz}{ds}\frac{\partial F}{\partial z} + \frac{dt}{ds}\frac{\partial F}{\partial t}. \tag{6.11}$$

The equations have already been scaled such that the characteristics have a simple form. If I set

$$\frac{dz}{ds} = 1 \quad \text{and} \quad \frac{dt}{ds} = 1, \tag{6.12}$$

then 6.8 gives:

$$\frac{dF}{ds} = (\mathscr{L} + \mathscr{N})F. \tag{6.13}$$

Equation (6.12) gives $z = s + z_1$ and $t = s + t_1$. Solving these for s and equating yields:

$$z - z_1 = t - t_1, \tag{6.14}$$

or simply $z = t$ where I have taken $(z_1, t_1) = (0, 0)$.

These characteristics have a simple physical interpretation, by momentarily revert-

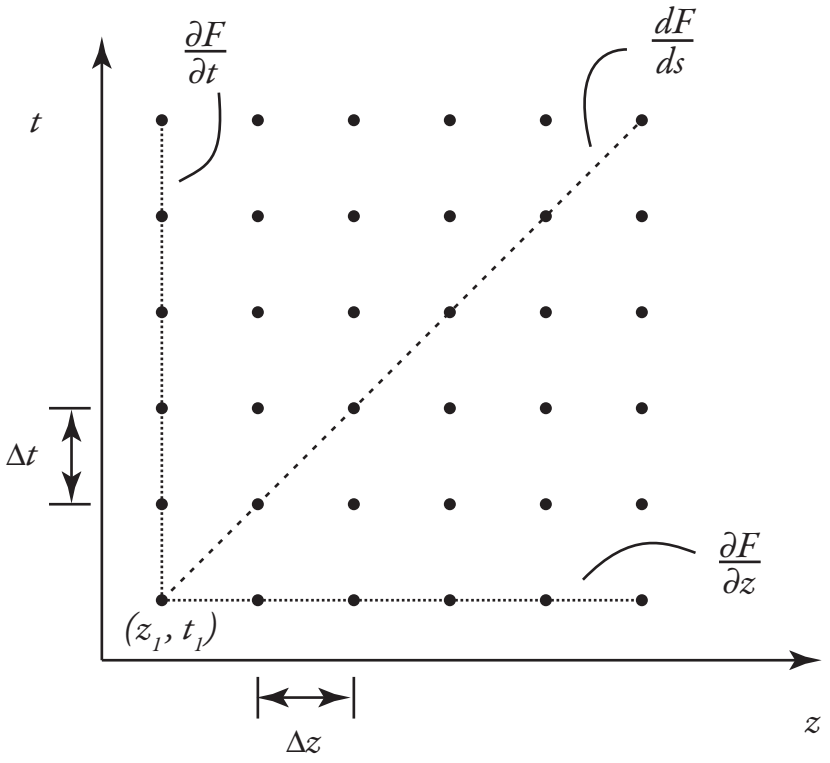

Figure 6.1: The characteristic for Eq. (6.8), illustrated in z-t space, can be described by dF/ds. Using variables with physical units, $\Delta z = (c/n)\Delta t$, hence the characteristic is the light-line for a propagating wave.

ing to variables with physical units via Table 6.1, we see that

$$\frac{z}{L} = \frac{t}{t_r} = \frac{tc}{n_0 L} \tag{6.15}$$

$$z = \frac{c}{n_0} t, \tag{6.16}$$

also illustrated in Fig. 6.1. Hence, the characteristics are the lines through space-time that describe a wave propagating along the z axis with phase velocity $\pm c/n_0$. In the case of wave equations, the characteristics always have this interpretation, and thus the method of characteristics can generally be used to reduce PDEs describing wave propagation to ODEs along the light-lines of each propagating wave.

Numerical integration may thus take place along the characteristics of the wave equation by taking each numerical step in time and space simultaneously. In the case presented here, this allows the simplification of Eq. (6.6) as

$$\frac{dF}{dt} = (\mathscr{L} + \mathscr{N})F, \tag{6.17}$$

where z is replaced with t corresponding to integration along the characteristic $z = t$. The following section describes how numerical integration of Eq. (6.17) is achieved via the split-step beam propagation method.

6.3 Split-step beam propagation method

The method of characteristics has reduced the partial differential equation given by Eq. (6.8) to an ordinary differential equation. The primary difficulty in solving numerically this set of equations is that they contain both linear and nonlinear terms. The

split-step BPM [66] is a numerical technique for efficiently integrating the linear and nonlinear portions of a wave equation by alternately treating linear diffraction in the Fourier domain and the nonlinear terms in the spatial domain.

The foundation of the BPM is that the Maxwell equations for counter-propagating beams in a nonlinear medium can be approximated by a set of m thin slices separated by regions of empty space.[1] Waves propagating through this sequence of spaces and slices experience only linear diffraction in the empty space and only a nonlinear phase shift within each slice. This model medium is illustrated in Fig. 6.2.

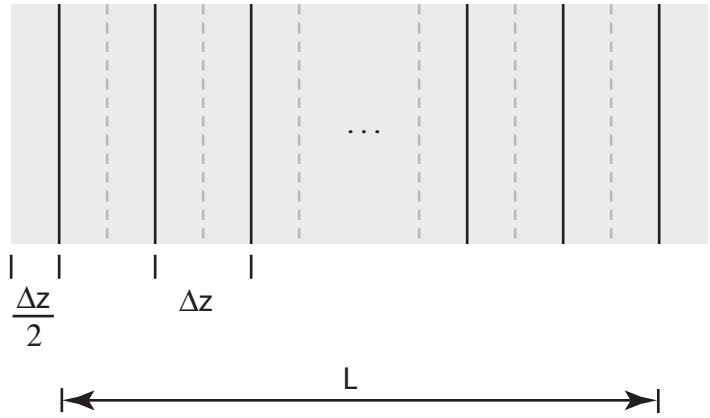

Figure 6.2: A model medium of length L illustrating the split-step BPM. Slices of nonlinear media (solid black lines) separated by free-space (grey) of length Δz combine to approximate the effects of a medium that exhibits both linear diffraction and nonlinear wave mixing. The dashed grey lines indicate the boundary between each unit cell consisting of of free space, nonlinear slice, and free space.

The approximation of the medium as a series of slices originates from approximating the solution to Eq. (6.17) as [69, 70]

$$F(x,z_1,t_1) = \exp\left(\mathscr{L}\frac{\Delta t}{2}\right)\exp(\mathscr{N}\Delta t)\exp\left(\mathscr{L}\frac{\Delta t}{2}\right)F(x,z_0,t_0) + \mathscr{O}(\Delta t^3), \quad (6.18)$$

[1] I have chosen to denote the number of slices m in order to avoid any confusion with the index of refraction. In the literature, n is commonly used for both.

where $\Delta t = t_1 - t_0$, and $z_0 = z(t_0)$, with a similar equation for B.

It is straightforward to apply the nonlinear operator in the spatial domain because the operator contains only multiplication operations. From Eq. (6.10), a single time-space step through a nonlinear slice is calculated via

$$F(x, y, z_1, t_1) = \exp(\mathcal{N} L_m) F(x, y, z_0, t_0) = \exp[i(|F|^2 + 2|B|^2) L_m] F(x, y, z_0, t_0), \tag{6.19}$$

where $L_m = L/m$ for m slices.

The linear operator could be applied in the spatial domain; however, such an operation requires calculating a second-order spatial derivative, which is computationally intensive. Fortunately, the linear operator can be applied in the Fourier domain very efficiently via the Fast-Fourier Transform algorithm [66]. For the Fourier transform $\widetilde{F}(\kappa_x, \kappa_y, z, t)$ of $F(x, y, z, t)$, Eq. (6.9) becomes

$$\frac{d\widetilde{F}}{dz} = \frac{i}{4\pi\mathscr{F}} (\kappa_x^2 + \kappa_y^2) \widetilde{F}, \tag{6.20}$$

with solution

$$\widetilde{F}(K_x, K_y, z_1, t_1) = \exp(-i\theta_n) \widetilde{F}(\kappa_x, \kappa_y, z_0, t_0) \tag{6.21}$$

$$\theta_n = \frac{(\kappa_x^2 + \kappa_y^2) \Delta z}{4\pi\mathscr{F}}, \tag{6.22}$$

where $\Delta z = L/(m-1)$, with m slices.

A subtlety of the solution described in Eq. (6.18) is that the approximation is only exact for a physical system where the length of the nonlinear medium is not equal to the total length of propagation. This is illustrated in Fig. 6.2 where there is an

extra half-step of free-space propagation on either side of the nonlinear slices. The nonlinear medium I use in my experiments is contained within a glass cell of length $L = 5$ cm, so including the extra half-step on each side of the simulated medium is equivalent to measuring the field a small distance away from the cell. However, the measurements of the switch response I make experimentally are all in the far-field; hence, this approximation is suitable for simulating my experimental system. If I were to simulate the effects of placing this medium within a cavity, extra consideration must be paid to the effect of additional regions of free-space propagation.

Another consequence of approximating a continuous medium with a set of discrete slices is an artificial instability that can arise due to the inherent periodicity of the slices. In the thin-slice model, each beam experiences phase modulation within a nonlinear slice and the free-space propagation can then convert this phase modulation into an amplitude modulation via diffraction. Penman *et al.* [69] show, by linear stability analysis, that specific values of the transverse wavenumber K experience no amplitude modulation (*i.e.*, they are only phase-shifted) due to the specific periodicity of the model system. This can result in an instability for large-K that does not correspond to an instability in the continuous model. To avoid this artificial instability, spatial filtering is implemented that excludes transverse wavevectors that satisfy $K > (\pi k/\Delta z)^{1/2}$, or using the notation of Eq. (6.22), $\theta_n > \pi/2$. During a discussion of this issue, Dr. William Firth clarified for me that this filtering was implemented by Chang *et al.* [11]. This filtering has been applied in my simulations, and I do not observe the large-K instability.

A final step in modeling hexagon formation numerically is a source of symmetry breaking required to overcome the square symmetry of the numerical grid. The model implemented by Chang *et al.* [11] successfully demonstrated two sources of symmetry-breaking, noise added to the initial gaussian beams, and anisotropy in the numerical

grid. I have observed hexagon formation using either of these techniques in addition to a third technique where I inject a weak off-axis probe beam for a few transit times very early in the course of the simulation. This weak beam serves to seed the instability and also selects the initial pattern orientation.

6.4 Numerical Results

The previous work of Chang *et al.* shows that three-dimensional simulations of counter-propagating gaussian beams exhibit transverse patterns. Specifically, they demonstrate that generalizing the model of Firth and Paré to two transverse dimensions leads to the formation of hexagonal patterns in agreement with a large number of experimental results (see [11] and References therin). Chang *et al.* find the formation of hexagons for pump powers just above the threshold predicted by Firth and Paré and well below the threshold predicted by Yariv and Pepper.

It must be made clear that neither the simulations conducted by Chang *et al.* nor the simulations I conduct, are intended for direct comparison with experimental results. This would require refinement of the model for the nonlinear response of the medium to accurately describe the nonlinear response of rubidium vapor (see Chapter 3 for a discussion of the limitations of the Kerr model).

6.4.1 Pattern Formation

The primary result presented by Chang *et al.* is the formation of hexagonal patterns in a three-dimensional model of gaussian beams counterpropagating through a medium exhibiting Kerr nonlinearity. Their simulations are conducted with $\mathscr{F} = 63.7$ and $IL = 0.565$ where the threshold for plane-wave pattern formation predicted by Firth

and Paré is $IL \simeq 0.45$. Therefore, Chang *et al.* simulate pattern formation for pump beams that are 25% above the minimum plane-wave threshold.

I have conducted simulations with a wide range of $\mathscr{F}$ between 63.7 and 4, where my experimental conditions correspond to $\mathscr{F} = 5.3$. Simulations in this range all exhibit hexagonal pattern formation and reproduce the results of Chang *et al.*; I use this as one criterion for confirming my computational implementation of the BPM.[2] The primary difference between the results for different $\mathscr{F}$ is simply the opening angle θ of the cone describing the generated light. From the analysis of Firth and Paré, the instability threshold is lowest for $K^2L/2k \simeq 3$. Given $\mathscr{F} = w_0^2/\lambda L$, and $\kappa = w_0 K$, the minimum instability threshold corresponds to a dimensionless transverse wavevector of $\kappa^2 = 12\pi\mathscr{F}$. Clearly larger $\mathscr{F}$ results in a larger transverse wavevector generated by the instability; hence, my observation that small $\mathscr{F}$ results in small θ. In order to simulate the geometry of my experiment, the results presented below are of simulations where $\mathscr{F} = 5.3$ and $IL = 0.565$ ($\sim 25\%$ above threshold).

Images of the far field pattern generated in a typical run of my simulation are shown in Fig. 6.3 where the time corresponding to each frame is indicated in units of the transit time $t_r = nL/c$. In the initial frame of Fig. 6.3, the transmitted forward pump-beam is visible at the center, and the weak off-axis perturbation is visible to the right. This perturbation is used to quickly induce hexagonal pattern formation. Without the initial perturbation, hexagons are observed after 100-150 transit times. At $t_r = 17$, the field that is conjugate to the perturbation, and due to forward four-wave mixing, is visible to the left of the central pump. The Fast-Fourier Transform (FFT) is used to compute these far-field images, and one artifact of this is a large-narrow peak corresponding to zero spatial frequency (DC). This feature is located in the center of

[2]Other criteria for confirming that I have correctly implemented the BPM are simulating gaussian beam propagation [14], and nonlinear self-focusing [71], both of which are correctly reproduced using the appropriate parameters.

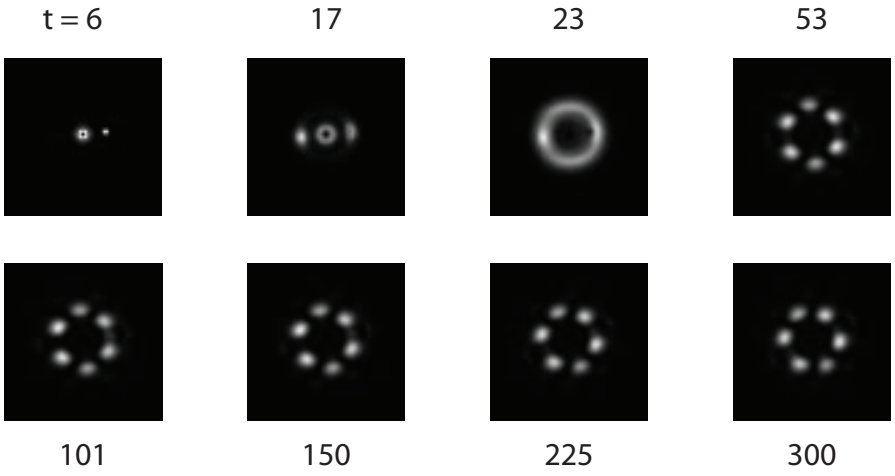

Figure 6.3: Numerical simulation of counterpropagating gaussian beams shows ring and hexagon pattern formation in the far field.

the frame and is much narrower than the transmitted pump beam. The dark dot in the central spot of the first two frames is the result of numerical filtering that I use to remove this component of the image. At $t_r = 23$, a ring pattern has formed that is replaced by hexagons at $t_r = 53$. The perturbing beam is turned off at $t_r = 35$ and is not visible at $t_r = 53$. It is interesting to note that the ring pattern, predicted by naively generalizing the models of Yariv and Pepper or Firth and Paré to cylindrically symmetrical transverse dimensions is a transient solution that appears early in the development of the off-axis patterns. The ring is not a stable solution for the system in the presence of symmetry breaking, due in this case to the initial perturbation beam, and the ring breaks up into six spots after a short time. The second row of frames shown in Fig. 6.3 were collected after the application of an off-axis switch-beam, which turns on at $t_r = 85$, and are discussed in the next section.

6.4.2 Switch Response

In my simulations, much like in my experiments, I observe that injecting a weak switch beam into the nonlinear medium after hexagons have formed causes the hexagon pattern to rotate such that a bright spot is aligned to the direction of the switch beam. This rotation is illustrated in the lower four frames of Fig. 6.3. The switch beam is applied at $t_r = 85$, and becomes visible between the two right-side spots at $t_r = 101$. For the frames shown, the switch beam power is $P_s = 10^{-4}P_p$, where P_p is the power of each of the counterpropagating pump beams. At $t_r = 150$, the counterclockwise rotation of the pattern can be observed and continues until the end of the simulation at $t_r = 300$ where the pattern has rotated such that the locations that were previously bright are now dark.

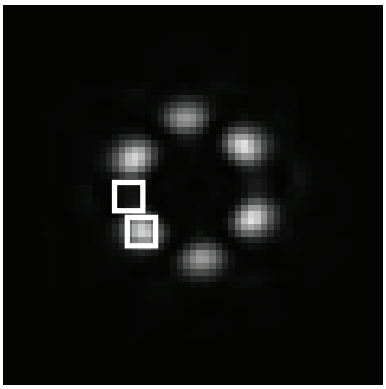

Figure 6.4: The location of the on- and off-state apertures are indicated relative to the initial hexagon pattern that forms at $t_r = 53$. The on-state aperture (upper square) is located opposite the applied switch beam, and the off-state aperture (lower square) transmits the spot immediately counter-clockwise from the on-state aperture.

As in the switch I demonstrate experimentally, the patterns generated in this simulation can be spatially filtered in order to define two or more output channels. Figure 6.4 indicates the location of the apertures used to filter the numerical results.

Square apertures are used for numerical efficiency, but the results are not expected to differ if they are replaced with round apertures. The power transmitted by these apertures is calculated by summing the simulated intensity values within each aperture. For four simulation runs, each with different switch-beam power, the power transmitted through the on- and off-state aperture as a function of transit time t_r is shown in Fig. 6.5(a) and (b), respectively.

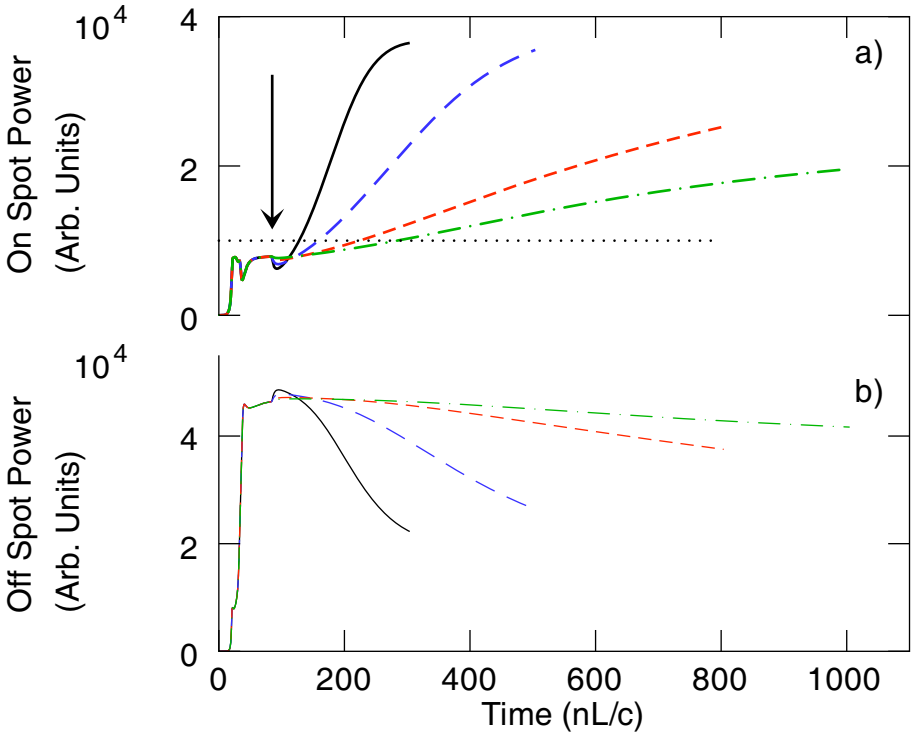

Figure 6.5: The power transmitted by apertures in the numerical model exhibits switching behavior that is similar to the experimental system. The response of the on- and off-state aperture transmission is shown for four levels of switch-beam power. The switch beam is turned on at $t_r = 85$, indicated by the arrow in (a). As the switch-beam power decreases, the simulation exhibits slower response, *i.e.* slower pattern rotation. The switch-beam power (in units of pump-beam power) corresponding to these four traces are 10^{-4} (solid black), 2.5×10^{-5} (lg. dash blue), 4×10^{-6} (sm. dash red), and 1×10^{-6} (dash-dot green). The horizontal dotted line indicates the threshold used to calculate response times for the simulated switch.

After the initial transients in the pattern formation, the power in the off- and on-

spots stabilize within 50 transit times. At $t_r = 85$, the switch-beam is applied and the pattern begins to rotate, transferring power from the off-state aperture to the on-state aperture. For $P_s = 10^{-4} P_p$, complete rotation occurs within 200 transit times. For lower switch beam power, the pattern rotates more slowly as the remaining traces show in Fig. 6.5. To compare the change in response time observed in the simulation to that observed experimentally, I measure the response time of the simulated switch as the time between the application of the switch beam ($t_r = 85$) and the threshold crossing for the on-spot. The threshold, also shown in Fig. 6.5, is chosen to roughly correspond to the level of the experimental threshold.

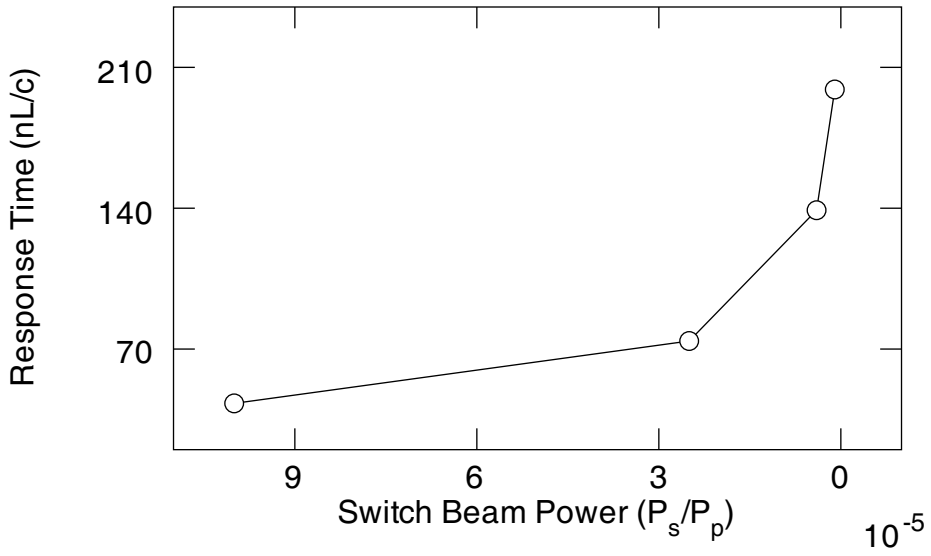

Figure 6.6: Simulation of the switch exhibits an increase in response time for decreasing power that is qualitatively similar to experimental observations. To facilitate comparison to Fig. 5.8(a), the horizontal axis has high switch-beam power to the left and low switch-beam power to the right.

The response time of the simulated switch data shown in Fig. 6.6 ranges from 40 transit times to 210 transit times, as shown in Fig. 6.6. For comparison, the transit time of the 5 cm vapor cell used in my experiment is 160 ps, so the simulated response times would correspond to experimental values of 6.4 ns and 33.6 ns respectively. As

P_s/P_p	P_s[nW]
1×10^{-4}	26
2.5×10^{-5}	6.5
4×10^{-6}	1
1×10^{-6}	.26

Table 6.2: The correspondence between P_s/P_p and P_s in nW based on 560 μW of total pump power.

described in Chapter 5, I observe response times between 2 and 4 μs experimentally, so it is clear that the numerical model does not agree quantitatively with my experimental observations. However, the simulated response time does exhibit a sharp increase in the limit of low switch-beam power, which is qualitatively similar to my experimental observations. This increase in response time for weak inputs indicates that the switch undergoes critical slowing down, which suggests that the orientation of the pattern exhibits multi-stability between the preferred orientations.

Another notable feature of these numerical results is that, despite the limitations of the model, the amount of switch-beam power, relative to the total pump power, required to rotate the pattern is of the same order of magnitude as what I observe experimentally. For reference, Table. 6.2 shows the correspondence between the normalized switch-beam power P_s/P_p used in the simulations presented above and the experimental values, based on total pump-beam power, from my experiments, of $P_p = 560$ μW. As an example, the third curve in Fig. 6.5 corresponds numerically to $P_s = 4 \times 10^{-6} P_p$. In my experiment, this switch-beam to pump-beam power ratio would imply a switch-beam power of 1 nW. In my experiment, the switch typically operates between 1 nW and 50 pW. Therefore, the sensitivity exhibited by my experiment is largely described by this model.

There are certainly features of the experiment that these simulations do not capture. In the first case, absorption is neglected in assuming a Kerr-type nonlinearity. One

consequence of this is that misalignment of the pump beams in the simulation does not serve to reduce the number of spots generated. This is likely due to the fact that, without absorption, there is no loss experienced by the less-favored hexagonal components and even for large pump-beam misalignment, the pattern remains a hexagon. Simulations that include misalignment of the forward pump beam exhibit hexagonal pattern formation in addition to fluctuations in the pattern orientation and a near-field pattern flow [55]. Just as for well-aligned pump beams, the switch beam also causes pattern rotation when the forward pump beam is misaligned, and the switch response time diverges near zero switch-beam power in the misaligned case as well.

As I discuss in the following Chapter, symmetry breaking may be responsible for pinning the orientation of the pattern. However, including pump-beam misalignment in these simulations does not have this effect: even weak switch beams cause pattern rotation and there does not seem to be a critical switch-beam power required to rotate the pattern. Refinement of the model to include absorption and saturation may improve the agreement between my experiment and the simulation. Furthermore, because I have assumed a medium with an instantaneous nonlinear response, the only timescale in the Kerr model is the transit time. This leads to significantly faster switch response in the model compared to my experimental observations. To quantitatively model the response time requires a more refined model of the nonlinear interaction that includes optical pumping effects and the associated time scales.

6.5 Summary

Pattern formation in nonlinear optical systems has been well-studied via experiment, theory and numerical modeling. Previous simulations, based on the Kerr model described by Firth and Paré, have been conducted by Chang *et al.* and exhibit the for-

mation of hexagon patterns for a wide range of simulation parameters. I extend this result by showing that not only are hexagonal patterns generated by this model, but the model also describes pattern rotation induced by an external switch beam. Furthermore, this model successfully reproduces the general relationship between the switch response time and the switch-beam power that I observe experimentally.

The only timescale included in the model is the transit time, so the fact that the response time depends on the strength of the perturbation may be a universal feature of all-optical switching with transverse patterns.

The qualitative agreement between this simple model and my experimental observations indicate that the transparent Kerr medium, although different from rubidium vapor in important ways, describes many of the features that make transverse optical patterns useful to applications in all-optical switching.

Chapter 7

Ultimate performance limitations

The previous chapter presents my results from simulating all-optical switching with transverse optical patterns. The results generated from these simulations and my experimental results both exhibit increased response time for low switch-beam powers. This chapter presents a conjecture that the increased response time at low switch-beam power is due to critical slowing down. I support this conjecture by mapping the pattern orientation to a simple first-order one-dimensional system. Numerical integration of this model demonstrates an increased response time for weak perturbations, which exhibits a scaling law that is similar to my experimental observations and simulated results.

For clarity, I am using the concept of critical slowing down from the nonlinear dynamics community. In this sense, critical slowing down refers to the situation where the eigenvalue of a system crosses through zero at a bifurcation point leading to a diverging time-scale. This corresponds to the case where a stable fixed point of a system becomes weakly stable and the decay to such a fixed point occurs more slowly.

7.1 A toy model

A conceptually simple way to describe the dynamics of a system is in terms of a potential that the system seeks to minimize. My experimental observations and numerical simulations suggest that the pattern forming system discussed in this thesis obeys a potential with a ring-shaped well containing six valleys equally spaced around the ring

and separated by $\pi/3$ radians (corresponding to 60°). The individual valleys represent the six preferred spot locations while the diameter of the well is set by the cone angle $\theta \simeq \sqrt{3\lambda/(\pi L)}$ described in Chapter 3. A three-dimensional plot of such a potential is shown in Fig. 7.1. It should be noted that this potential is motivated solely by the observed patterns and is thus totally phenomenological and does not correspond to any physical property of the system as far as I know.

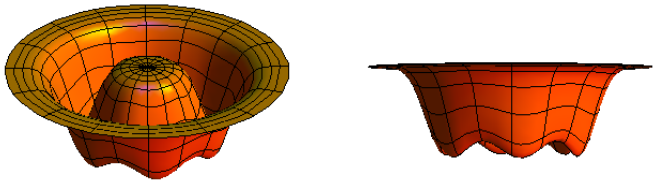

Figure 7.1: Two views of the symmetric potential with six wells of equal depth which gives rise to six-spots.

To explore the features of this model in quantitative detail, I examine the functional form of the potential shown in Fig. 7.1 given in cylindrical coordinates ρ and ϕ by

$$V(\rho,\phi,r,h) = -re^{-\frac{(\rho-1)^2}{0.1}}(1+h\sin 6\phi), \tag{7.1}$$

where r and h parameterize various portions of the potential well. The parameter r scales the overall depth of the well and h scales the relative depth of the individual valleys that contribute to the hexagon structure. As an example, for $h = 0$, the potential well takes the form of a single ring of uniform depth and for $h = 1$ the six wells range from depth $-2r$ to maximum height $V = 0$. I have normalized the radial coordinate such that $\rho = d\theta$, where d is the distance from the nonlinear medium to the measurement plane and θ is the cone opening half-angle of the generated light. There is also an arbitrary constant equal to 0.1 scaling the radial extent of the ring potential, this has been chosen to qualitatively correspond to my observations and does not effect the

dynamics of the system along the azimuthal angle.

If I assume that the system finds the global minimum via noise and quantum fluctuations, then the patterns corresponding to the potential shown in Fig. 7.1 are expected to exhibit six spots of equal intensity because each well is equally deep. To introduce the possibility of symmetry breaking, I include additional terms in the potential of the form

$$V_p(\rho,\phi) = (1+\cos 2\phi)\rho^2, \tag{7.2}$$

and correspond to a restoring force that breaks the rotational symmetry such that two of the six spots have slightly lower minima and thus become slightly preferred. The general effect of this term is to fold the potential upwards in the shape of a taco as shown in Fig. 7.2.

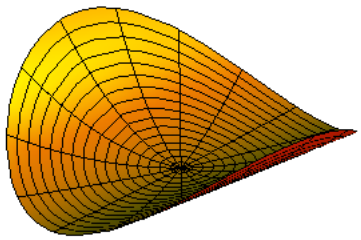

Figure 7.2: Fundamental symmetry-breaking folds the potential along one axis.

Introducing two of these symmetry-breaking terms allows me to describe changes in the potential caused by two symmetry-breaking mechanisms: one due to fundamental symmetry-breaking in the system such as via pump-beam misalignment, and the other due to the applied switch beam. The full functional form of the toy-model

potential is then given by

$$V(\rho,\phi,r,h,p,s) = -re^{-\frac{(\rho-1)^2}{0.1}}(1+h\sin 6\phi) + p\left(1+\cos\left(2\left(\phi+\pi/6\right)\right)\right)\rho^2 + s\left(1+\cos\left(2\left(\phi-\pi/6\right)\right)\right)\rho^2, \tag{7.3}$$

where the new parameters p and s scale the two symmetry-breaking terms corresponding to the fundamental symmetry-breaking and the switch-beam symmetry-breaking, respectively. Because the switch beam is applied at a fixed azimuthal angle relative to the unperturbed pattern orientation, the only difference between the two new terms are that they are offset by $\Delta\phi = \pi/3$.

To visualize the effect of broken symmetry on the potential, Fig. 7.3 shows V for the case where there is only fundamental symmetry breaking ($p \neq 0$ and $s = 0$). There is clearly a fold in the potential due to the symmetry breaking and from the side view there are now only two global minima rather than six, which can be seen more easily from the side view. These minima corresponding to the two-spot pattern with the orientation preferred by the system.

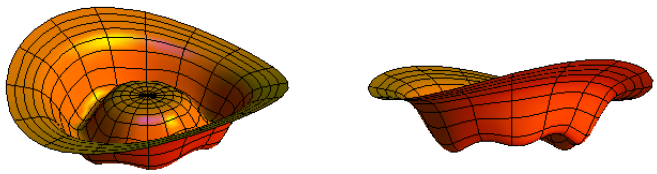

Figure 7.3: Fundamental symmetry breaking folds the six-well potential and lifts the degeneracy of the wells leaving two spots preferred. The parameters used in Eq. (7.3) to generate this plot are $p = 0.1$, $r = 1$, $h = 0.1$, and $s = 0$.

Alternatively, when the unperturbed system is perfectly symmetric and only the switch beam breaks the symmetry of the system, the potential changes to the one

shown in Fig. 7.4. The orientation of the fold in the potential has changed, corresponding to the orientation of the switch beam. From a side view of the potential, there are still two global minima; however, the orientation of these minima has changed by 60° relative to the unperturbed system. The combination of both symmetry-breaking contributions results in a potential that can have either orientation as a global minima depending on the relative strength of the fundamental symmetry-breaking and the switch-beam perturbation.

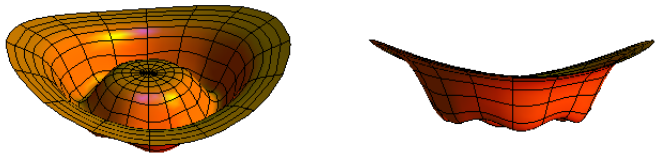

Figure 7.4: Potential well for the case of a fundamentally symmetric system that has been perturbed by the switch beam. There are still two global minima but now they have been rotated by $\pi/3$ relative to Fig. 7.3. The parameters used in Eq. (7.3) to generate this plot are $p = 0$, $r = 1$, $h = 0.1$, and $s = 0.1$.

In order to simplify the description of the orientation angle, I move from this two dimensional picture, to a one-dimensional system by considering the circle corresponding to $\rho = 1$ and allowing ϕ to vary through 2π. This one-dimensional system thus corresponds to a 1D flow along the circle $\rho = 1$. The following discussion uses this 1D model to predict the pattern orientation angle in terms of the relative strengths of the two symmetry-breaking terms described above.

The change in the 1D potential caused by increasing s, which corresponds to increasing the switch beam strength, can be seen in Fig. 7.5. The lower curve corresponds to the potential where there is only fundamental symmetry-breaking. There is a global minimum at $\pi/3$. As s increases, shown by the higher curves, the local minimum at $2\pi/3$ becomes the global minimum as s becomes larger than p. Also note, for $s > 0.35$, there is only one minimum for $0 < \phi < \pi$. Therefore, regardless

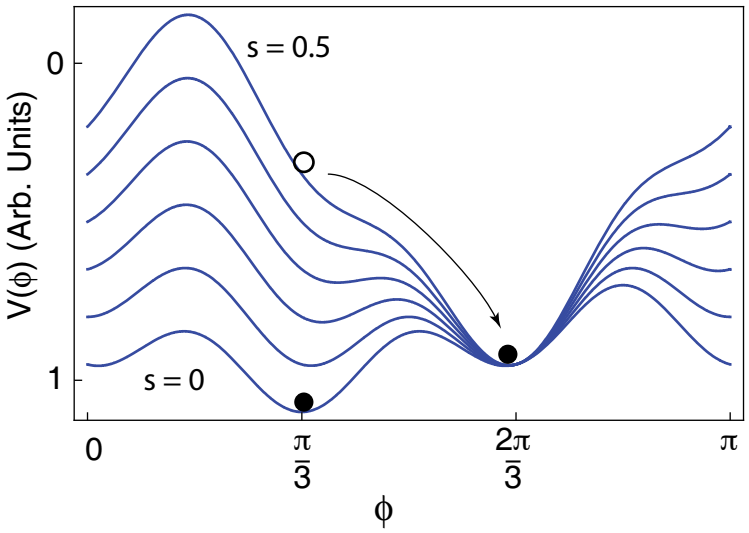

Figure 7.5: The one-dimensional potential corresponding to the ring where $\rho = 1$. The curves correspond to $p = 0.1$, $r = 1$, $h = 0.1$, and s between 0 (bottom curve) and 0.5 (top curve) in steps of 0.1. As s increases, the global minimum at $\pi/3$ shifts upward and is replaced by a global minimum at $2\pi/3$ when $s > 0.1$. When $s = p = 0.1$, the two orientations have equal V and are thus equally preferred.

of the initial orientation of the pattern, applying a switch-beam perturbation corresponding to $s > 0.35$ will cause the pattern to rotate. Drawing an analogy between the one-dimensional potential and a ball resting on a hill, we see that, for $s = 0$, the orientation state $\phi = \pi/3$ is stable. As s increases the local minimum at $\phi = \pi/3$ becomes shallow, and for $s > 0.35$ the minima disappears and the ball rolls down the hill to rest in the nearest stable state $\phi = 2\pi/3$.

In order for the ball and hill analogy to be explicitly accurate for this model, it is important to clarify that I consider this system in the overdamped limit. Explicitly, the overdamped limit corresponds to assuming that inertial forces are much smaller than damping forces. From Newton's second law

$$F = m\ddot{\phi} + b\dot{\phi} = -\frac{dV}{d\phi}, \tag{7.4}$$

where I take $m << b = 1$ giving

$$\dot{\phi} = -\frac{dV}{d\phi}. \tag{7.5}$$

This simplification also ignores any transients that occur during the pattern formation process and assumes that once the pattern is formed, the dynamics of the pattern orientation ϕ is governed by a one-dimensional first-order equation $\dot{\phi} = f(\phi)$. This assumption is not related in any way to the atomic, or optical properties of the system, it is simply made to generate a toy model that serves to demonstrate the topological origin of critical slowing down in a pattern-forming system with weakly broken symmetry. A more accurate analogy for Fig. 7.5, to borrow from Strogatz [2], would be of a ball rolling down a hill through a layer of viscous goo so there is no possibility of overshoot or oscillation.

The temporal dynamics of this one-dimensional system can be observed via numerical integration of the first-order equation

$$\dot{\phi} = -\frac{dV}{d\phi} = -6hr\sin 6\phi + 2p\sin\left(2\left(\phi + \pi/6\right)\right) + 2s\sin\left(2\left(\phi - \pi/6\right)\right), \tag{7.6}$$

where the parameters r, h, p, and s are as before. The depth of the potential well is scaled by r so for the remainder of this chapter, I set $r = 1$. Similarly, the preference toward hexagon patterns is parameterized by h where $h = 1$ yields six potential wells of depth r and $h = 0$ leaves the entire 1D system at a constant potential. For the purposes of illustrating this toy model, I choose $h = 0.1$ so the height of the barrier between each of the six spots is one tenth of the depth of the ring-shaped well. The relative strengths of s and p are of primary interest to the problem so I set $p = 0.1$ and allow s to vary over the range $[0, 0.5)$.

Once the applied symmetry-breaking perturbation overcomes the fundamental asym-

metry of the system, the orientation ϕ will change. This corresponds to the switch action I observe experimentally: with an applied switch-beam, I can change the orientation of the generated patterns. The toy model switch response is shown in Fig. 7.6 for increasing values of s, analogous to increasing amounts of switch-beam power. The first curve shows that for $s = 0.35$, the initial state is stable even after the perturbation is applied. In the language of nonlinear dynamics, the point $\phi_0 = \pi/3$ is a weakly-stable fixed point of the system. For $s > 0.35$ the pattern angle ϕ changes from $\pi/3$ to $2\pi/3$ corresponding to rotation by 60°.

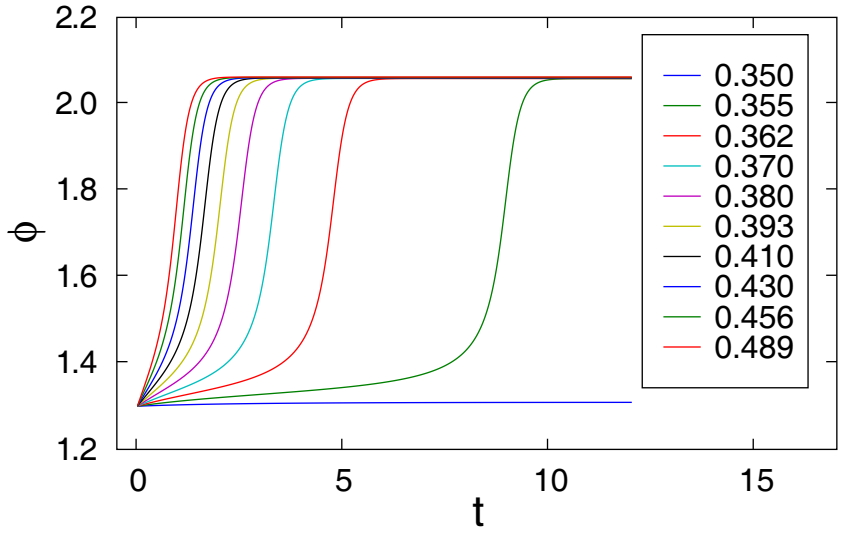

Figure 7.6: The 1D model response to symmetry-breaking perturbations in the range $0.35 \leq s < 0.49$. Once the applied perturbation overcomes the potential barrier between two orientation states, the orientation changes. This change occurs more quickly for larger perturbations (*i.e.*, for larger s).

To compare the behavior of this model to my experimental and numerical results, I measure the response time τ_{1D} as the time between the initial perturbation (in the case of the toy model $t = 0$) and the time ϕ passes a threshold set at $\phi_{on} = 1.5$. The measured response time as a function of the perturbation parameter s is shown in Fig. 7.7. The response time is slowest (τ_{1D} is largest) for perturbations that are just above the

threshold for switching, which is consistent with my experimental observations and simulation results. This phenomena can be explained by critical slowing down, which is known to occur near weakly-stable fixed points in a one-dimensional flow [2].

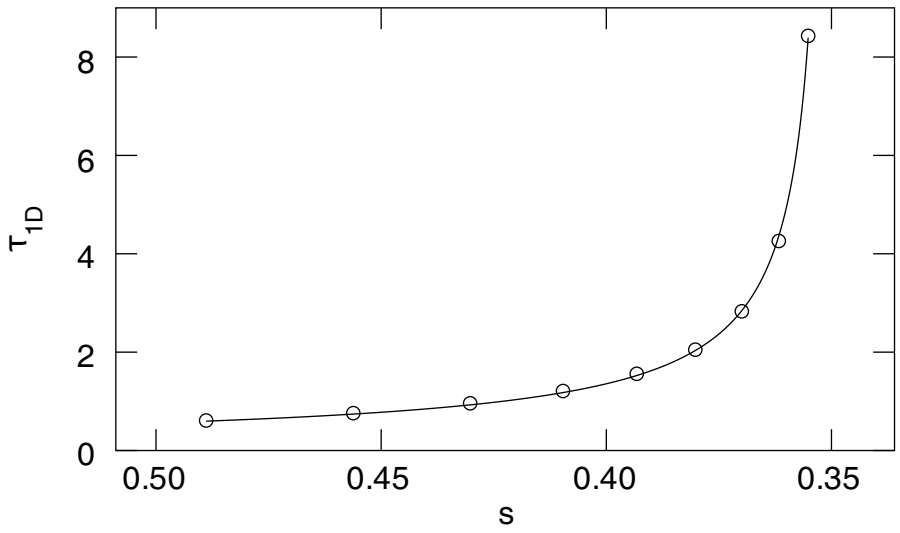

Figure 7.7: The response time measured for the 1D model shows critical slowing down as the perturbation parameter s decreases towards the critical value $s_c = 0.35$. For $s < 0.35$, no pattern rotation occurs.

The response time $\tau_{1D}(s)$ increases as a power law as s decreases toward the critical value for pattern rotation $s_c = 0.35$. A fit of this functional form yields

$$\tau_{1D}(s) \propto (s - s_c)^{-0.8 \pm 0.02}, \tag{7.7}$$

where the critical value $s_c = 0.35$ is the maximum value of s where ϕ is stable, *i.e.*, where the pattern does not rotate because it is pinned by the fundamental symmetry breaking.

7.2 Performance implications

Interesting implications arise for the ultimate performance of my switch after considering this simple 1D model. My experimental results, simulations of an analogous nonlinear optical system, and this model based on symmetry arguments all exhibit an increase in the response time as the strength of the applied perturbation decreases. In the case of my experiments and simulations, this perturbation is the injected switch beam. The 1D model suggests that the strength of the applied perturbation must be sufficient to overcome fundamental symmetry-breaking that exists in the unperturbed system. The functional relationship between the perturbation strength and the response time is given as an inverse power law that diverges at the critical perturbation strength. If the perturbation strength is below this critical value, no pattern rotation occurs.

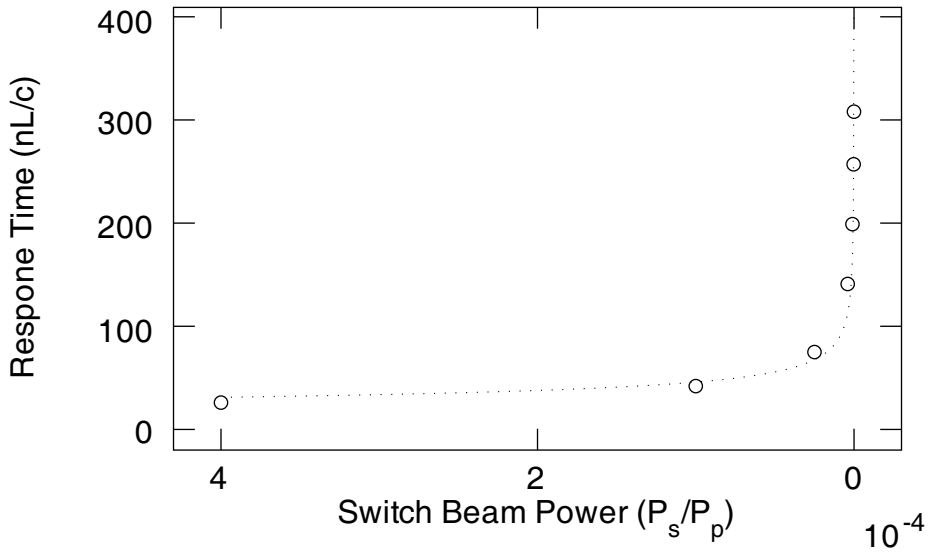

Figure 7.8: The response time of the simulated switch follows a power law $\tau_{\text{sim}}(P_s) \propto P_s^{-0.3\pm0.01}$.

For comparison, the results from numerical simulation of my pattern-based switch

also follow an inverse power law. However, the response time τ_{sim} diverges at a critical value corresponding to zero switch-beam power (see Fig. 7.8). This implies that any applied perturbation will cause the pattern to rotate, although weak perturbations cause the rotation to be extremely slow. A critical value of zero perturbation strength is consistent with the above interpretation considering that there is no fundamental symmetry-breaking introduced in the numerical simulation so the patterns have no universally-preferred orientation. My simulations begin by seeding the pattern in a specific orientation, and then causing it to rotate to a new orientation with a perturbation. This is different from biasing the pattern orientation by introducing fundamental symmetry breaking.

In the simulated switch, critical slowing down causes the pattern to rotate more slowly for weak perturbations. No orientation is preferred over another unless the switch beam is applied, thus the response time diverges at zero switch-beam power rather than at some finite critical value. The exponent found in the power law fit for τ_{sim} is -0.3 ± 0.01, which is closer to agreement with the 1D toy model if the parameter s is taken to be the field strength. Assuming this relationship, the power law exhibited by the 1D model ($\tau_{sim} \propto s^{-0.8\pm0.02}$) becomes $\tau_{sim} \propto s^{-0.4\pm0.01}$ due to the quadratic relationship between power and field strength.

The experimental data exhibits similarities to the simulation and the 1D model, although the range of switch-beam powers over which I can collect data is limited by the fact that the patterns exhibit partial switching for low switch-beam powers. The amplitude of the switch response decreases at low switch-beam powers which prevents measurement of the response time in the limit of zero switch-beam power. Thus, one weakness of the toy model is that it does not predict the transistor-like behavior that I observe in my experiment. As discussed in Chapter 6, the transistor-like response is also not observed in simulations based on a Kerr medium. For this reason, it is likely

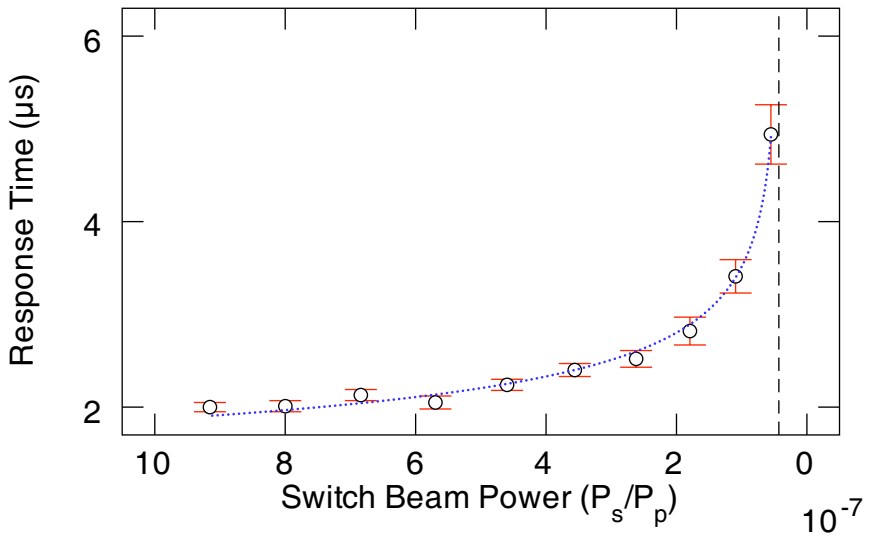

Figure 7.9: The response time measured experimentally follows a power law $\tau_{\text{exp}}(P_s) \propto (P_s - P_c)^{-0.22\pm0.01}$ where $P_c = 4.3 \pm 0.3 \times 10^{-8} P_p$. The vertical dashed line indicates P_c.

that the absorption in the experimental system is responsible for this behavior.

The available response time data, presented first in Chapter 5, spans less than an order of magnitude, so an inverse power-law fit is not entirely conclusive. However, the data is consistent with a critical switch-beam power of less than 35 pW. An approximate fit, shown in Fig. 7.9, corresponds to a critical switch-beam power of $P_c = 4.3 \pm 0.3 \times 10^{-8} P_p = 24 \pm 2$ pW. The lowest measured switch response was for $P_s = 35$ pW, which corresponds to 600 photons for $\tau_{\text{exp}} = 5\,\mu s$. If the experimental response time does diverge at $P_c = 24 \pm 2$ pW, then the lowest possible switching photon number must be between 600±40 photons and $\tau_{\text{exp}} P_c / E_p = 470 \pm 40$ photons.

7.3 Summary

Critical slowing down appears to be fundamental to my pattern-based switch. Using symmetry arguments, the toy model presented in this chapter shows the response time follows an inverse power law that diverges at a critical value of the symmetry-breaking perturbation. This suggests that the primary limitation on the switch sensitivity is likely due to additional factors such as absorption and not due to fundamental symmetry-breaking or pinned patterns. If the patterns were pinned by fundamental symmetry-breaking, I would expect to observe a power-law increase in the response time that diverges at a finite switch-beam power. Instead, my data shows that, if a critical switch-beam power exists, it is less than 35 pW and indicates the minimum number of photons capable of actuating my all-optical switch is between 470 and 600 photons.

Chapter 8

Conclusion

The ability to control patterns formed in a nonlinear optical system allows a new type of all-optical switch that is sensitive to ultra-low light levels. This dissertation describes my investigation of controlling optical patterns generated by nonlinear interactions between laser light and warm rubidium vapor. To conclude, I review the major results reported in each chapter and suggest further experiments and applications.

8.1 Summary

The first two chapters of this thesis provide introductory and background material. In Chapter 1, I frame my work in the context of nonlinear dynamics and physics in general and include a brief preview of each chapter of this thesis. In Chapter 2, I provide a more specific context for all-optical switching by describing two simple all-optical switches. The first switch, based on the nonlinear phase shift, illustrates the concepts of nonlinear self- and cross-phase shift. The second switch, based on saturated absorption, motivates the concept of the atomic cross section as a measure of the strength of interactions between light and matter. Chapter 2 also includes a review of major progress in the field of all-optical switching, including a description of several competing schemes for implementing sensitive all-optical switches.

Chapter 3 describes theoretically the origin of pattern formation in nonlinear optical systems with counterpropagating beams. I provide a conceptually simple argument for the origin of the cone-angle observed in off-axis pattern formation. I describe the

forward and backward four-wave mixing processes (FFWM and BFWM), and present three theoretical treatments that consider the roles these processes play in instabilities that spontaneously generate off-axis light. Based on the third model, which considers both FFWM and BFWM, a linear-stability analysis predicts that instability-generated light will be emitted at a finite angle θ on the order of a few mrad. Finally, I give a qualitative argument, originally presented by Grynberg, that suggests conical emission is replaced by hexagonal pattern formation when weak symmetry-breaking is present in the system [48].

Chapter 4 describes a simple experimental system that gives rise to transverse optical patterns with less than 1 mW of optical pump power. An instability in the system gives rise to mirrorless parametric self-oscillation that is responsible for generating new beams of light that propagate at an angle to the pump beams and form multi-spot patterns in the far-field. I have characterized this instability, and the generated patterns, in terms of several properties of the pump beams: frequency, intensity, size, and alignment.

This instability is also responsible for the formation of optical patterns. The form of these patterns is two or more spots arranged along a ring corresponding to the projection of a cone of light onto the plane of measurement. The opening angle for the cone is 4 mrad. Patterns with hexagonal symmetry are observed in addition to patterns with up to 18 spots. Increasing the pump beam intensity or the pump beam size leads to patterns with finer transverse scales, and in general, to patterns with a larger number of spots. Just above threshold, for all pump beam sizes studied, the pattern consists of a pair of spots symmetrically located across the pump-beam axis from one another.

Finally, I observe a secondary modulational instability that gives rise to fluctuations in the intensity of the generated light. The frequency of these fluctuations depends

directly on the angle between the counterpropagating pump beams. For well-aligned pump beams, this instability is greatly suppressed, for pump beams misaligned by $\theta_p \simeq 0.4$ mrad, the instability has a characteristic frequency of ∼245 kHz.

In Chapter 5, I present a device that operates as an all-optical switch by controlling the orientation of transverse patterns. A perturbation in the form of a weak switch beam injected into the nonlinear medium is suitable for controlling the orientation of the generated patterns and thus operating as a switch where each state of the pattern orientation corresponds to a state of the switch. Spatial filtering of the generated pattern defines the output ports of the device, and measurements of the switch response show that it can be actuated by as few as 600 photons. For a switch beam with 1/e field radius $w_0 = 185 \pm 5\,\mu$m, 600 photons correspond to an energy density of $5.4 \pm 0.7 \times 10^{-4}$ photons/$\lambda^2/(2\pi)$. My approach to all-optical switching operates at very low light levels, exhibits cascadability and transistorlike response, and is markedly simpler than cold-atom EIT systems or cavity QED systems, requiring only one optical frequency and occurring in warm atomic vapor.

Chapter 6 presents a numerical model for the switch system, and results from this model. I extend previous results of numerical simulations of pattern formation by showing that not only are hexagonal patterns generated by a scalar Kerr model, but this model also describes pattern rotation induced by an external switch beam. This model also successfully reproduces the general relationship between the switch response time and the switch-beam power that I observe experimentally. The qualitative agreement between this simple model and my experimental observations indicate that the transparent Kerr medium, although different from rubidium vapor in important ways, describes many of the features that make transverse optical patterns useful to applications in all-optical switching.

Finally, in Chapter 7, I discuss the relationship between the switch response time

and the input power in the context of nonlinear dynamics. I describe a simple toy model that exhibits critical slowing down, similar to that observed in my numerical simulations and experimental study. This model provides a conceptual foundation for understanding the minimum number of photons capable of actuating a switch based on transverse optical patterns.

8.2 Future Directions

The two main contributions of this thesis to the field of nonlinear optics are the introduction of a new paradigm for all-optical switching based on transverse patterns and an investigation into factors that limit the performance of a pattern-based switch implemented via counterpropagating-beam instabilities in warm rubidium vapor. This innovative concept of all-optical switching opens the door to many further investigations in a wide range of pattern-forming systems, and a thorough understanding of the limitations faced by the prototype atomic-vapor switch serves to guide such future research.

Counterpropagating beam systems have a relatively large parameter-space. This thesis presents a study of the optimization of a rubidium-vapor counterpropagating-beam system for use in all-optical switching. However, there are still additional parameters that could be explored in this system. As mentioned in Appendix A, transverse magnetic fields are known to induce rotation in single-mirror feedback systems [72]. For this reason, introducing weak transverse magnetic fields may provide another way to break the symmetry of the system. Unlike pump-beam misalignment, it is possible that transverse magnetic fields will break the symmetry without pinning the patterns.

Another interesting direction for this work is to explore the statistical properties of the switch in the regime where the symmetry-breaking is minimized. I observe that

the switch is unstable, or spontaneously changes state when the pump beams are well aligned. This spontaneous switching, however, may be due to extremely weak (possibly quantum) inputs, and, although reliable switching is not possible in this regime, applying additional weak inputs will likely have a measurable effect on the statistics of the switch response. In other words, single photon sensitivity may be possible by measuring the statistics of the switch response.

The two primary limitations of my switch are that is is slow (relative to optical data rates) and its input sensitivity is limited to several hundred photons. These limitations can be independently addressed by using transverse patterns generated in related systems such as semiconductor devices. Single photon switching may be possible using patterns that are generated by counterpropagating beams in a long-narrow cloud of cold-trapped atoms. Such a system has recently been developed in our group, and work will likely continue to explore this medium for pattern-formation and all-optical switching. Nonlinear response that is fast enough for GB/s data rates (which would require $\tau_r < 1$ ns) is available in nonlinear excitonic processes that occur in individual semiconductor quantum wells. Motivated by my results, hexagonal pattern formation and pattern-based all-optical switching in quantum wells are currently under investigation by Schumacher *et al.* [65, 73]. Both of these systems, cold atoms and quantum wells, are promising avenues for extending the work presented in this thesis.

On a wider scale, the idea of pattern orientation as a logic state may find applications in systems beyond optics. Hexagonal pattern formation has been observed in an enormous range of systems, and there may be many undiscovered uses for controlling the orientation of patterns generated by nonlinear systems of other sorts.

Appendix A

Preliminary experimental setup

I have previously reported results demonstrating all-optical switching with transverse optical patterns in [12] and [46]. The earlier of these, published in 2005, included data that was collected using the first version of my experimental setup for all-optical switching based on patterns. The second, published in 2008, includes a more detailed presentation of the results, and describes some improvements to the experimental system. Finally, the results presented in this thesis reflect additional improvements to the experimental system. The purpose of this Appendix is to outline the various modifications that have been made to my experimental system, and describe the resulting improvements in the operation of my all-optical switch.

A.1 Vapor cell

There are two different vapor cells that I have used. The first cell, used in the preliminary data collection, contains isotopically-enriched rubidium vapor ($> 90\%$ ^{87}Rb) in a 5-cm-long glass cell heated to 67 °C (corresponding to an atomic number density of $\sim 2 \times 10^{11}$ atoms/cm^3). The cell is made entirely of pyrex glass and the entrance and exit windows are roughly parallel; thus the entire cell must be tilted with respect to the incident laser beams to prevent possible oscillation between the uncoated windows.

The pyrex windows introduce enough aberration in the pump beam wavefronts that they provide pattern selection via symmetry-breaking. In the ideal situation, the only symmetry-breaking is provided by the pump-beam misalignment, or an other source

that can be carefully controlled. However, the pyrex windows limited the performance of the system by coupling the symmetry-breaking due to the pump-beam alignment with symmetry-breaking due to cell-window aberrations. With the pyrex cell, I found that the position of the cell windows within the path of the pump beams had a significant effect on the orientation and symmetry of the generated patterns. The pyrex cell was sufficient to demonstrate the extreme sensitivity of the generated patterns to a weak switch-beam, yet the ultimate performance of the switch was limited by the amount of symmetry breaking introduced by the vapor cell windows.

To overcome this problem, I now use a vapor cell constructed with uncoated quartz windows installed at opposite 11° angles to prevent oscillations between the entrance and exit surfaces. The cell was purchased from Triad Technology Inc., part no. TT-RB-50-V-Q. Like the pyrex cell, this quartz cell contains no buffer gas and is not paraffin coated. With this cell, I observe highly symmetric generated patterns for all pump-beam alignments with $\theta_p < 0.1$ mrad. The position of the transmitted beam on the cell windows does not substantially affect the symmetry of the generated patterns, and even tilting the vapor cell while observing the patterns does not have a significant effect on their symmetry.

Another difference between the pyrex vapor cell and the quartz cell is that the quartz cell contains rubidium vapor with naturally abundant isotopes ($\sim$ 72% ^{85}Rb, 28% ^{87}Rb). My preliminary switching experiments were conducted near the D_2 transition in ^{87}Rb, ($^5S_{1/2} \rightarrow {}^5P_{3/2}$, 780 nm wavelength), but I observe instability generated light near either the D_1 or the D_2 transition and in either isotope. The threshold for the instability is lowest for the D_2 transition where I also find that the switching is most sensitive. The pyrex cell contained isotopically-enriched ^{87}Rb because it was previously used in a different experiment and was readily available for my preliminary work. The presence of ^{85}Rb in the quartz cell does not seem to have any detrimental effects on

the generation of optical patterns or the switch response: my results from experiments using the quartz cell show a factor of five reduction in the number of photons required to actuate the switch.

A.2 Magnetic shielding

My preliminary data was collected using a vapor cell placed within a Helmholtz coil that served to cancel the component of the Earth's magnetic field along the pump-beam axis. The primary reason for this was to reduce the amount of forward-pump power rotated into the vertical polarization by the resonant Faraday effect. The instability-generated light is detected by separating it from the pump beams via polarizing beam-splitter; hence, pump-light that has its state of polarization rotated within the medium will appear as additional background and makes detection of the generated light difficult.

After the pyrex vapor cell was replaced with the quartz cell, I observed patterns that would spontaneously rotate when the pump-beams were well-aligned. Similar spontaneous pattern rotation has been observed in a single-mirror feedback system where weak transverse magnetic fields are found to induce pattern rotation [72]. The single-mirror feedback system differs from my system in that a single forward pump wave propagates through the nonlinear medium and is reflected to propagate back through the medium in the opposite direction. In one sense, this is still a counter-propagating beam system, however the feedback mirror couples the generated light back into the system after an amount of free-space diffraction that is controlled by the distance between the mirror and the nonlinear medium. Hexagonal pattern formation has also been observed in the single-mirror system and there are many qualitative similarities between the two-pump system I use, and the single-mirror feedback system.

For this reason, I used the results from single-mirror-feedback experiments to guide my attempts to stabilize the spontaneous pattern rotation. In light of the result that weak transverse magnetic fields can induce pattern rotation, I chose to shield the cell from external magnetic fields.

To eliminate transverse and longitudinal magnetic fields, I place the vapor cell within a cylinder constructed from high-permeability *mu*-metal, MμShield Inc. custom order rolled and welded sheet constructed from 0.025" thick high permeability material. The shield has an inner diameter of 5 cm and is 20.5 cm long. The *mu*-metal was annealed in a hydrogen environment after construction in order to increase the permeability and thus increase the magnetic field attenuation. I have measured field attenuation of $> 10^4$ in the central third of the shield, corresponding to the cell location. In fact, the attenuation of external fields is $> 10^2$ for all but the last 3 cm at either end of the cell.

Using this magnetic shield, the unperturbed pattern orientation is stable for several days and depends solely on the pump beam alignment and intensity.

A.3 Pump beam symmetry

As the two previous sections illustrate, the primary challenge in optimizing my experimental system for sensitive all-optical switching is the elimination of extraneous symmetry-breaking. To eliminate as much asymmetry as possible, the final experimental modification I have made to my experimental apparatus is the replacement of the single-mode optical fiber that provides spatial filtering of the pump beams. In my preliminary work, I used an optical fiber that was polished such that the entrance and exit face was 8° from normal incidence. This polish standard, known as APC, is one of two options, the other being flat-polished or PC. The benefit of using fibers with APC con-

nectors at each end is the suppression of back-reflections and Fabry-Perot fringes due to the cavity formed by the entrance and exit face of the fiber. One drawback to the APC fiber connector is that unless a custom collimation lens is used, the fiber output will not be a round gaussian mode, the intensity distribution will have a slight amount of ellipticity.

Pump beam ellipticity is a source of symmetry breaking in the system, and can provide pattern selection or lead to pinned patterns. Using the APC fiber output coupler, the pump beam vertical and horizontal waists differed by $\sim$10%. By replacing the APC single mode fiber with one that had on APC end and one PC end (ThorLabs Inc., custom fiber patch cable 780HP with one end FC/APC and one end FC/PC), I reduced the pump-beam ellipticity to $< 0.5\%$, below the precision of the measurement.[1]

A.4 Modulational instability

The modulational instability (MI) that I observe in my experimental system contributes to the sensitivity of the switch by destabilizing the pattern orientation. However, if the amplitude of the MI is large, the data fidelity, and the sensitivity begin to decrease. I find there is an optimum MI amplitude that allows high contrast between the two switch states, but also provides high sensitivity by inducing intensity fluctuations having a period that matches the characteristic pattern-rotation time.

I have found two separate ways to control the MI. Varying the total pump power affects the MI amplitude, while increasing or decreasing the pump-beam misalignment θ serves to increase or decrease the MI frequency, respectively. In my preliminary work, I was not able to continuously vary the pump-beam misalignment without significantly

[1]The beam profiles were measured using both a 10-μm pinhole mounted on a translation stage, and a calibrated CCD beam profiler. The CCD pixels are also 10μm, hence the limited precision of either measurement.

changing the generated pattern because the pyrex cell windows had a large effect on the pattern symmetry. Preliminary switching data, collected using the pyrex vapor cell, is shown in Fig. A.1(a). The data shown were collected with the pump beams 20% above threshold, hence the MI was large due to the pump beam power being further above threshold.

Comparison with Fig. A.1(b) shows the significant reduction of the MI amplitude after improvements to the experimental system and operating closer to the instability threshold. Furthermore, the frequency of the MI has been optimized to match the response time of the switch and hence leads to more sensitive switch response. Prior to minimizing the modulational instability, the lowest switching photon number I observed was 2,700. By suppressing the modulational instability, and hence lowering the detection threshold for reliable switching, I have observed reliable switching with as few as 600 photons. It should be noted that the response time of the data shown in Fig. A.1(a) and (b) should not be compared directly to one another because the input switch beam power was not the same across these two measurements. For the data shown in Fig. A.1(a) the input power was 3 nW and for the data shown in Fig. A.1(b) the input power was 900 pW.

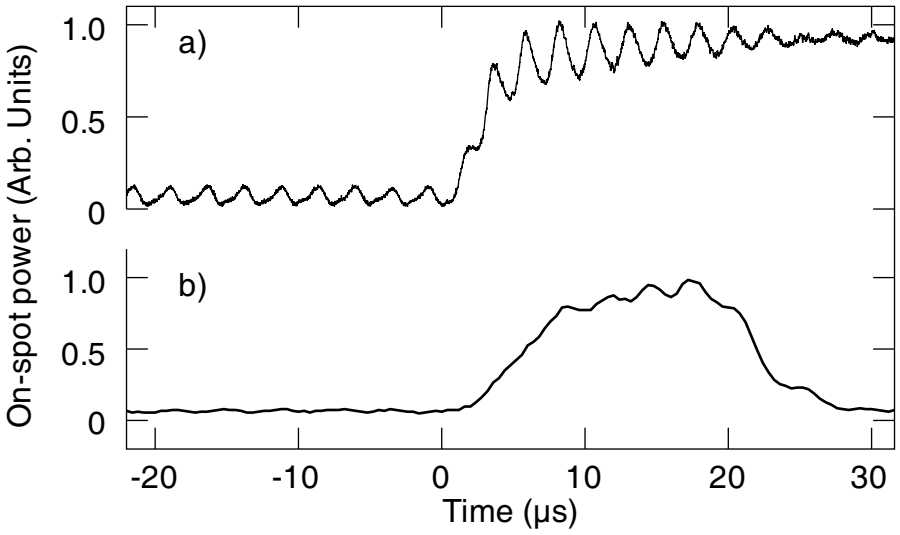

Figure A.1: Comparison of modulational instability for preliminary data and recent data. a) Preliminary data shows large modulation amplitude. b) In recent data, the MI amplitude is suppressed by operating close to threshold.

Bibliography

[1] M. C. Cross and P. C. Hohenberg, Pattern formation outside of equilibrium, *Rev. Mod. Phys.* **65**, 851 (1993).

[2] S. H. Strogatz, *Nonlinear Dynamics and Chaos: With Applications to Physics, Biology, Chemistry and Engineering* (Perseus Books Group) (2001).

[3] M. Lim, R. Metzler, and Y. Bar-Yam, Global Pattern Formation and Ethnic/Cultural Violence, *Science* **317**, 1540 (2007).

[4] R. K. Cavin and V. V. Zhirnov, Generic device abstractions for information processing technologies, *Solid-State Electronics* **50**, 520 (2006).

[5] L. A. Lugiato, Transvserse nonlinear optics: Introduction and review, *Chaos, Solitons, & Fractals* **4**, 1251 (1994).

[6] R. W. Keyes, Power dissipation in information processing, *Science* **168**, 796 (1970).

[7] J. Sharping, M. Fiorentino, P. Kumar, and R. Windeler, All-optical switching based on cross-phase modulation in microstructure fiber, *Photonics Technology Letters, IEEE* **14**, 77 (Jan 2002).

[8] M. Soljačić, S. G. Johnson, S. Fan, M. Ibanescu, E. Ippen, *et al.*, Photonic-crystal slow-light enhancement of nonlinear phase sensitivity, *J. Opt. Soc. Am. B* **19**, 2052 (2002).

[9] J. Zhang, G. Hernandez, and Y. Zhu, All-optical switching at ultralow light levels, *Opt. Lett.* **32**, 1317 (2007).

[10] W. J. Firth and C. Paré, Transverse modulational instabilities for counterpropagating beams in kerr media,, *Opt. Lett.* **13**, 1096 (1988).

[11] R. Chang, W. J. Firth, R. Indik, J. V. Moloney, and E. M. Wright, Three-dimensional simulations of degenerate counterpropagating beam instabilities in a nonlinear medium, *Opt. Commun.* **88**, 167 (1992).

[12] A. M. C. Dawes, L. Illing, S. M. Clark, and D. J. Gauthier, All-Optical Switching in Rubidium Vapor, *Science* **308**, 672 (2005).

[13] R. W. Boyd, *Nonlinear Optics, Second Edition* (Academic Press) (2002).

[14] A. E. Siegman, *Lasers* (University Science Books) (1986).

[15] R. W. Keyes, Information, computing technology, and quantum computing, *J. Phys.: Condens. Matter* **18**, S703 (2006).

[16] S. E. Harris and Y. Yamamoto, Photon switching by quantum interference, *Phys. Rev. Lett.* **81**, 3611 (1998).

[17] C. J. Hood, M. S. Chapman, T. W. Lynn, and H. J. Kimble, Real-time cavity qed with single atoms, *Phys. Rev. Lett.* **80**, 4157 (1998).

[18] K. Birnbaum, A. Boca, R. Miller, A. Boozer, T. Northup, *et al.*, Photon blockade in an optical cavity with one trapped atom, *Nature* **436**, 87 (2005).

[19] X. Hachair, L. Furfaro, J. Javaloyes, M. Giudici, S. Balle, *et al.*, Cavity-solitons switching in semiconductor microcavities, *Phys. Rev. A* **72**, 013815 (2005).

[20] S. E. Harris, Electromagnetically induced transparency, *Phys. Today* **50**, 36 (1997).

[21] H. Schmidt and A. Imamoglu, Giant kerr nonlinearities obtained by electromagnetically induced transparency, *Opt. Lett.* **21**, 1936 (1996).

[22] A. S. Zibrov, M. D. Lukin, and M. O. Scully, Nondegenerate parametric self-oscillation via multiwave mixing in coherent atomic media, *Phys. Rev. Lett.* **83**, 4049 (1999).

[23] D. A. Braje, V. Balić, G. Y. Yin, and S. E. Harris, Low-light-level nonlinear optics with slow light, *Phys. Rev. A* **68**, 041801 (2003).

[24] Y.-F. Chen, Z.-H. Tsai, Y.-C. Liu, and I. A. Yu, Low-light-level photon switching by quantum interference, *Opt. Lett.* **30**, 3207 (2005).

[25] S. E. Harris and L. V. Hau, Nonlinear optics at low light levels, *Phys. Rev. Lett.* **82**, 4611 (1999).

[26] M. Yan, E. G. Rickey, and Y. Zhu, Observation of absorptive photon switching by quantum interference, *Phys. Rev. A* **64**, 041801 (2001).

[27] K. J. Resch, J. S. Lundeen, and A. M. Steinberg, Conditional-phase switch at the single-photon level, *Phys. Rev. Lett.* **89**, 037904 (2002).

[28] H. Kang, G. Hernandez, and Y. Zhu, Slow-light six-wave mixing at low light intensities, *Phys. Rev. Lett.* **93**, 073601 (2004).

[29] H. Wang, D. Goorskey, and M. Xiao, Controlling the cavity field with enhanced Kerr nonlinearity in three-level atoms, *Phys. Rev. A* **65**, 051802 (2002).

[30] T. Tanabe, M. Notomi, S. Mitsugi, A. Shinya, and E. Kuramochi, Fast bistable all-optical switch and memory on a silicon photonic crystal on-chip, *Opt. Lett.* **30**, 2575 (2005).

[31] M. Soljačić, E. Lidorikis, J. D. Joannopoulos, and L. V. Hau, Ultralow-power all-optical switching, *Appl. Phys. Lett.* **86**, 171101 (2005).

[32] M. Islam, S. Dijaili, and J. Gordon, Modulation-instability-based fiber interferometer switch near 1.5 Mu m, *Opt. Lett.* **13**, 518 (1988).

[33] D. Chang, A. Sørensen, E. Demler, and M. Lukin, A single-photon transistor using nano-scale surface plasmons (2007), arXiv:0706.4335v1 [quant-ph].

[34] Y. Silberberg and I. Bar-Joseph, Optical instabilities in a nonlinear kerr medium, *J. Opt. Soc. Am. B* **1**, 662 (1984).

[35] G. Khitrova, J. F. Valley, and H. M. Gibbs, Gain-feedback approach to optical instabilities in sodium vapor, *Phys. Rev. Lett.* **60**, 1126 (1988).

[36] A. L. Gaeta, R. W. Boyd, J. R. Ackerhalt, and P. W. Milonni, Instabilities and chaos in the polarizations of counterpropagating light fields, *Phys. Rev. Lett.* **58**, 2432 (1987).

[37] D. J. Gauthier, M. S. Malcuit, and R. W. Boyd, Polarization instabilities of counterpropagating laser beams in sodium vapor, *Phys. Rev. Lett.* **61**, 1827 (1988).

[38] D. J. Gauthier, M. S. Malcuit, A. L. Gaeta, and R. W. Boyd, Polarization bistability of counterpropagating laser beams, *Phys. Rev. Lett.* **64**, 1721 (1990).

[39] A. Petrossian, M. Pinard, A. Maître, J. Y. Courtois, and G. Grynberg, Transverse-pattern formation for counterpropagating laser beams in rubidium vapour, *Europhys. Lett.* **18**, 689 (1992).

[40] G. Grynberg, E. Le Bihan, P. Verklerk, P. Simoneau, J. R. R. Leite, *et al.*, Observation of instabilities due to mirrorless four-wave mixing oscillations in sodium, *Opt. Commun.* **67**, 363 (1988).

[41] R. Bennink, V. Wong, A. Marino, D. Aronstein, R. Boyd, *et al.*, Honeycomb pattern formation by laser-beam filamentation in atomic sodium vapor, *Phys. Rev. Lett.* **88**, 113901 (2002).

[42] A. L. Gaeta and R. W. Boyd, Transverse instabilities in the polarizations and intensities of counterpropagating light waves, *Phys. Rev. A* **48**, 1610 (1993).

[43] A. E. Kaplan and C. T. Law, *IEEE J. Quantum Electron.* **21**, 1529 (1985).

[44] A. Yariv and D. M. Pepper, Amplified reflection, phase conjugation, and oscillation in degenerate four-wave mixing, *Opt. Lett.* **1**, 16 (1977).

[45] A. Maître, A. Petrossian, A. Blouin, M. Pinard, and G. Grynberg, Spatio-temporal instability for counterpropagating beams in rubidium vapor, *Opt. Commun.* **116**, 153 (1995).

[46] A. M. C. Dawes, L. Illing, J. A. Greenberg, and D. J. Gauther, All-optical switching with transverse optical patterns, *Phys. Rev. A* **77**, 013833 (2008).

[47] R. Y. Chiao, P. L. Kelley, and E. Garmire, Stimulated four-photon interaction and its influence on stimulated rayleigh-wing scattering, *Phys. Rev. Lett.* **17**, 1158 (1966).

[48] G. Grynberg, Mirrorless four-wave mixing oscillation in atomic vapors, *Opt. Commun.* **66**, 321 (1988).

[49] G. Grynberg and J. Paye, Spatial instability for a standing wave in a nonlinear medium, *Europhys. Lett.* **8**, 29 (1989).

[50] Y. Silberberg and I. B. Joseph, Instabilities, self-oscillation, and chaos in a simple nonlinear optical interaction, *Phys. Rev. Lett.* **48**, 1541 (1982).

[51] W. J. Firth, A. Fitzgerald, and C. Paré, Transverse instabilities due to counterpropagation in kerr media, *J. Opt. Soc. Am. B* **7**, 1087 (1990).

[52] J. Pender and L. Hesselink, Degenerate conical emissions in atomic sodium vapor, *J. Opt. Soc. Am. B* **7**, 1361 (1990).

[53] N. Tan-no, T. Hoshimiya, and H. Inaba, Dispersion-free amplification and oscillation in phase-conjugate four-wave mixing in an atomic vapor doublet, *IEEE J. Quantum Electron.* **16**, 147 (1980).

[54] G. D'Alessandro and W. Firth, Spontaneous hexagon formation in a nonlinear optical medium with feedback mirror, *Phys. Rev. Lett.* **66**, 2597 (1991).

[55] T. Honda, Flow and controlled rotation of the spontaneous optical hexagon in KNbO3, *Opt. Lett.* **20**, 851 (1995).

[56] G. Grynberg, A. Maître, and A. Petrossian, Flowerlike patterns generated by a laser beam transmitted through a rubidium cell with single feedback mirror, *Phys. Rev. Lett.* **72**, 2379 (1994).

[57] A. Aumann, T. Ackemann, and W. Lange, Selection between hexagonal, square and stripe patterns in a polarization instability: an experimental investigation,

Ann. Phys. (Leipzig) **13**, 379 (2004).

[58] T. Ackemann, A. Aumann, E. G. Westhoff, Y. A. Logvin, and W. Lange, Polarization degrees of freedom in optical pattern forming systems: alkali metal vapour in a single-mirror arrangement, *Journal of Optics B: Quantum and Semiclassical Optics* **3**, S124 (2001).

[59] S. Saikan, Polarization and angular-momentum dependeces of degenerate backward four-wave mixing in atomic lines, *J. Opt. Soc. Am.* **72**, 514 (1982).

[60] M. Pinard, R. W. Boyd, and G. Grynberg, Third-order nonlinear optical response resulting from optical pumping: Effects of atomic motion, *Phys. Rev. A* **49**, 1326 (1994).

[61] A. N. Nesmeyanov, *Vapor Pressure of the Chemical Elements* (Amsterdam: Elsevier) (1963).

[62] M. Gruneisen, A. Gaeta, and R. Boyd, Exact theory of pump-wave propagation and its effect on degenerate four-wave mixing in saturable-absorbing media, *Journal of the Optical Society of America B: Optical Physics* **2**, 1117 (1985).

[63] P. Kish, The effect of network cabling on bit error rate performance, Tech. rep., NORDX/CDT (2000).

[64] J. A. Greenberg, M. Oria, A. M. C. Dawes, and D. J. Gauthier, Absorption-induced trapping in an anisotropic magneto-optical trap, *Opt. Express* **15**, 17699 (2007).

[65] S. Schumacher, N. H. Kwong, R. Binder, and A. L. Smirl, All-optical switching in planar semiconductor microcavities (2007), arXiv:0712.2060v1 [cond-mat.other].

[66] J. Fleck, J. Morris, and M. Feit, Time-dependent propagation of high energy laser beams through the atmosphere, *Appl. Phys. A* **10**, 129 (1976).

[67] J. Moloney, M. Belic, and H. Gibbs, Calculation of transverse effects in optical bistability using fast fourier transform techniques, *Opt. Commun.* **41**, 379 (1982).

[68] J. M. Burzler, S. Hughes, and B. S. Wherrett, Split-step fourier methods applied to model nonlinear refractive effects in optically thick media, *Appl. Phys. B* **62**, 389 (1996).

[69] C. Penman, W. J. Firth, and C. Paré, Transverse modulational instability of counter-propagating beams in a kerr medium divided into thin slices, *J. Mod. Opt.* **37**, 719 (1990).

[70] G. Agrawal, *Nonlinear Fiber Optics (Optics and Photonics)* (Academic Press) (2001).

[71] J. M. Jarem and P. P. Banerjee, *Computational Methods for Electromagnetic and Optical Systems (Optical Engineering)* (Marcel Dekker, Inc., New York) (2000).

[72] F. Huneus, B. Schäpers, T. Ackemann, and W. Lange, Optical target and spiral patterns in a single-mirror feedback scheme, *Appl. Phys. B* **76**, 191 (2003).

[73] S. Schumacher, N. H. Kwong, and R. Binder, Large optical gain from four-wave mixing instabilities in semiconductor quantum wells, *Euro. Phys. Lett.* **81**, 27003 (2008).

Biography

Andrew M. Dawes was born in Pullman, Washington on December 11, 1979. He grew up in Moscow, Idaho, a small university town in the rolling hills of the Palouse. In 1998 he graduated from Moscow High School and matriculated at Whitman College in Walla Walla, Washington. He received the B.A. degree with honors in physics in 2002. He began graduate study at Duke University in the fall of 2002 at which point he joined the Quantum Electronics Lab under the supervision of Dr. Daniel J. Gauthier. In 2003 he married Leslie Lauren Crandell and has gone by Andrew M. Crandell Dawes since. He received his A.M. in 2005 and his Ph.D. in 2008 for his study of all-optical switching in atomic vapor.

Andrew was named Teaching Assistant of the year in 2004. Also while at Duke, he received the Walter Gordy Departmental Fellowship from the Duke University Department of Physics, and the John T. Chambers Fellowship from the Fitzpatrick Institute for Photonics. In 2006 he was a finalist for the OSA New Focus/Bookham Student Award.

Publications

A. M. C. Dawes, L. Illing, J. A. Greenberg, and D. J. Gauthier, All-optical switching with transverse optical patterns, Phys. Rev. A 77, 013833 (2008).

A. M. C. Dawes and D. J. Gauthier, Using Transverse Patterns for All-Optical Switching in Coherence and Quantum Optics IX, N. P. Bigelow, J. H. Eberly, C. R. Stroud Jr., Eds., p. 442, (Optical Society of America, Washington, DC, 2007).

J. A. Greenberg, M. Oria, A. M. C. Dawes, and D. J. Gauthier, Absorption induced trapping in an anisotropic magneto-optical trap, Opt. Express 15, 17699 (2007).

Z. Zhu, A. M. C. Dawes, D. J. Gauthier, L. Zhang, and A. E. Willner, Broadband SBS slow light in an optical fiber, J. Lightwave Tech. 25, 201 (2007).

H. Jeong, A. M. C. Dawes, and D. J. Gauthier, Direct observation of optical precursors in a region of anomalous dispersion, Phys. Rev. Lett. 96, 143901 (2006).

M. D. Stenner and M. A. Neifeld, Z. Zhu, A. M. C. Dawes, and D. J. Gauthier, Distortion management in slow-light pulse delay, Opt. Express 13, 9995 (2005).

A. M. C. Dawes, L. Illing, S. M. Clark, D. J. Gauthier, All-Optical Switch Controls Strong Beams with Weak Ones, in Optics and Photonics News 16, no. 12, pp. 34 (2005).

A. M. C. Dawes, S. M. Clark, L. Illing, D. J. Gauthier, Observation of ultra-low-light-level all-optical switching, in Advanced Optical and Quantum Memories and Computing II; H. J. Coufal, Z. U. Hasan, and A. E. Craig; Eds., Proc. SPIE 5735, 60-68 (2005).

A. M. C. Dawes, L. Illing, S. M. Clark, and D. J. Gauthier, All-optical switching in rubidium vapor, Science 308, 672 (2005).

A. M. Dawes and M. Beck, Simultaneous quantum state measurements using array detection in Coherence and Quantum Optics VIII; N. P. Bigelow, J. H. Eberly, C. R. Stroud, and I. A. Walmsley; Eds., (Kluwer Academic/Plenum, New York, 2003) p. 301.

A. M. Dawes, M. Beck, and K. Banaszek, Mode optimization for quantum-state tomography with array detectors Phys. Rev. A 67, 032102 (2003).

A. M. Dawes and M. Beck, Simultaneous quantum state measurements using array detection Phys. Rev. A 63, 040101(R) (2001).

Presentations

“Recent progress in low-light switching via optical patterns,” Conference on coherent control of the fundamental processes in optics and X-rayoptics, Nizhny Novgorod - Kazan, Russia, June 29 - July 3, 2006 (invited).

“Improving the Bandwidth of SBS-Based Slow-Light Delay,” Conference on Lasers and Electro-Optics (CLEO), Long Beach, CA, May 21-26, 2006.

“Observation of ultra-low-light-level all optical switching,” Photonics West, San Jose, CA, January 22-27, 2005 (invited).

“Mode optimization for quantum-state tomography with array detectors,” The Eighth Rochester Conference on Coherence and Quantum Optics, Rochester, NY, June 13-16, 2001.

“Simultaneous quantum state measurement using array detection,” Northwest Section APS Meeting, Seattle, WA, May 25-26, 2001.

Poster Presentations

"Using transverse patterns for all-optical switching," The Ninth Rochester Conference on Coherence and Quantum Optics, Rochester, NY, June 10-13, 2007.

"All-optical switching: the weak controlling the strong," Fitzpatrick Institute for Photonics 6th Annual Meeting, Durham, NC, September 28-29, 2006.

"All-optical switching: the weak controlling the strong," Dynamics Days 2006, Bethesda, MD, January 4-7, 2006.

"Information Velocity," Fitzpatrick Institute for Photonics 4th Annual Meeting, Durham, NC, May 11-12, 2004.

"Simultaneous quantum state measurement using array detection," 9th Regional Conference on Undergraduate Research, Murdock College Science Research Program, University of Puget Sound, Tacoma, WA (2000).